INFORMATION TO USERS

The most advanced technology has been used to photograph and reproduce this manuscript from the microfilm master. UMI films the text directly from the original or copy submitted. Thus, some thesis and dissertation copies are in typewriter face, while others may be from any type of computer printer.

The quality of this reproduction is dependent upon the quality of the copy submitted. Broken or indistinct print, colored or poor quality illustrations and photographs, print bleedthrough, substandard margins, and improper alignment can adversely affect reproduction.

In the unlikely event that the author did not send UMI a complete manuscript and there are missing pages, these will be noted. Also, if unauthorized copyright material had to be removed, a note will indicate the deletion.

Oversize materials (e.g., maps, drawings, charts) are reproduced by sectioning the original, beginning at the upper left-hand corner and continuing from left to right in equal sections with small overlaps. Each original is also photographed in one exposure and is included in reduced form at the back of the book. These are also available as one exposure on a standard 35mm slide or as a 17" x 23" black and white photographic print for an additional charge.

Photographs included in the original manuscript have been reproduced xerographically in this copy. Higher quality 6" x 9" black and white photographic prints are available for any photographs or illustrations appearing in this copy for an additional charge. Contact UMI directly to order.

U·M·I

University Microfilms International
A Bell & Howell Information Company
300 North Zeeb Road, Ann Arbor, MI 48106-1346 USA
313/761-4700 800/521-0600

Order Number 9000029

K-Shell ionization cross sections of the elements Pr, Nd, Sm, Tm, Ta, and W for 1-3 MeV protons

Guardala, Noel Adam, Ph.D.

City University of New York, 1989

U·M·I
300 N. Zeeb Rd.
Ann Arbor, MI 48106

K-Shell Ionization Cross Sections of the Elements Pr, Nd, Sm, Tm, Ta, and W for 1-3 MeV Protons

by

Noel A. Guardala

A dissertation submitted to the Graduate Faculty in Chemistry in partial fulfillment of the requirements for the degree of Doctor of Philosophy, The City University of New York

1989

This manuscript has been read and accepted for the Graduate Faculty in Chemistry in satisfaction of the dissertation requirement for the degree of Doctor of Philosophy.

11/28/88
Date

Evan T. Williams
Chair of Examining Committee

11/28/88
Date

A.M. Lesser
Executive Officer

Harmon L. Finston

Max Diem
Supervisory Committee

The City University Of New York

Abstract

K-Shell Ionization Cross Sections of the Elements Pr, Nd, Sm, Tm, Ta and W for 1.0 - 3.0 MeV Protons

by Noel Guardala

Advisor: Professor Evan T. Williams

We have attempted to measure with an improved degree of accuracy the values of the K-Shell ionization cross section, σ_{KI}, for selected elements in the region, $59 \leq Z \leq 74$, using 1.0 - 3.0 MeV H^+ as the projectiles. This is a region of the Periodic Table where due to the strong permanent deformations, β_o, of the nuclear ground state, the values of the nuclear Coulomb excitation cross sections, σ_{CE}, become comparable in magnitude to the values of σ_{KI} for the direct atomic collision process.

Not only are the two inelastic channels comparable in overall magnitude, but because the same nuclear states that are easily populated by CE tend to decay primarily by K-Shell internal conversion. This nuclear de-excitation process results in the emission of K x-rays which are identical to the K x-rays produced by direct atomic ionization, DAI. This means that the yields of K x-rays produced in these types of collisions must be corrected for by either calculating the values of σ_{CE} or by measuring the yields of CE γ-rays. The the portion of K x-rays arising from the CE channel can then be subtracted from the total yield of K x-rays.

We have tried the strategy of using where possible isotopes which have smaller values of β_o, and therefore smaller values of σ_{CE}, as a means of practically eliminating the CE contribution to the yield of K x-rays. Where no spherical isotopes exist, we have attempted to both calculate and to

measure the yield of CE γ-rays to a high level of accuracy and then use the appropriate internal conversion coefficients, ICC. This was done to arrive at the "true" amount of K x-rays coming from CE.

The other experimental goal of the thesis was the development of a new normalization method using the characteristic L_{γ_1} and $L_{\gamma_{2,3}}$ x-rays of the elements studied. This method was compared to the already established normalization methods which uses either Rutherford back-scattering, RBS, or CE γ-rays (when the values of σ_{CE} are large enough). Significant attention was paid to the determination of the absolute energy efficiency calibration of an intrinsic Ge photon detector. The photon energy range covered in the calibration was 4.0 - 160 keV. This range of energy includes all the L x-rays of the elements studied up to the higher energies typical of the γ-rays produced by CE of the most deformed nuclides.

Dedication

For Phyllis, who sacrificed far more than she had to
while seeing me through the darkest hours.
Someday soon we will enjoy it all together.

and

To my mother Catherine, and my two brothers, Frank and Pat,
for providing a home to grow up in
full of love,support and encouragement.

Acknowledgments

I am extremely grateful to a number of very talented and gifted former colleagues at the Dynamitron Lab of Brooklyn College. Their contributions to this thesis were in many cases superior to my own. I merely exercised the good sense to seek out their expertise and advice. They were always kind enough to offer it to me.

This is not a statement of false modesty, but an attempt to draw some well deserved attention to their seemingly unique talents. My sincere hope is that in some way I made (or may make in the future) as profound an impact on their lives and careers as they did on mine. It will always be pleasant for me to remember that their efforts on my behalf were primarily motivated by friendship.

Steven Greenberg, who did so much of the computer work and some other "dirty" work for me that I would have never done on my own. He went far beyond the call of duty (and long into the early morning hours) for me many times. Dong Yan, who was always eager and patient to help me no matter how overburdened he might be. Dr. J.P. Farrell, whose knowledge and abilities in the area of accelerator physics are astonishing to me. Ted Liubicich, for making so many practical and necessary suggestions which saved many hours of work. Prof.George Skorinko, for giving me a great deal of valuable advice concerning target making and the construction of the scattering chamber. Bill Steuber for doing many "simple" things (for him) around the lab that I would have found quite difficult to do.

The contributions of the Machine Shop of Brooklyn College to many theses are legendary. The work associated with this thesis has both, major contribitutions from the Machine Shop and some new "legends". So another statement concerning their abilities is very much in order. Marty Berman and Sol Coltun not only did their usual magnificent jobs in building equipment for me, they also imparted some of their extremely valuable wisdom to me. As a result, I am now and probably will always be very impressed by the "art" of their craft.

To the members of my thesis committee, especially my mentor, Evan T. Williams, Prof.H.L.Finston of Brooklyn College and Prof. Max Diem of Hunter College, C.U.N.Y.; I am very appreciative of their patience, flexibility, and cooperation in dealing with an "unorthodox" student who usually placed himself in highly unusual situations.

I am very much indebted to my new colleagues at Stanford University; Dr.David Spooner and Prof.Eduardo Montenegro of the Catholic University in Rio de Janerio, Brazil. Dave took over for Steve Greenberg by tutoring me in the strange and wonderful world of the micro-computer. His help was obtained many times at the expense of his own thesis editing. Eduardo not only provided to me his theoretical cross section calculations, spent a good deal of time with me in our office discussing the mysteries of ion-atom collisions and detector calibrations, but most importantly made me feel very welcome as a new member of the high-energy atomic physics "fraternity".

A large amount of very useful information (as well as the computer calculations) concerning nuclear Coulomb excitation coupled-channels effects were provided to me by both I.Y. Lee of Oak Ridge and B. Kostilinski of the Univ. of Rochester's Nuclear Structure Lab. Their help and advice is deeply appreciated. G. Lapicki of East Carolina Univ. was very kind in providing me with his ECPSSR cross section calculations for the elements studied in this thesis. R.H. Pehl of Lawrence Berkeley Radiation Lab

was very gracious and generous with his time in discussing detector design strategies with me, a subject for which he holds a virtual monopoly on. He literally provided a "window" into the world of solid-state detectors for me.

Last but not least the help of that lifelong resident of sunny California and long-time role model for me, Myron Elgart of Rana Associates, Santa Clara, CA. is greatly appreciated. Will the circle remain unbroken? The presence of Penn and Teller during the final throes of this thesis added the proper touches of magic, fantasy and illusion, key issues always central in this work from its inception.

Table of Contents

Chapter I. Introduction

Chapter II. Theory

Chapter III. Experimental Procedure

Chapter IV. Absolute Energy Efficiency Calibration of a HyperPure Ge x-ray/ - ray Detector

List of Figures

List of Tables

Page

Chapter I. Introduction:

Inner-shell collision studies with light, energetic projectiles such as protons, deuterons, alpha particles etc., have attracted considerable attention from both experimentalists [1-3] and theorists [4-6]. The results of these investigations are significant for both applied and fundamental research, with regard to ion-beam analysis, fusion development, stopping-power calculations, and in general to obtain data necessary for nuclear physics experiments at both low and high energy [7-11].

The range of target atoms investigated comprises nearly the entire Periodic Table except for the very lightest elements (which can be thought of as being devoid of inner electrons) and the heaviest short-lived elements [12-13]. The projectiles used range from H+ ions all the way up to fully stripped Cm ions [14]. The bombarding energies used in these types of collision studies range from the keV region to the relativistic velocities of GeV/u [15,16].

In this thesis we will restrict ourselves to discussions of ions light enough to be accelerated by the Brooklyn College 3.75 MeV Dynamitron. The ions have low Z, so that the ratio of projectile charge, Z_1, to the target atom charge, Z_2, is such that $Z_1 << Z_2$ or $Z_1/Z_2 << 1$. This condition represents the asymmetric region of ion-atom collisions and is distinguished from the so called symmetric region where $Z_1 = Z_2$. The asymmetric region also turns out to be a regime where a first-order perturbation approach is quite adequate to describe the ionization process [17,18].

The mechanisms for excitation and ionization are simpler in the asymmetric region being limited to direct Coulomb ionization. The simple, light

ion is treated as a bare projectile; no consideration is given to its electronic structure regardless of charge state. The perturbation of the inner-shell electron is due entirely to a time-varying electric field associated with the nuclear charge and velocity of the ion. The collision transfers sufficient momentum to the bound electron so that its kinetic energy is large enough to propel it into the continuum. The energy transfer must be larger than the binding energy for the stationary state under consideration if ionization is to take place. Promotion to a higher bound state is negligible for all elements heavy enough to have inner shells.

Another mechanism which is possible in the asymmetric region is electron capture by the projectile. This mechanism, though always present is a very small channel for inner-shell ionization for collision systems with $Z_1/Z_2 < 0.3$. A typical value of the capture channel in the collision regimes studied in this thesis is 1×10^{-5} of the values for the direct Coulomb ionization channel [19]. Other more exotic channels for ionization are vacancy transfer and vacancy sharing [20,21] but they need not be considered as affecting the results of this thesis.

The symmetric region of collision studies involves a variety of complex excitation mechanisms [22,23]. When $Z_1 = Z_2$, the possibility of coupling between the various atomic orbitals, (AO's, so-called basis states), on both projectile and target becomes a realistic concern. Especially in slow, adiabatic collisions, the interactions take place and evolve on a time scale similar to the collision time. The time-dependent nature of the states that are formed opens up many new excitation channels. These new channels make possible a wide range of electronic transitions due to the energies, angular momenta and parities of the inner-shell states involved (assuming of

course the core and valence states are separated sufficiently). The energies of the time-evolved states and the transition probabilities are also time-dependent i.e. collision-velocity dependent. We are now of course considering the inner-shell states of both projectile and target.

The fingerprints for such interactions are seen in the x-ray spectra observed during bombardment [24,25]. Instead of the characteristic x-rays of the target atom (or if the projectile has an electronic structure complex enough to give x-rays itself) only being present, a range of continuous x-ray energies are observed, appearing as a continuum upon which there is observed the superimposed characteristic atomic x-rays. The couplings between the AO's of projectile and target, forming molecular orbitals, (MO's), usually follow similar patterns for the MO's (diabatic states) that would be formed in a stable diatomic molecule (the stability of the molecule may be quite small depending on the type of atoms involved). In this way the adiabatic collision may be thought of as the formation of a quasi-molecule. Transitions between the various MO's are not only due to the effects of a moving charge (as in Coulomb ionization) but have the additional mechanisms of rotational coupling along the inter-nuclear axis of the quasi-molecule and the effect of Pauli promotion due to the fermionic nature of electrons.

For $Z > 12$, K-shell ionization cross sections, σ_{KI}, are most conveniently measured by the yield of K x-rays emitted during bombardment. Whereas for $Z_1 > 47$, L subshell cross sections, σ_{Li}, can be determined from the yields of the characteristic L x-rays. The determination of the K shell ionization cross section via the yield of K x-rays requires amongst other things an accurate knowledge of the fluorescent yield, ω_K, of the K shell

for the element being studied. A possible factor influencing the values of ω_K is multiple vacancy production in the target atom.

Ionization is most likely to occur in two regimes: a) if the projectile's velocity is significantly larger than the orbital atomic electron's velocities on the target atom, i.e. a relatively energetic projectile and typically a light target, b) if velocity matching occurs between vacant orbitals on the projectile and full or partially full target orbitals, i.e. a projectile whose electronic structure can be considered "rich" no matter what its pre-collision charge state is. These factors do not contribute to the results presented in this thesis. Therefore the values of ω_K will be taken from the standard literature tabulations in order to arrive at the σ_{KI} values [26].

This general procedure is much more difficult for L subshell measurements due to two processes which transfer vacancies from one L subshell to another. One of these occurs regardless of how the L-subshell vacancy was prepared, while the other is very dependent upon the collision parameters. The first process is the Coster-Kronig transitions which are closely related to non-radiative transitions of the Auger type in that they transfer vacancies in a non-radiative process from states of lower angular momentum to states of higher angular momentum but of the same principal quantum number. For L subshell vacancies there is a strong transition probability for L_1 vacancies (l=0,j=1/2) to be transferred to both the L_2 subshell (l=1,j=1/2) and to the L_3 subshell (l=1,j=3/2) while L_2 vacancies can be transferred to the L_3 subshell with the energy liberated in the process going to ionize an electron in a higher subshell (M,N....) [27,28]. The process is intra-shell coupling during the collision which moves L subshell

vacancies to higher states of angular momentum inside the L shell. Instead of being purely an atomic property of the the target, the degree of coupling depends strongly on the collision parameters [29,30].

L subshell cross-section measurements are further complicated by the intrinsic closeness and overlapping of the characteristic L x-ray lines, a greater amount of attenuation due to their relatively low energy, uncertainties in the ω's, radiative transition widths Γ_i, and the relative transition rates for the various Coster-Kronig processes [31-33].

Electrons of two distinct types are emitted during ion-atom collisions. In addition, of course, to the various x-ray photons, there is the flux of ejected electrons, the so-called "delta-electrons", whose study is of considerable interest [34,35], and secondly the aforementioned Auger process which removes additional inner-shell electrons during the non-radiative relaxation process following the production of an inner-shell vacancy. In contrast to the delta electrons which are ejected into the continuum with a wide range of energies, the Auger electrons typically have very definite energies which correspond to the difference in energy between the initial and final electronic configurations of the ion [36].

Due to the inherent difficulty of measuring both fluence and energies of "low energy" electrons emitted from solid targets, most K and L shell ionization cross-sections are determined by measuring the x-ray yield. X-ray transitions larger than 1 keV can be reliably measured by using solid-state photon detectors, usually either a Lithium-drifted Silicon detector, Si(Li), or a hyperpure Germanium, HPGe. Both detectors are operated at liquid Nitrogen temperatures, 77 K. X-ray transitions of energies down to 277 ev (C K x-rays) can be detected using a windowless Si(Li) detector (no

Be window in front of the active volume of the crystal) or with a windowless proportional counter (the traditional way before the windowless Si(Li) was available) [37-39]. For very-high-resolution studies but not for cross-section determinations, solid state detectors are replaced by Bragg diffractometers which are better suited to study multiplets that can not be resolved by the energy dispersive detectors [40].

In the case of elements which can be easily vaporized, or are gases, or exist in compounds which are quite volatile, the vacancy production cross-sections can be studied very accurately by Auger spectroscopy. One of the interesting aspects of Auger spectra is that the discrete levels of the target atom are "perturbed" by their electronic environment, that is, by the type of atoms present in the molecule. This leads to the study of "chemical" shifts in the Auger spectra of a particular element as a function of the type of atoms it is bound to [41,42]. Another novel approach is the study of projectile Auger emission which is not only a sensitive indicator of the collision process but can also be used to study meta-stable ionic configurations formed by selective state electron capture [43].

Auger studies in collision physics are usually limited to gas targets or to projectiles because they are both sufficiently transparent to the low-energy electrons. It is also worth mentioning here that for the low Z elements $Z_2 < 11$, the values of ω_K are very small; typically the radiative transition rates are 1×10^{-4} times smaller than the non-radiative transition rates.

The K x-rays of the elements studied in this thesis are sufficiently energetic to be detected by solid-state detectors and the radiative decay rates for the K-shell vacancy are much larger than the the non-radiative

rates. The values of ω_K for these elements are 0.9 or larger. The L x-rays of these elements are also sufficiently energetic and the average L shell fluorescent yields, ω_{Li}'s , are large enough,typically greater than 0.15, to produce a significant amount of characteristic L x-rays at the bombarding energies considered here [44].

In addition to the direct Coulomb ionization process, which is traditionally an area of study for atomic physics (although its roots lie in the concerns of nuclear physics) there is another inelastic collision process which can produce inner-sheil vacancies which are essentially indistinguishable from the vacancies produced in the processes already discussed. This process is the internal conversion of excited nuclear states [45-47]. Internal conversion, IC , is found in radioactive decay (where it was first recognized) and in a variety of nuclear excitation methods. These excitation methods can be: neutron capture and the prompt decay of the excited states formed, inelastic neutron or charged particle scattering, charged-particle capture, resonant photon fluorescence such as Mossbauer spectroscopy and nuclear Coulomb excitation. It is this last process which this study and that of other researchers who study K-Shell-vacancy cross-section determinations of the rare earth region of the Periodic Table with sub-Coulomb barrier projectiles should have the most concern about.

Briefly, this non-radiative de-excitation mechanism can be considered as the nuclear analogue of the Auger effect [48]. The similarity between the processes is that the energy of either the excited atomic or nuclear state is transferred to a bound inner-shell electron. The excitation energy transferred (dumped if you will) must be larger than the the binding energy of the the electron participating in the process. Thus the ejected electron

(either Auger or IC) will have sufficient kinetic energy to be transported to the continuum. Because both processes take place in a single step, the energy is not shared by other electrons, (ignoring any shake processes) but is emitted with a definite energy per decay. Both processes have been used to study the bound-state energies of atomic levels and both processes are presently used in condensed matter studies as well [49,50]. Auger and IC electrons have characteristic shapes and intensities that indicate the type of transition (in the case of IC electrons they provide information on both the atomic and nuclear levels) as well as the type of atom from which the transition arose. The ratio of conversion electrons emitted to the number of gamma rays from a particular decay of a nuclear state is defined as the internal conversion coefficient, ICC , and is designated by α . The amount of conversion taking place from all the electronic shells or, subshells, contributing relative to the emission of a gamma ray is termed α_{tot}. The relative amount of conversion electrons emitted from a particular shell or subshell is defined by α_K, α_{L_1}, α_{L_2}, etc. The concept of an ICC can be thought of as the inverse analogue of ω in that the ICC has the number of electrons emitted in the numerator relative to the total amount of nuclear excitation while the ω's have the the number of photons emitted in the numerator relative to the number of total vacancies produced and which remain in that subshell or shell.

The subsequent atomic cascade following the formation of a vacancy produced by IC is to first order, independent of any of the details involving the structure of the particular nucleus which has undergone a transition. Energies, intensities, and linewidths of the resulting x-rays or Auger electrons emitted are strictly dependent on the characteristic atomic par-

ameters relevant to the decay of the excited nuclear state. Indeed, radioactive sources that emit x-rays and Auger electrons from the IC channel as part of their decay have long been used to determine values of Coster-Kronig transition rates, f_{12} , f_{13} , f_{23} , Auger rates and energies etc. [51,52].

The values of α_{tot} and α_K, α_{L_1} etc. are strongly dependent on several factors such as: the atomic number of the nuclide undergoing the transition, the energy of the state involved, and the multipolarity of the transition. We will see in the theory section that these factors are important in basically two aspects; the total lifetime of the excited state and how close to the nucleus an orbital electron can come in that particular atomic system.

The multipolarity of the state is designated either ML or EL where M stands for a magnetic and E stands for an electric transition, and L represents the change in the angular momentum in the transition. For mixed transitions with a fixed percentage for each contributing multipole, the value for the ICC can be calculated from theoretical values for the pure multipoles by taking the linear sums of the ICC's for the pure multipoles of a given energy and Z [53-55]. This can be done because there is no interference between the different phases in terms of intensity (amplitude) i.e., they add incoherently. However, the phases are coherent in terms of angular correlation or distributions, and anisotropies can be measured for IC electrons well as for gammas rays. In fact one of the major ways of experimentally determining the value of the mixing ratio, δ , the relative amounts of ML and EL multipolarity of a given nuclear transition (ML and EL must of course have the same parity if they are to mix, E1 and ML-1

have the same parity) is to measure the relative amounts of conversion taking place from the various atomic shells or subshells [56,57]. In nuclear transitions by far the most common mixing is between M and E multipoles involving M1 and E2. This fact will be of particular importance in this thesis especially for the odd-A elements of nuclides whose K-shell cross-sections were measured.

In general, we can predict that the values of α_{tot} will be strongly dependent on the following factors: a) As the value of Z increases, the value of α_{tot} will increase for a given transition energy, k. b) α_{tot} will increase for a given Z with decreasing vales of k. c) α_{tot} will vary for a given Z and k for different multipole values. The higher the value of L, the larger the value of α_{tot}. d) Magnetic transitions will be more converted than electric ones of the same parity in the absence of any of the nuclear structure effects that will be discussed later on.

If there is some nuclear structure factor that prolongs the lifetime of the nuclear state, i.e., some type of isomerism, then for a fixed Z, k or given multipolarity, there will be an increase in the value of α_{tot} as compared to the "normal" transitions, as well as in large shifts in the L subshell conversion ratios from the "normal" ratios that can be calculated without any considerations of the details of the structure of the nucleus involved in the transition undergoing conversion.

In this last regard, additional consideration must be given to the nuclides with strong permanent ground state deformations, those in the region $150 < A < 190$ and $A > 224$. These "rotational" nuclides, so-called because they have an energy level structure similar to the structure found in the eigenspectra of diatomic molecular rotation, have rotational bands that are

best described using Nilsson's asymptotic quantum number, N and Λ , need to be considered in addition to the more generalized factors for IC. These nuclides may have transitions which involve changes in N, these are the so-called K forbidden transitions which are typically quite hindered [60], which result in deviations from the "expected" values of the ICC. Changes in Λ lead to "anomalous" values of the ICC, either in the value of α_{tot} or in the subshell ratios for the ICC [61]. This last effect is found predominantly in either M1 or E1 transitions in the type of nuclides described above.

The bombarding energies available from the Brooklyn College Dynamitron and the large Z values of the elements studied in this thesis together preclude the excitation of nuclear states where either of the situations affecting "normal" IC needs to be considered. Due to the heights of the classical Coulomb barriers involved, the only possible nuclear excitation that can take place is Coulomb excitation [62-64].

Significant Coulomb excitation cross-sections, σ_{CE}, for light, slow ions can be found only in the case of E2, electric quadrupole excitations. This category of E2 excitations are greatly enhanced in the strongly deformed nuclides previously mentioned. These nuclides lie in regions between the closed-shell nucleon configurations, and as such, have spheroidal shapes for the ground state. The enhancements in transition probability are as much as 100-200 times larger than expected from models of single particle excitation, and are due almost entirely to the collective nature of these types of nuclides.

The excited nuclear levels associated with collective motion are typically of relatively low energy. Analogous to the molecular case, it is well established that rotational excitations typically require less energy than vibrational excitations which are, in turn, less energetic than typical electronic electronic excitations. Extending the same argument, only now for nuclear states, we find that nuclides which are spheroidal in shape possess excitational modes of very low frequency (low energy) that are connected to each other via E2 transitions. E3 and E4 transitions are also enhanced in these rotational nuclides although of significantly smaller magnitudes than the E2 transitions and especially when light projectiles are used.

Cross-sections for CE are directly dependent on the value of the reduced transition matrix element for E2 excitation, B(E2), which is significantly larger in these deformed nuclides then in the spherical (single particle) nuclides. Using experimentally determined values of B(E2) in specific nuclides it is possible to calculate in a relatively simple way the value of σ_{CE} at a particular bombarding energy and for a given projectile [65]. This is of course an accurate calculation as long as the projectile is not very large. It still can be considered as causing a small perturbation and is sufficiently low in energy not to interact with the nucleus directly (the short wavelength approximation). For protons however, this short wavelength approximation is not a completely accurate picture. The wavelength of even MeV energy protons is sufficiently long that it allows for penetration of the proton into the classically forbidden region, i.e. into the region beyond its classical turning point. Regions of nuclear deformation are found throughout the Chart of the Nuclides.

In reality all nuclides are deformed somewhat, except for those that have completely closed shells such as most of the Pb and Sn isotopes. However, the regions midway between the closed shells exhibit the greatest degree of deformation and therefore have the largest nuclear static quadrupole moments (nuclei are forbidden from having ground state electric dipole moments). This is true as well for even-A nuclides which have 0+ ground states. The level spacings for the nuclides which are most like rigid rotors are typically on the order of 50-100 KeV with B(E2)'s connecting them on the order of 100-200 times what a single particle excitation estimate would give.

Due to the presence of three of the four main factors which contribute to a high degree of conversion in a nuclear transition, namely high Z, (60-74), low k (ca. 100 KeV) and either pure E2 or M1/E2 de-excitation, the same states that are relatively easy to produce from Coulomb excitation are also highly converted. Not only are these states highly converted, but they are highly K-shell converted, meaning that K x-rays are a common radiation produced from charged particle bombardment not only from the atomic collision channel but also (and with comparable intensities) from the inelastic nuclear channel. K x-rays from both channels are indistinguishable and the only signatures in the photon spectra that would indicate that two channels were present would be the increased yields of K x-rays and the recording of low-energy γ-rays from Coulomb-excited states that were not converted. Indeed, it was a scenario very much like this one, some 35 years ago, that was directly responsible for the seminal Coulomb excitation studies and in an indirect way, for the revival of interest in inner-shell collision phenomena.

It is because of the fact that the very large majority of nuclides in the rare-earth region are strongly deformed (having the two K x-ray production channels) and that for low bombarding energies typical of most small research accelerators, that the nuclear channel not only is competitive with the atomic channel but in some cases can be the dominant one depending on the projectile used and the energies available. An experimenter wishing to perform measurements of K-shell ionization probability for these elements is faced with the task of collecting x-ray spectra that are not a true indication of the process he had intended to study. Needless to say, this is not the optimal position an experimenter would like to be in, especially since it further requires a considerable amount of thought and calculation (and some approximating as well) in order to arrive at some reliable and accurate results. We have assumed that the awareness of the two channels was commonplace among those experimenters in the K-shell ionization field. Yet there have been studies (and published results) [66,67] done in the region of the Periodic Table mentioned already using projectile energies which warranted attention to the Coulomb excitation process but in which these complications were apparently overlooked by the experimenters.

It is revealing to recognize that this problem has existed for experimenters for over 30 years [68]. However, at that time, the context of the experiments were in the realm of seminal nuclear CE experiments. Given the inherent proximity of the K x-ray and the CE γ-ray energies for many of the rare earths and the relatively poor resolution of the NaI scintillation detectors used, it was important to accurately calculate σ_{KI} for the pure atomic channel (again only the direct channel is important) for the

bombarding energies and the projectiles most frequently used in nuclear CE experiments. B.Mottleson encouraged E.Merzbacher [69] to pursue the problem of calculating the values of σ_{KI}. Merzbacher's involvement in the field of inner-shell ionization led to his Plane Wave Born Approximation, (PWBA), which can be considered the first accurate "modern" theory to give reliable values [70].

Merzbacher's developments were followed by Bang and Hansteen's semi-classical approximation, SCA, [71] which treats the projectile's trajectory as being classical i.e., following Rutherford orbits with the wavelengths of both the target electrons and the projectile being too short to interact with each other. This is the identical framework that was used by Bohr and Alder to describe the nuclear Coulomb excitation problem with the appropriate modifications put in, to account for the differences between the nuclear and atomic systems.

It is interesting to consider that the same theoretical framework which works very accurately to predict the values of σ_{KI}; is also at the present time, (recent developments will be outlined in more detail in the Theory section of this thesis) the most accurate for calculating the values of σ_{KI}. This is especially true in the adiabatic collision region which is responsible for the largest relative contributions to the K x-ray yields from the IC channel (via the CE process) in deformed nuclides. In a way, this can be thought to be a consequence of the naturalness built into the SCA description of the inelastic collision process whether it be in the nuclear or the atomic system.

An important modification to the PWBA was proposed by W.Brandt [72]. Recognizing a need to improve the PWBA in the adiabatic region, Brandt cast

Bates' perturbed stationary state ansatz, PSS, into a PWBA-type approach. This development along with a series of second-order perturbations which play very significant roles in altering the probability for collision with inner-shell electrons leads to good agreement with experimental values of σ_{KI} for a good portion of the collision regime [73].

A final theoretical development, the Binary Encounter Approximation, BEA, of J.D.Garcia [74] gives excellent results (as do the PWBA and the SCA) for sudden collisions (i.e. high velocity). The BEA or impulse approximation treats the interaction between the projectile and the target inner-shell electron exactly, and not as a perturbation. Since its inception, the BEA has gradually become less popular in its use, and although modifications have been made to improve upon its limitations, at the present time it is not as widely used as the previously mentioned theories. In this thesis, attempts to measure with a higher degree of precision the dependency of σ_{KI} on bombarding velocity for elements in the region of strong nuclear deformation will be described. One strategy, and one that has not been used very often, is to choose, wherever possible, isotopes of an element that is not strongly deformed [75]. That has been done in this study by selecting isotopes of Nd and Sm, both of which straddle the strong deformation region. Both elements are multi-isotopic and are at the very onset of nuclear deformation so there exist isotopes of both elements which run the spectrum from spherical (non-rotational) to spheroidal in shape. The general trend in this region is that the smaller A isotopes are the spherical ones while the heavy isotopes are spheroidal. The isotopes chosen were Nd-142 and Sm-150.

In order to have a more complete study of cross-section behaviors in the rare-earth region, it was necessary to include elements that are farther away from the onset of permanent nuclear deformations. This means that none of the isotopes for the multi-isotopic elements are spherical and therefore a substantial amount of the K x-rays detected have as their origins the IC channel. Not only does this require having to make corrections for the nuclear channels, it also increases the complexities and uncertainties in data analysis. There are two reasons for the increased complexity and uncertainty: a) Some of the isotopes studied are odd-A; therefore, arriving at a reliable value of the ICC for the M1/E2 transitions as well as correcting for the anisotropic emission of the CE γ-rays is not a trivial concern. b) The mono-isotopic element Tm-169, which was studied, can not have the values σ_{CE} calculated accurately using the first-order formalism this is because of an extremely low lying first excited state at 8.4 keV which is very easily populated. This requires a more sophisticated coupled channels approach (requiring a computer code) in order to calculate the correct σ_{CE} for the higher states which are also Coulomb excited and K converted in their decay. This departure from the first-order theory will be discussed in more detail in the Chapter II. and in Chapter V.

In addition to the previously mentioned Nd-142, Sm-150 and Tm-169 the other elements studied were: Pr-141 (mono-isotopic) and non-deformed, natural W and Ta-181 (mono-isotopic) both of these elements contain only strongly deformed nuclides. An important consideration for choosing these particular elements was the development of a new normalization technique involving the detection of the $L\gamma_1$ and $L\gamma_{2,3}$ lines of these elements while collecting the K x-rays and the CE γ-rays. The quality that all these ele-

ments share is that the $L\alpha_{1,2}$ lines of these elements are extremely close in energy to the K-Shell binding energy of a few of the transition elements, typically within 20-100 ev.

These transition elements act as "critical absorbers" for the $L\alpha_{1,2}$, to a considerable degree for the Lβ x-rays as well, of the elements that were studied. This is an important consideration because the $L\alpha_{1,2}$ and Lβ x-rays usually constitute from 85-90% of the L x-ray emission. The cross-sections for L-subshell ionization are of course much greater than the K-Shell cross-sections for a given Z and bombarding energy, so that in order to prevent large deadtime losses in the photon detector, one typically places an absorber thick enough to practically eliminate all of the L x-rays before they can reach the detector [76]. The typical absorber is some common metal like Al, Fe or Cu; no thought has been given to its electronic energy structure relative to the energies of the target's characteristic L x-rays. However, workers in the areas of X-Ray fluorescence, XRF, and in Particle Induced X-Ray Emission, PIXE, have long used critical absorbers to remove the x-rays of an element that was present in a sample in such high quantities that the minor constituent's x-rays would be either buried from "pile-up" or distorted in form, due to the large deadtimes incurred because of the high count rates from the major constituent [77]. The thickness of the critical absorber can be chosen so as to minimize attenuation of the x-rays one wishes to detect while insuring that the filter is thick enough to remove the unwanted X-ray(s).

The original strategy in choosing the critical absorber method was to minimize the attenuation of the "harder" K x-rays and γ-rays while effectively removing the many L x-ray lines of the element being studied. It

soon became apparent from the recorded spectra that while the $L\alpha_{1,2}$ and $L\beta$ lines were removed dramatically, the $L\gamma$ lines were recorded in almost all cases with the same intensity as the K x-rays of the same element. These observations led us to consider the development of a new method of normalization for the determination of K shell cross-sections.

This alternate method of normalization was patterned after another photon method of normalization that is particularly adapted to the deformed rare earth and actinide elements [78-80]. It depends on the determination of the measured yield of CE γ-rays. This requires the accurate determination of σ_{CE} for producing γ-rays, an accurate value of the detector efficiency for the gamma rays studied, making the suitable corrections for anisotropic emission of the CE γ-rays, and either using the Bohr-Alder ansatz or some coupled-channels code for the value of the σ_{KI}; (whichever is the more appropriate approach given the targets and the projectile type and energies). Implicit in this approach is the use of sufficiently deformed nuclides so that the yield of CE γ-rays is large enough to measure. This of course is contrary to any attempt to either limit or to eliminate entirely the contributions to the K x-ray yields from the IC channels.

There are a number of advantages in using a photon method ofnormalization to obtain experimental values of σ_{KI} as opposed to the more "traditional" means of normalizing the K x-ray yields. These methods are well established in both nuclear and atomic accelerator-based physics and involve either an acurate way of measuring the incident beam current in the target or by measuring the yield of charged-particles undergoing Rutherford scattering at some fixed backward angle.

The advantages of using a photon method of normalization are the use of a single photon detector and the ability to perform cross-section measurements in a geometric arrangement which may be unacceptable for RBS, Rutherford Backscattering spectroscopy. As well as possible situations when the incoming projectile is above or sufficiently close to the Coulomb barrier so that nuclear scattering (either elastic or inelastic) is a distinct possibility. Under these bombarding conditions, the use of the well known Rutherford formula for predicting the angular dependence for the intensity of the back-scattered porjectiles is quite inaccurate.

In that case an unraveling of the particle spectrum may be extremely difficult for normalization purposes. Especially in the cases of resonant scattering and for multiisotopic elements such as the rare-earths. An experimenter would be forced to either do some extremely complicated computer calculations to obtain the proper nuclear scattering amplitudes and use those for normalization purposes or restrict himself to one particular isotope and measure the angular dependence of the nuclear scattering or rely on previously published experimental or theoretical results.

In regard to the CE γ-ray normalization; it suffers from the large IC contribution and its limited applicability in the type of elements it is suitable for, it also suffers from the same limitations that the RBS method has in terms of not being reliable at bombarding energies close to the nuclear Coulomb barrier. At these energies the excitation process is not strictly electromagnetic and the SCA formalism no longer is valid. The experimenter is faced once again with the same types of choices (further complicated by the prospect of interferences between CE and nuclear amplitudes) as described in the previous paragraph.

The LY x-ray normalization method does not have these limitations since the L subshell cross-sections do not appear to be altered considerably for energies near or above the Coulomb barrier. It is also not limited to the deformed region of nuclear shapes and as will be shown in greater detail in the Experimental Results Section of this thesis where the other normalization methods are compared directly, it offers a higher degree of accuracy and reproducibility than the CE method because the peak heights using protons as projectiles are much higher for the LY x-rays than are the CE Y-ray peaks.

The cross-sections for LY x-ray production can be obtained from three distinct sources: a) They can be calculated from the theoretical values of L subshell cross-sections and can then be converted to L x-ray production cross-sections knowing the branching ratios, fluorescent yields and Coster-Kronig transition rates of the transitions involved. b) They can be taken from previously measured values in the literature, whether for vacancy or x-ray production. If the vacancy production cross-sections are used, the same conversion as described in a) can be used. c) They can be measured by the experimenter as a prelude to the K-shell measurements. Of course, for an absolute measurement the absolute efficiency of the photon detector is essential for both K and L-subshell cross-sections.

All three approaches were taken in this thesis and a direct comparison is made in a "self-consistent" way. The difficulties and uncertainties are discussed for the various normalization methods and the applicabilities and limitations for each method are also discussed.

Chapter II. Theory

This thesis involves measuring experimentally the photon emission produced by three distinct phenomena associated with charged particle excitation. These phenomena will be discussed within the context of the current theories which have shown the greatest degree of accuracy in predicting cross-sections or total yields of photons as well as parameterizing the interactions and the dynamics.

The phenomena to be discussed theoretically are: a) Inner-shell vacancy production by charged-particle impact; restricted to the direct ionization theories b) Nuclear Coulomb excitation c) Internal conversion of nuclear excited states. Theories concerning b and c have been adequately described in essentially "complete" form [1,2]. There is no true competition from alternate theories in terms of providing more accurate or speedier results. Though there are some cases where a more refined and developed theoretical approach is necessary, these are taken more in the nature of modifications rather than as a reformulation of the problem. The modifications will be discussed briefly for the purpose of understanding where they may be needed to obtain more accurate experimental results.

On the other hand, the major theories of atomic inner-shell ionization do not share this "completeness". First, they do not give calculated cross-sections of significant accuracy when compared to the measured ones [3]. This is most noticeable in the adiabatic regime. Secondly, their success is restricted to the asymmetric region of collisions [4]. Thirdly, while they deviate from each other as to their degree of accuracy in predicting cross-

sections, they all can be shown to be reducible to identical or nearly equivalent descriptions under certain sets of conditions [5].

One important aspect of all the inner-shell ionization theories which has a definite influence on the applications of calculated values of σ_{KI} is the "scaling law" behavior that is built into all the theoretical models. In fact, the ability to scale ionization cross-sections as functions of several reduced parameters (whose properties are to be discussed in more detail below) enables calculations to be made in a very consistent and reliable way for many collision systems. This is due to the periodicity of the energy levels of atomic systems and the long range and well-behaved nature of the Coulomb interaction especially in regimes where first order perturbation is a valid approach.

A. Theories of Inner-shell Ionization by Charged-Particle Impact

The major theories at the present time are: 1. The Plane Wave Born Approximation, with Relativistic, Binding Energy and Coulomb Deflection Corrections (RPWBA-BC) 2. Perturbed Stationary State with Energy Loss Coulomb Deflection and Relativistic Corrections (ECPSSR) 3. Relativistic Semi-Classical Approximation (RSCA).

1. RPWBA-BC

We start with the first Born approximation, FBA, to describe the ionizing collision. The plane wave approximation idealizes the trajectory for both the incoming and outgoing projectile as a plane wave.

For a target atom's inner electron, the nuclear Coulomb potential is reduced by the effect of screening from the other inner electrons. Assuming hydrogenic wavefunctions, the amount of screening can be approximated by using the appropriate Slater correction term for the given shell. The correction term, C_S , has a value of 0.3 for the K shell and 4.15 for the L shell. The screened potential, Z_{scr} ,is given by:

$$Z_{scr} = Z_S - C_S \tag{1}$$

The energy of a level with principal quantum number n,(n=1 for K, n=2 for L etc.) is given by the Bohr formula:

$$E_S = Ry \frac{Z^2}{n^2} \tag{2}$$

with Ry standing for the Rydberg constant

Next the classical electronic velocity, v, is defined by:

$$v = (2E_S/m)^{1/2} = v_o Z_{scr}/m \tag{3}$$

The average electron radius can be defined by:

$$r_s = \frac{a_o n^2}{Z^2_{scr} Ry} \tag{4}$$

with a_o being the Bohr radius; in MKS units, $a_o = 5.29 \times 10^{-9}$ cm. In atomic units, a_o, v_o and $2 \cdot Ry$ are also given values of unity.

A more realistic value of the binding energy, U_s, which is usually taken from the experimental value of the binding energy can be used to define a reduced "universal" binding energy given by Θ_s, which is defined by:

$$\Theta_s = (E_s / Z^2_{scr} Ry) \tag{5}$$

After considering the target parameters which influence the cross-section's behavior, we consider the projectile parameters in a first-order approach. The important considerations are the projectile velocity relative to the inner electron velocity which will be ionized, and the projectile atomic number.

No screening effects are considered for the projectile charge [6]. In the asymmetric region, light ions, even with electrons on them, have electronic radii which are larger than the radii of the target's inner electrons. So that for light ions carrying electrons, their electronic clouds do not affect collision process.

An important parameter is the reduced ion energy, η_s , and is given by:

$$\eta_S = \frac{v_1^2}{Z^2_{scr} v_0} \tag{6}$$

The inclusive cross section in the PWBA for inner shell ionization is given by:

$$\sigma_S = \frac{8\pi r^2 Z_1^2}{Z_2^2 \eta^4 n} \cdot f_S(\eta_S, \theta_S) \tag{7}$$

The function f_S, has been tabulated [7] for various values of η_S, and θ_S. For small values of η_S/θ_S, a more convienent form of f_S can be used to calculate σ_S by the following identity:

$$\frac{\eta_S}{\theta_S} f_S(\eta, \theta) = \frac{\theta_S^2}{f_S} \cdot f_S\left(\frac{\eta_S}{\theta_S, 1}\right) = F_S\left(\frac{\eta_S}{\theta_S}\right) \tag{8}$$

The differential cross section as a function of the ejected electron energy following Madison and Merzbacher [8] is:

$$\frac{d\sigma}{dE_f} = \frac{4\pi}{h^2} \frac{Z_1^2 e^4 M}{E_1} (2j+1) \frac{\int dq}{q^3} |F_S(q)|^2 \tag{9}$$

The new terms in eqn.(9) are: E_f - the ejected electron's kinetic energy, hq - the momentum transfer, 2j + 1 - the statistical factor for the bound atomic electrons contributing to the ionization process

a. Relativistic Effects

Moving out of first order PWBA, we introduce the relativistic effect on the target's inner electron wavefunctions. A relativistic form factor is needed to characterize the electronic states. Important considerations in the decision to use relativistic wave functions especially for the types of high Z elements discussed in this thesis are: 1). Dirac-Hartree-Fock wavefunctions give a more accurate momentum distribution for inner-shell electrons particularly near the nucleus. The relativistic wave functions "peak" the electronic density nearer the nucleus than non-relativistic wave functions do. This has an important effect in allowing larger momentum transfers in close collisions, thereby giving larger probabilities for ionization than would be expected from non-relativistic momentum distribution. 2). The increased mass of the target electrons due to their high velocities.

The states are defined by the quantum numbers l_i, j_i, (j-j coupling must be used when relativistic effects are incorporated) for the initial (unionized) states while l_f, j_f, describe the continuum states. The relativistic form factor [9] is given by:

$$\left|F_{if}(q)\right|^2 = \Sigma(2l+1)(2j_f+1)\begin{bmatrix} j_f & 1 & j_i \\ \frac{1}{2} & 0 & \frac{1}{2} \end{bmatrix}\Pi(l_f l l_i)\left|\int j(qr)(P_i P_f + Q_i Q_f dr\right|^2 \quad (10)$$

with $\Pi(l_f l l_i) = 0$ if l_f+l+l_i = odd and $\Pi(l_f l l_i) = 1$ if l_f+l+l_i = even and P and Q are the representations of the large and small radial components of

the Dirac equation. One-electron Dirac wave functions are used. The increase in the electron mass is also considered and although a discussion of it is in the ECPSSR section it can be easily invoked for any other theory.

b. Polarization Effects

The time-varying potential formed along the axis created by the two nuclei in the collision, introduces a perturbation to the stationary state's binding energy of the inner-shell electron. This potential can act in two ways, each of which produces the opposite effect on the value for ionization probability.

The first effect is the increasing of the binding energy for the inner-shell electron. This term dominates at low projectile velocities. Given the adiabacity of the collision, the target electron finds itself in a potential of a quasi-diatomic molecule composed of both projectile and target. Large-Z projectiles moving slowly will enhance the binding energy and give lower than predicted cross sections from first-order considerations.

The second effect on the electron's potential is produced by a fast projectile, and the effect is to polarize the wavefunction in the direction of the incoming projectile. This raises the value for the cross section because the electron's binding energy is lowered as it moves out further from the Coulomb potential of its nucleus. This is termed the polarization effect and it too is proportional to Z_2.

The changes in the binding energy due to either effect is calculated by:

$$\langle \Delta E \rangle = \frac{2Z_1 E_1}{Z_{scr}\Theta_S[g_S - h_S]} \tag{11}$$

ΔE represents the binding energy correction whose change depends on the values of g_S and h_S. When g_S (the binding effect) dominates, the binding energy is increased and the cross section goes down. Conversely, it can be seen that if the term h_S dominates, the binding energy, will go down and therefore h_S is a good indicator of the importance of the binding effect.

The functional forms of g_S for the K shell and for the L_1, L_2, and L_3 subshells are tabulated [8]. The adiabacity, ξ_S, is given by:

$$\xi_S = \frac{v_1}{\Theta_S v_S} \tag{12}$$

The function h_S is given by:

$$h_S = \frac{2n}{\Theta_S \xi^2_S} I\left(\frac{C_S n}{\xi_S}\right) \tag{13}$$

C_S equals 1.5 for the $s_{1/2}$ orbitals (K,L_1) while it equals 1.25 for $p_{1/2}$ and $p_{3/2}$ subshells (L_2,L_3).

c. Coulomb Deflection

The final correction to be made is the deviation from a straight line trajectory by the projectile's approach. The corrected cross section is then just the product of the first order cross section and the term for

deflection by the Coulomb field of the target nucleus. The Coulomb correction term is given by: eqn. (14) as found in [9].

for $s_{1/2}$ subshells

$$C(2a_o q\zeta_s)/(z_s(1+z_s) = 9\mathcal{E}_{10}(2\pi a q_o \zeta_s)/(z_s(1+z_s) =$$

$$11\mathcal{E}_{12}(2\pi a q_o \zeta_s/z_s(1+z_s) \qquad (14)$$

$\zeta_s = 1 + \langle \Delta E_s \rangle / E_s$ takes into account the change in binding energy

z_s - is a factor involving the energy loss of the projectile during the collision process, a - is the half distance of closest approach between the nuclei, $\mathcal{E}_n$ - is the exponential integral of order n.

The Coulomb deflection term is most important for light, slow, moving projectiles. The energy loss term is particularly critical for close, adiabatic collisions of the kind studied in this thesis. It is intriguing to speculate as to the effect on either the inclusive or the differential σ_{KI} values when inelastic nuclear and atomic collisions are taking place with nearly equivalent ξ's and scattering amplitudes.

2. ECPSSR

ECPSSR has many features in common with RPWBA-BC. Fundamental of course is PWBA as its starting point [10]. Given the similarities between the two, redundancy will be avoided in outlining the identical approaches to the correction terms. More detail in describing the effects will be

provided in this section.

The term, z_S , introduced in the last section is given by:

$$z_S = \left[1 - \frac{4}{M\zeta_S\theta_S(\frac{\zeta_S}{\xi_S})^2}\right] \tag{15}$$

here M is the mass of the target in atomic units

The change in the inner-shell electron mass is denoted m^R and is given by eqn. (16): $m^R = (1 + 1.1\, y^2)^{1/2} + y$

with:

$$y = \frac{0.4(Z_{Scr}c^{-1})}{n\xi_{K,L_1}} \tag{16a}$$

for $s_{1/2}$ orbitals

or by:

$$y = \frac{0.15(Z_{Scr}c^{-1})}{n\xi_{L_2,L_3}} \tag{16b}$$

for $p_{1/2}$ and $p_{3/2}$ orbitals

using of course the appropriate values of ξ for the orbitals under consideration

Including the previously mentioned correction terms, the transformation from PWBA to ECPSSR is accomplished by modifying η_S and θ_S respectively and by replacing them with $m^R(\xi/\zeta)\eta_S$ and with (ζ_S,θ_S). We arrive at the ECPSSR cross section using eqn.(17):

$$\sigma^{ECPSSR} = C^{E}(aq_o,\zeta_S)\sigma^{PWBA}[m^{R}(\xi/\zeta)n(\zeta_S/\Theta_S{}^2),^{-1}\zeta_S,\Theta_S] \tag{17}$$

3. RSCA

The starting point for the RSCA is the assertion that the DeBroglie wavelengths for projectile and target electrons are too small to interact or overlap. A single condition used to insure this given by eqn.(18) for the parameter, η, it was first used by Bohr [13].

$$\eta = \frac{Z_1 Z_2 e^2}{h v_1} >> 1 \tag{18}$$

here e is the fundamental unit of electric charge and h is Plank's constant divided by 2

When this condition is imposed on the projectile motion then the trajectory can be described as a hyperbola. Alternatively, one can speak of the trajectory as a Rutherford or classical orbit.

A "symmetrized" Rutherford orbit can be characterized by its scattering amplitude, $f_c(\Theta)$ and given by eqn. (19):

$$f_c(\Theta) = -\frac{a}{2\sin^2\frac{\Theta}{2}} [\exp(2i\sigma_o(\eta) - \frac{\eta\sin\Theta}{2}] \tag{19}$$

where θ is the angle through which the projectile is scattered.

The symmetrization process is important because it selects the proper Rutherford trajectory between the incoming and the outgoing projectiles. This is a result of the quantum mechanical aspect of the problem (as we would expect from using a scattering amplitude to describe the probability for ionization) since frequency associated with the moving projectile (which can be defined in a classical sense) has strong significance in the quantum aspects of the excitation process as well.

This symmetrization has important ramifications for both the atomic and nuclear applications because the predicted cross section values will be in error if the proper Rutherford orbits are not selected [14]. The correct trajectories insure that the classical frequencies are matched to an equivalent frequency which is a transition frequency of the system [15].

This brings up the important point that although for a great many cases the underlying quantum mechanical considerations of the ionization (or for the nuclear case as well) are not always exploited, they can be brought into the analysis when necessary. As an example of this, consider the SCA description for the ionization process using a full T-matrix (transition matrix) approach which can be expressed in eqn.(20) following from [16].

$$T_{fi} = \langle \chi^{-}(R)\phi^{-}(r) | V_{int} | \psi^{+}(r,R) \rangle \qquad (20)$$

Where the scattering wave functions of the projectile and the ejected electron are given by:

$\chi^{-}(R)$ (20a)

$\phi^{-}(r)$ (20b)

The interaction potential, $V_{int}(r,R)$ is determined from

$$V_{int}(r,R) = V_{pt}(R') - V_{pt}(R) + V_{pe}(r') \qquad (21)$$

The wave function, ψ^{+}, for the bound initial state is a solution for the Hamiltonian of the total system which is defined by:

$$H_{tot} = T_{kin} + V_{pt}(R) + V_{pe}(R') + V_{pe}(r) \qquad (22)$$

here H_{tot} stands for the Hamiltonian for the total system. T_{kin} is the kinetic energy operator for the projectile, the target atom as a whole (important if we want to include recoil effects) and for the ejected electron, V_{pt}, V_{pe} and V_{te} stand respectively for the various interactions that take place between the projectile, the target and the electron.

In order to insure that the perturbation is a small one, (which is not always justified as we have seen from the preceding sections) and it is legitimate to use first order perturbation, we limit the projectiles to atomic numbers so that $Z_1 << Z_2$ or the asymmetric limit. In the spirit of first-order perturbation, we also require that $\Delta E/E << 1$. Equations (23a,b)

give the relevant equations for defining the proper energy and momentum transfer.

$$hq_o \approx \frac{\Delta E}{v_i} \tag{23a}$$

$$\Delta E = E_{scr} + E_f \tag{23b}$$

As a start to the SCA for ionization calculations, the formula for the differential cross section as a function of energy transfer is given by:

$$\left(\frac{d\sigma}{dE_f}\right) = 2\pi h^{-2} \int_o^\infty P dP \int^\infty e^{i\omega t} dt \left|\langle f|V(t)|i\rangle\right|^2 \tag{24}$$

with P as the impact parameter characterizing the collision, V(t) is the time dependent potential of the evolving states and ω the frequency of the time-varying field induced by the motion of the projectile which is given by:

$$\omega = (E_f - E_i)h^{-1} \tag{25}$$

An alternative way to write the SCA cross-section (and one which appears similar to the PWBA) is:

$$\frac{d\sigma}{dE_f} = 2\pi h^{-2} 2aZ_1^{\,2} e^4 \int_0^\infty \varepsilon d\varepsilon \left| \int_0^\infty dt e^{i\omega t} \langle \psi | (r-R(t))^{-1} | \psi \rangle \right|^2 \tag{26}$$

where ε is the eccentricity of the Rutherford orbit which is given by eqn.(26a)

$$\varepsilon = (\sin^2 \frac{\Theta}{2})^{-1} \tag{26a}$$

It is revealing to recognize at this point that when the conditions are reversed such that $\eta >> 1$, then the identity eqn.(27) is found. A straight line is found to be an adequate description for the trajectory.

$$(\frac{d\sigma}{dE_f})_{SCA} \approx (\frac{d\sigma}{dE_f})_{Ruth.} \tag{27}$$

The ionization probability, I_p, is introduced in the form of:

$$I_p = \int^\infty (\frac{d\sigma}{dE_f}) dE_f \tag{28}$$

It is worth mentioning at this time that the SCA gives reliable values for the impact-parameter dependence of ionization as well as the number of partial waves contributing to the ionization process, i.e. the multipole character for the transitions.

Combining the classical part (Rutherford orbit) with the quantum mechanical part (the frequency and the multipolarity of the ejected elec-

tron) one can arrive at the differential angular cross-section

$$\left(\frac{d\sigma}{d\Omega}\right)_{SCA} \approx I_p\left(\frac{d\sigma}{d\Omega}\right)_{Ruth.} \tag{29}$$

The adiabacity parameter, ξ, is reinterpreted by:

$$\xi = \frac{Z_1 Z_2 e^2}{M_0 v_1^2} \frac{\Delta E}{h\nu_1} \tag{30}$$

where M_0 is the rest mass of the proton and where we specify the following to be true at threshold defined by:

$$\xi = \xi_0 \quad (30a) \quad \text{and} \quad E = 0 \quad (30b)$$

The connection between the hyperbolic and straight-line trajectories is then made by:

$$\left(\frac{d\sigma}{dE_f}\right)_{hyp} = \exp{-\pi\xi}\left(\frac{d\sigma}{dE_f}\right)_{st.line} \tag{31}$$

This is true for the inclusive cross-section as was first demonstrated by Kocbach [17] and is defined by:

$$\sigma_{hyp} = (\exp{-\pi\xi})\,\sigma_{st.line} \tag{32}$$

Additional restrictions for the replacement of the hyperbolic orbits with the straight-line trajectories are made through:

$$hq > a^{-1} \quad (33a) \qquad q_0 > k \quad (33b)$$

where k stands for the wave number of the ejected electron

Screened Slater potentials are used as they were for the other two theories of ionization. Multipole transitions higher than monopole, that is $\Delta l = 1,2..$etc. are evaluated and are found to make important contributions to the total probability for ionization, especially for close collisions. Their inclusion in the amplitude for ionization is even more critical for predicting the behavior of the differential cross sections then for predicting the inclusive cross sections. This comes about as a natural consequence of the impact parameter dependence of the amplitudes built into the SCA.

In this last regard, an important parameter, r_{ad}, or the adiabatic radius, is an extremely useful means of understanding the collision dynamics, especially for very adiabatic processes. Since it not only expresses the momentum transfer involved in the ionizing collision, but it also gives an indication about the distance the ionizing collision takes place relative to the unperturbed K-shell radius of the target. Equation (34) defines r_{ad}:

$$r_{ad} = \frac{1}{q_o} = \frac{h\nu_1}{\Delta E} \tag{34}$$

The main contributions to the values of the inclusive cross-section come from the momentum transfers that take place at the particular value equal to r_{ad} for the collision system investigated. Therefore it follows that:

$$p_{max} = r_{ad} \tag{35}$$

For collisions with $\xi > 1$, $r_{ad} > r_s$ while for $\xi < 1$ we have $r_{ad} < r_s$

These properties can be demonstrated as shown by:

$$\xi = \frac{h\nu_i}{E_{scr} r_s} = \frac{r_{ad}}{r_s} \tag{36}$$

One of the major successes of the SCA is its ability to predict the impact parameter dependency for a wide variety of collision systems such that the inclusive cross-section can be expressed by:

$$\sigma_s = 2\pi \int I_p P dp \tag{37}$$

Relativistic electron form factors have been used by Trautmann [18] and by Amundsen [19]. Relativistic Hartree-Fock wave functions have also been used by Jakob [20] giving more realistic momentum-space configurations during collisions. It has been shown [21] that the change in binding energies of the inner-shell electrons is roughly equal if hydrogenic relativistic wave functions are used instead of the Dirac-Hartree-Fock calculations.

The Coulomb deflection term is not needed as an addendum to the SCA calculations since the trajectory is calculated exactly along the ionization path. This approach maybe more tedious, but it is more exact and versatile in its applications.

Kocbach [22] has shown that in addition to providing the proper trajectory, the SCA can also correct for the binding changes. This is done by

using the time-dependent Schrodinger equation with time-varying adiabatic changes for the target electrons. He has shown that by evoking Bate's Generalized Distortion Approximation, (GDA), the accurate detailed behavior of both the L subshell cross-sections and of L subshell alignment can be calculated in the SCA approach.

B. Nuclear Coulomb Excitation

We will see in this section that many of the concepts introduced in the RSCA will be reinvoked. Therefore, those concepts which are practically identical, will be glossed over, while those concepts which are different or unique to nuclear Coulomb excitation will be discussed in some detail.

The basics concerning the projectile description as following a Rutherford orbit remain intact. In addition, the condition of nonoverlap of the projectile's wavelength will be extended to the nuclear wavelength so that only electromagnetic forces will be involved. This simplifies the process quite a bit while adding some important symmetries inherent in the Coulomb field.

One will see the same symbols as commonly used in the atomic collision theories. By and large they are identical in meaning as in the RSCA but have very a different significance in the RPWA-BC and ECPSSR. This is unavoidable, and thus, an understanding of, and a familiarity with the two applications of the SCA is the only prevention against a complete sense of confusion.

Rutherford orbits are again assumed for the projectile, and the Bohr condition (which has a strong connection to the Sommerfeld parameter) is a criterion for assessing the SCA's validity for nuclear Coulomb excitation. The quantum mechanical nature of the process is introduced by:

$$b_{if} = (h)^{-1} \int e^{i\omega t} \langle f | H_{int}(t) | i \rangle dt \tag{38}$$

where b_{if} represents the transition probability and the time dependent Hamiltonian for nuclear excitation.

The adiabacity of the nuclear excitation is described by ξ, given by:

$$\xi = \frac{E_f - E_i}{h\omega_c} = \frac{Z_1 Z_2}{h v_1} \frac{\Delta E}{2E} = \eta_f = \eta_i \tag{39}$$

where η_f is the final value and η_i is the initial value of the Sommerfeld parameter, E_i, E_f are the initial and final energies of the nucleus, the difference between the two states is given by ΔE and ω_c is the natural frequency for the Coulomb problem defined by eqn.(40)

$$\omega_c = \frac{v_\infty}{r_c} \tag{40}$$

where v_∞ is the projectile's velocity at infinity and r_{cl} is the distance

representing the particle's classical turning point.

The parameter ξ, can also be defined in terms of the aforementioned symmetrized orbits through:

$$\xi = \frac{Z_1 Z_2 e^2}{h(\frac{1}{v_f} - \frac{1}{v_i})} \tag{41}$$

where v_f is the final projectile velocity and v_i is the velocity of the projectile before collision.

The last expression for ξ which contains the symmetrized Rutherford orbits demonstrates the equivalence of both the classical and quantum mechanical descriptions of the projectile motion. A result of this equivalence is that the Sommerfeld parameter, η has the same interpretation in both the classical and quantum mechanical sense.

An important difference in the nature of atomic ionization relative vis-a-vis nuclear Coulomb excitation is that all partial waves contribute to both Coulomb problems; only $\Delta l = 2$ amplitudes make significant contributions in the nuclear process. This reflects the limits placed on bound-bound transitions between states of definite parity,which for nuclear levels involves E2 excitations almost exclusively. The atomic channel has $\Delta l = 0,1,2..$, excitations, and in theory there is no limit on the number of partial waves contributing coherently to ionization. Due to the finite dimensions of the atom, higher order amplitudes are not needed even in the closest collisions. It was mentioned previously that E3 and E4 transitions are observed but are less probable than E2 excitations and it is worth con-

sidering that ML excitations are not forbidden but are weaker by a factor of v/c relative to EL+1 excitations and thus at low projectile velocities are not considered.

A simple description of E2 excitation in terms of the factors influencing the magnitude of the cross section will be given in the manner of Bidenharn [14]. In order to keep the process a strictly electromagnetic one, the projectile energy must be kept below the target nucleus Coulomb barrier. This is equivalent to our description that the DeBroglie wavelengths of both nuclei are too small to interact. This is in part insured by having large values for η. The value of ξ should be kept as close as possible to zero (the sudden approximation) to increase the probability for excitation.

Along these lines, it can be shown that if ξ and ΔE are kept constant, the value of the cross section increases with larger values of the projectile charge. This is exactly the type of behavior that one expects from a first-order perturbation approach. One should bear in mind that for low velocities the first-order ionization theories are quite inadequate and therefore it is necessary to add the correction terms to get reasonable results. To our knowledge there is no low velocity region of breakdown for the first order approaches, although there are adaptations that need to be made when the probability for exciting a low-lying level exceeds unity. Recalling a similar situation from the atomic case, we have:

$$\sigma_{CE} = (1-P)\left(\frac{d\sigma}{d\Omega}\right)_{Ruth} \qquad (42)$$

For low-lying states, P can quite easily exceed unity, which is of course a physically unacceptable result. This is commonly observed for projectiles with $Z > 8$, but in the case of Tm-169, which has a state at 8.4 KeV, this state could become populated with a probability of greater than 1 using a first-order excitation approach to calculate the excitation cross section.

This higher-than-unity probability for excitation, makes it necessary to use a coupled-channels formalism to arrive at the proper cross-section values. Since the number of calculations involved in a coupled-channels is quite extensive, a computer code must be used. There are a number of codes that have been written over the past 20 years. The applicability of these codes depends on several factors such as: the number of states considered in the coupling scheme, the charge of the projectile and whether nuclear-Coulomb interferences need to be considered. Interference effects between the various Coulomb excited states are observed when the perturbation is no longer small. These interferences are responsible for keeping the excitation probability below unity. These effects will be discussed in more detail in the Chapter V as it relates to the subtractions that have to be made from the total K x-ray yields in order to obtain accurate values of σ_{KI}.

Recognizing the possible inadequacies of first-order perturbation, we examine the first order cross-section dependency as expressed by Bidenharn [15] for E2 excitations in the form:

$$\sigma_{E2} = \frac{2A_1 M_0}{h^2} E_1 \frac{B(E2)\uparrow}{(Z_2 e)^2} \qquad (43)$$

where $f_{E2}(\xi)$ is given by:

$$f_{E2} = 18.807\xi^{4/3}\exp -2\pi\xi \qquad (43a)$$

E is the projectile energy in MeV and B(E2) is the reduced transition matrix element for E2 excitation.

The values of B(E2) are typically taken from experimental results but can be calculated assuming some nuclear model. The expression for the E2 excitation cross-section given above is equivalent to the one derived by Bohr et al [23].

Since it is not the intent of this thesis to explore nuclear-structure phenomena in great detail, (except when the nuclear effects have an important effect either on the amount or the quality of the data collected), the data are primarily concerned with the values of σ_{KI}. That is, the discussion will be kept, by and large, to a relatively simple approach. However, it is useful to mention the nuclear collective model and the rigid-rotor model of strongly deformed nuclides. It is precisely because these deformed nuclides are so prevalent in the rare-earth region, that the nuclear properties of these elelements enter the discussion concerning the experimental determinations of σ_{KI} for the rare-earth region elements.

The model begins by drawing an analogy between low-lying nuclear states connected by successive E2 excitations in the same rotational band, and the excited rotational states of a diatomic molecule. These excited states are best described as oscillations on the surface of the nuclear volume due to the collective motion of the nucleons [24]. These oscillations are of low frequency, ω, (low energy) and are characteristic of nuclides with deformed ground states and large static quadrupole moments.

Ignoring the effects at higher excitation energies, such as Coriolis coupling and backbending [25], the identical equation used to describe the eigenspectrum of rotational molecular states can be used in the collective nuclear model. This is given by:

$$E_{rot} = \frac{h^2}{2I} J (J + 1) + \frac{h^2}{2} \left(\frac{1}{I_3} - \frac{1}{I_1}\right) \quad (44)$$

where J is the total angular momentum of the nuclear state, K is the projection of J along the nuclear axis of symmetry, I_1 is the moment of inertia along the major axis, and I_3 is the moment along the minor axis. For a symmetric rotor: $I_1 = I_2 \neq I_3$

The deformed nuclear potential which is a result of unfilled nuclear shells gives rise to an uneven charge distribution inside the nucleus. This uneven charge distribution is the reason that collective nuclides have such large static quadrupole moments, Q_0, and causes the E2 excitations to be typically enhanced by factors of 100-200 over what would be expected from solely single-particle excitation.

The value of the reduced transition matrix element for E2 excitation, B(E2), can be shown to be directly related to the value of Q_0 through:

$$B(E2) = 5/16\pi^2 Q_0^2 \langle J_i K,2,0 | J_f,K\rangle^2 \quad (45) \quad (45)$$

Given the previously stated relationship between B(E2) and the value of Q_0, it is obvious that by experimentally determining the yields of γ-rays (corrected for IC), inelastically scattered projectiles, or conver-

sion electrons, one could experimentally determine the values of Q_0 for various nuclides. This is one of the major reasons that nuclear Coulomb excitation was so powerful an experimental technique in helping to elucidate some of the systematics of nuclear structure in the 1950's and 60's.

The values of Q_0 can in turn be used to calculate a value for the nuclear deformation, β_0, given by the following:

$$Q_0 = 3(5\pi^2)^{-2} Z_2 R_0^2 \beta \, (1 + 0.36\beta + \ldots) \qquad (46)$$

where $R_0 = 1.2\ A \times 10^{-13}$ cm The variation of β_0 with neutron number was one of the more important correlations that could be made in terms of the properties of nuclides and their relationship to structure.

C. Internal Conversion of Nuclear Transitions

An important consideration in this thesis is the ability to discriminate between the two channels responsible for K-shell vacancy production. A brief discussion is justified in order to elucidate the process. We begin with the understanding that, given the energies of the accelerator used in this research, only excited states that are Coulomb excited need be considered. It should be quite obvious by now that states that are easily Coulomb excited especially in the rare-earth region are also quite heavily converted, although not always K converted.

This is helpful in recognizing the energies of the states involved and the multipolarities of the transitions involved, as well. We are concerned with excited states of less than 150 keV and which have either E2 or mixed

M1/E2 multipolarity. The transitions in the even-A nuclides are of pure E2 while the odd A nuclides are M1/E2; that is, although de-excitation is the mixed multipole, the excitation for these types of nuclides is pure E2. The mixed multipole transitions have amplitudes which add incoherently in terms of magnitude but do mix in terms of angular and directional effects. It is because of these last two conditions that measuring the ICC's for various nuclear transitions has always been so valuable in assigning spin and parity [26].

For both pure and mixed multipoles a typical way of determining the mixing ratio, δ, of a particular transition is to measure the K, L_1, L_2, L_3.... conversion-electron ratios which are strongly dependent on the the relative amounts of M1 and E2 amplitude present in the transition. Angular correlations between IC electrons and other radiations or with the beam of projectiles are another standard way of determining the multipolarity of the transition involved.

The emission of the IC electrons or gamma-rays is usually anisotropic. The ramifications of this for the measurements involving σ_{KI} are that: a) If one intends to use the γ-ray normalization method then a reliable value for the amount of anisotropy associated with the gamma-rays which are most intense is mandatory. b) Even if another normalization method is used but the experiments involve elements that are deformed enough to produce a significant amount of K x-rays from the IC channel (and therefore must also produce a measurable amount of CE γ-rays), the CE γ-rays will be anisotropic in their emission.

Corrections for this anisotropic emission of γ-rays can be made by choosing an appropriate angle for the photon detector of either 55° or 125°

[27]. If the constraints of the geometrical arrangement of the scattering chamber do not allow the positioning of the photon detector at one of the appropriate angles; in order to compensate for anisotropy, there are means of calculating the amount of counting losses due to the anisotropic γ-ray emission. These methods can become a bit tricky because they are based on the mixing ratios for mixed transitions, another complication introduced by the odd-A nuclides. Even for the pure multipoles, complications can arise when second-order effects become significant.

The internal-conversion process can be viewed as the exchange of a virtual photon of energy k between some excited nuclear state of transition energy k and of parity Π, and some bound atomic orbital electron. The Pauli Principle demands that the magnitude of k be larger than the binding energy, U_K, of the atomic electron involved in the process, in order that the electron is ejected into a continuum state, which represents the only available energy states of the system. The ejected electron has kinetic energy of $k-U_K$ and produces an inner-shell atomic vacancy which can be filled in either a radiative or non-radiative transition. Because both the nuclear and atomic states represent states with good parity, the ejected conversion electron also has definite parity assigned to it [28].

As long as no "penetration" effects are present (that is, the matrix elements for the radiative and non-radiative transitions are identical) the internal structure of the nucleus undergoing conversion will not effect the process. The nuclear structure or dynamic effects become important when the matrix elements are significantly different from each other; then the conversion process takes place inside the nuclear volume. These penetration effects can not be easily calculated and can become quite large when com-

pared with normal conversion [29]. In this thesis we are a bit fortunate in that all the CE nuclear states are "normally" converted which is as expected from an understanding of both processes. Because of this "normal" conversion we are luckily in position to use the various tabulated ICC's which are calculated on the basis of no anomalous conversion factors.

With no penetration effects present, the conversion takes place very close to, but not inside the nucleus. The calculation of internal-conversion coefficients is then best considered as a problem in atomic physics. The most accurate calculations involve these factors [30]: a) Relativistic Dirac-Hartree-Fock wave functions using screened potentials; b) The inclusion of the finite size of the nucleus which is especially important for s and p states because solutions using the Dirac equation for these states would lead to singularities if a point nucleus were used. c) A Fermi distribution of nuclear charge is assumed; and d) The inclusion of exchange effects as well as some direct interaction between hole states and continuum electrons.

The conversion coefficient from a particular orbital χ of a nuclear transition of energy k and multipolarity ΣL where Σ is either M or E, where M represents a magnetic transition, and E represents an electric transition is defined by:

$$\epsilon_{\chi'} = \left[\frac{\pi k(\frac{e^2}{hc})}{L(1+1)(2L+1)}\right] \Sigma \left| B_{\kappa\chi'}(\Sigma L) / R_{\kappa\chi'}(\Sigma L) \right|^2 \qquad (47)$$

where κ is the total angular momentum of the ejected electron which takes on the following values from the Dirac equation, $\kappa = l$ for $j = l - 1/2$ and $\kappa = l-1$ for $j = l + 1/2$ where the coefficients $B_{\kappa,\kappa'}$ (ΣL) have been tabulated [31] and $R_{\kappa,\chi'}$ are the radial integrals which are given by:

$$R_{\kappa,\chi'}(ML,k) = \int^{\infty} r^2 dr [g_\kappa(r) f_{\chi'}(r) + f_\kappa(r) g_{\chi'}(r)] \, h_l^{\,1}(kr) \qquad (48a)$$

$$R_{\kappa,\chi'}(EL) = \int^{\infty} r^2 dr \, [g_\kappa(r) f_{\chi'}(r) - f_\kappa g_{\chi'}(r)]$$

$$- [f_\kappa(r) f_{\chi'}(r) + g_\kappa(r) g_{\chi'}(r)] \frac{d}{dr} \, r \, h_l^{\,1}(kr) \qquad (48b)$$

$h_l^{\,1}(kr)$ are the spherical Hankel functions of the first kind, g_κ and f_κ represent respectively the large and small components of the Dirac equation for the continuum electrons which have kinetic energies of $k-U_k$, while g_χ and f_χ are the Dirac solutions for the bound states

Different values of κ do not effect the values of the coefficients (the overall magnitude of conversion) but do manifest themselves in terms of angular distributions. This is where the different phase factors of the different multipoles (although of the same parity) add coherently.

An interesting way to understand why the nuclear states that are typically highly converted behave in such a fashion, is to trace the behavior of the orbital electrons near the nuclear volumes. Intuitively, we expect the following: (experimental evidence is in accord with our intuition in this case) the closer the orbital electrons come to the nuclear volume and the longer lived the nuclear state, the higher the probability that the non-radiative process will occur.

Accordingly, a proper parameter to investigate is the radial time component of g_χ and f_χ, especially in regard to the electronic density near the nucleus. Their behavior is given by:

$$\begin{bmatrix} g_\chi \\ f_\chi \end{bmatrix} = A\, r^{\ell-1} \sum \begin{bmatrix} a_m \\ b_m \end{bmatrix} r^{-m} \tag{49}$$

The most important factor in eqn.(49) is A, which is the expansion of the atomic wave function near the nuclear volume. A has, in turn, a very strong dependence on the standard normalization term given by:

$$\int^{\infty} (g^2_\chi + f^2_\chi) r^2 dr = 1 \tag{50}$$

Recall that we are at this time only concerned with the radial dependence; the angular dependence was already dealt with by the coefficients $B_{\kappa,\kappa'}(\Sigma L)$. The electron density, $\rho(r)$, is defined by:

$$\rho(r) = (4\pi)^{-1}(g^2_\chi + f^2_\chi) \tag{51}$$

which has the following relationship to A given by:

$$A = \lim 4\pi\rho(r) r^{-2\,\ell-1} \text{ as } r \to 0 \tag{52}$$

with $\chi = 2(l-j)(j+1/2)$, for $s_{1/2}$ and $p_{1/2}$ states the values of A reduce to:

$$A = 4\pi\rho(0) \tag{53}$$

egn.(53) evaluates K and L_1 electron densities at nuclear surface

These results are to be expected given the greater degree of penetration of atomic states with lower values of j. This ability to penetrate into regions of space close to the nucleus translates directly into a

higher probability of being converted. This is the reason why K-shell conversion will always dominate the other subshell contributions when K conversion is energetically feasible. This is the case for ML transitions which are more converted than the corresponding EL+1 transitions. However, for EL transitions L_2 and L_3 conversion will be larger than L_1 ($s_{1/2}$, κ = -1) sometimes by an order of magnitude or more. L_1 conversion is decreased in this Z region due to a partial cancellation of the radial integral. Low energy M1 transitions have large contributions from nuclear surface terms, and, in consequence, the odd numbered subshells ($s_{1/2}$ states) make a larger contribution for these transitions than for E2 types.

This is because EL transitions are less sensitive to the orbital electron density and are more sensitive to the angular parts of the one-electron Dirac equation. This is particularly important at energies near the conversion threshold. A glance at the conversion coefficients shows that as k increases, the differences between the values of L_1, L_2, and L_3 conversion become smaller.

The main reason that longer-lived nuclear states are so highly converted is that the low energy, high multipole states live longer, allowing participation in the decay process by atomic electrons with significant densities near the nuclear volume. High-Z elements, with low-lying rotational types of transitions have the added dimension of having their orbital electrons spend a larger amount of time at the nuclear volume than the lower-Z elements. Taken together, it is not surprising that the low-lying rotational states in the rare-earths are as highly converted as they are.

Chapter III . Experimental Procedure

In this section the experimental techniques and equipment will be discussed with a special emphasis on how the performance of the various experimental systems affects the quality and accuracy of the experimental results. These considerations are particularly crucial in this thesis because many of the systems with which data were obtained were specifically designed and built in our facility.

The experimental techniques were modeled after other more conventional systems from both literature descriptions and from personal communications with other workers who performed similar experiments [1,2]. When constraints imposed on the design and functioning of the experimental systems demanded modifications or innovation, it was necessary to adopt a "trial and error" approach.

The beams of charged-particles were produced from the Brooklyn College Dynamitron which was manufactured by Radiation Dynamics Incorporated. The operation of this type of accelerator has been described previously.[3,4] The experimental conditions for the running of the accelerator at Brooklyn College have also been described elsewhere [5].

A recent and invaluable addition to the Dynamitron Lab has been two IBM PC/XT's which, when coupled to four Ortec ADCAM 918 MCB's, allows the user to transform the PC's into an MCA (multi-channel analyzer) for spectral data acquisition. All data were collected on these PC's via the Ortec software which was very skillfully modified by Dong Yan of the Dynamitron

Lab so that both photon and charged-particle spectra collection was relatively simple and painless. Spectra were stored on floppy disks which enabled the data analysis to proceed accurately and rapidly. More discussion of the spectrum analysis programs and the computer code used to calculate σ_{CE} will be given in Chapter V.

A. Target Preparation

A major portion of the experimental work was devoted to the fabrication of suitable targets of both separated and natural isotopes of the elements already mentioned in the Introduction. Some targets were purchased from Micromatter Co. of East Sound, Wash., to supplement targets that were made at Brooklyn College and also to serve as possible backups in the case that the targets made at Brooklyn College were either not durable enough or unsatisfactory in some other way for reliable experiments.

The targets made at Brooklyn College consisted of the natural elements (as well as some separated isotopes) Pr, Nd-142, Sm, Sm-150, Sm-154, Tm and Ta. They were backed by thin C foils that were purchased from Arizona Carbon Foil Co. The C foils that were used, ranged in thickness from 15-20 $\mu g/cm^2$ and showed no traces of contamination by heavy elements.

There was no indication of any characteristic x-ray or γ-ray lines due to trace-element contamination. In addition, the particle spectra displayed no peaks from elements whose presence was not anticipated from a knowledge of how the targets were produced. Not only was the collection of particle spectra essential for target thickness determinations, estimates of

beam transport through the scattering chamber, and for normalization involving RBS, it was also very useful in the analysis of the purity of the targets with respect to elements which are too light to give x-rays which can be detected, such as O.

The rare-earth targets were prepared by reducing the oxides with a suitably active reducing agent such as Th or Zr metal powder. This was necessary because the oxides either had sublimation points which were too high to be reached in a typical evaporating high vacuum system or were too unstable and degraded before they could evaporate onto a selected substrate [6,7]. There are two other concerns which mediate against using the oxides directly.

The first is the general instability of the deposited oxides which react to form hydroxides after evaporation onto the substrate. The hydroxides and, to some extent the oxides, are somewhat brittle and tend to flake especially under exposure to the particle beam. The loss of target material during bombardment can have dramatic effects on the yield of photons. We have found that for the target thicknesses typical for our experiments, energy losses of protons (the only projectile used for actual cross-section measurements) are too small and too variable to be considered as a reliable measure of target thicknesses.

Another very important consideration, one that arises specifically when separated isotopes are used, is the cost of these isotopes. In this regard it is a prime consideration to maximize the efficiency of both the reduction and collection steps as well as the deposition procedure onto the C foils. While inefficiency is generally to be avoided, when one is attempting to fabricate usable targets from a very small quantity (ca.100 mg) of

isotopically-separated rare-earth oxide, inefficiency can become disastrous.

When the elemental metal, is evaporated onto a C foil, the chemical reactivity is such that if a good vacuum was used during the reduction and evaporation processes, the amount of oxide formation is usually minimal [8]. After evaporating the metal, proper storage of the targets is essential in order to minimize any further oxidation. This can be accomplished by storing the targets in a dessicator under a noble gas or in a vacuum dessicator. Even with a great amount of care in terms of rapid placement of the targets in a stable environment and employing vacuums on the order of 10^{-7} torr for the reductions and evaporations, small peaks in the RBS spectra due to the presence of O were observed. Its presence in the RBS spectra was obviously due to oxidation processes taking place either in the evaporating chamber or in the dessicators where the targets were stored.

The detailed overall procedure for preparing C-backed thin targets from their oxides follows. The reduction process is performed in a Ta tube 2" long and 1/8" in diameter. The tubes were purchased from Fansteel, Corp. of Chicago, Ill. The oxide and the reducing agent, either Th or Zr, are mixed thoroughly prior to being placed inside the tube, to insure uniformity during the reaction. The amounts of reactants chosen are typically 50-100 mg of each and a 20% stoichiometric excess of the reducing agent is used. The balanced equation for the process is given below.

equation for the process is given below.

$$2Ln_2O_3 + Th \rightarrow 4Ln\uparrow + 3ThO_2$$

The Ta tube, after being loaded with the reactants, is sealed at both ends and then placed inside the evaporator where it is positioned between

two electrodes. Current is passed through the electrodes and the Ta, ohmically heating the tube and its contents. As the reaction proceeds, the metal formed in the reaction evaporates through a 0.025" pinhole in the tube and is collected as a nodule on a water-cooled quartz disc. The amount of current necessary to reduce the oxide and vaporize a rare-earth metal is variable and ranges from 80-130 amps. This reflects the differences in the stability of the oxides and differences in the heats of vaporization of the rare earths themselves. The evaporator used was a Veeco 300.

The collected nodule is then placed in either a W or Mo crucible for evaporation onto the thin C foils. They are obtained adhering to glass microscope slides, where each slide contains enough foil for three targets. A portion of the foil approximately the same length as the Al target support (ca. 1" x 1"), is removed from the slide by cutting through the foil at the right length and then placing the slide into a beaker of deionized water. Deionized water is used to avoid contamination from trace elements in tap water. By dipping and slowly submerging the slide carefully into the water at an acute angle, the foil gradually separates from the slide as the release agent (usually NaCl) binding the C foil to the glass dissolves.

Due to the lightness of the foil (if one has been very careful during the procedure not to rupture the foil) the foil will float on the surface of the water. Next an Al target support held with a tweezer is brought alongside the floating foil which is made to adhere to the top of the target support. The support and the clinging C foil are lifted gently and slowly from the water making sure that the angle between the water and the target support is nearly 90°. This handling procedure limits the amount

of water lying above the stretched C foil, especially the amount on top of the open space in the target support through which the evaporated metal will be deposited.

If too much water is allowed to sit on top of this open portion of the target support the C foil will invariably rupture and the process must be repeated. Up to five target supports, now containing the stretched and dried C foils are mounted onto the side-flaps of a holder fashioned in the shape of a pentagon. The side-flaps are cut to the same dimensions as the target supports. These flaps have holes in them (with the same dimension as the holes in the target supports) to allow the deposition of the metal onto the C foils, as was pointed out previously. They are also positioned at 30° to insure the maximum collection efficiency of the evaporated metal.

On the flat surface of the holder is cut a 1/2" hole to allow for the positioning of a quartz-oscillator thickness monitor. The quartz oscillator is positioned at approximately the same height as the C foils so that the amount of metal deposited on the crystal can be considered to be approximately the same as the amount deposited on the C foils. The operation of the thickness monitor will be described now but it should be pointed out that the accuracy of the monitor used at Brooklyn College was found to be in the range of 50% or so when the target thicknesses were measured by RBS determinations using 2.0 MeV alpha particles [9,10].

The foils and the quartz oscillator are placed approximately 2.5" above the crucible which contains the rare earth nodule. Again the temperature (and therefore the current required) at which the nodule evaporates depends on the particular rare earth. The amount of current needed to eva-

porate the nodule ranges from 50-90 amps.

The change in the resonant frequency of a quartz crystal vibrating in its thickness shear mode is well documented [11,12]; it is given by:

$$\Delta m = \frac{1}{2} C_q \rho_q \left(\frac{1}{f_f} - \frac{1}{f_q}\right) \tag{1}$$

where Δm is the mass per unit area of the evaporated film, C_q is the velocity of the transverse acoustic shear wave traveling from face to face of the quartz crystal, ρ_q is the density of the quartz, f_q is the resonant frequency before deposition, and f_f is the resonant frequency after deposition.

The acoustic impedance of the quartz is given by:

$$Z_q = C_q \rho_q \tag{2}$$

substitution into eqn.(1)gives:

$$\Delta m = \frac{1}{2} Z_q \left(\frac{1}{f_f} - \frac{1}{f_q}\right) \tag{3}$$

When the appropriate numerical values are used we arrive at:

$$\Delta m = 4.417 \times 10^5 \tag{4}$$

here Δm is measured in $\mu g/cm^2$ and the frequencies are in Hertz,

As an estimate of the change in resonant frequency, f_f, eqn.(4) is quite adequate to use in terms of selecting the approximate frequency change in the external audio oscillator. The evaporation is complete when the change in desired frequency is obtained, the targets are then allowed

to cool to room temperature in the bell-jar of the evaporator. This is done to minimize the possibility of oxidation.

B. Scattering Chamber Design and Experimental Arrangement

1. Description of the Chamber

Many accelerator groups are faced with the problem of performing meaningful experiments with equipment that is limited in design application or simply outdated and not compatible with current technology. Budget restraints being what they are, experimenters are often forced to improvise either by modifying their existing equipment or by building and designing new equipment [13,14] This process of custom designing experimental setups usually involves two separate but complementary approaches. One involves building a part or parts from basic materials. This requires skill from both the machinists supporting the lab and the experimenter/technician who must supply accurate drawings. Usually such parts can be designed from literature descriptions or by contacting someone with prior experience in their production. The second involves using a standard commercial piece of equipment in a novel experimental fashion. Often this requires making modifications and additions. Fortunately, the Machine Shop supporting the Dynamitron Lab at Brooklyn College routinely does marvelous work and some very experienced people were very helpful in making valuable suggestions and contributions [15-18].

A six-way multicross (commercially available from Anacon Corp, Division of High Voltage Engineering) serves as the basis of the chamber. It is mounted via standard Dependex vacuum connections on a beam line of the Dynamitron which also contains a larger scattering chamber [19]. A hand operated gate valve is mounted between this larger chamber and the one used for the measurements described in this thesis; the valve has Conflat fittings so it was necessary to purchase the proper adapters from Anacon so that the valve could be installed in the beam line. The hand valve was invaluable for maintaining high vacuum throughout the beam line when it was necessary to open the chamber for either target changes or for making adjustments in the chamber during experimental runs. The experimental arrangement is shown in Figure 1.

The chamber is oriented so that the beam enters the chamber through one of the 4" ports. After passing through the target assembly the beam is collected in a Faraday cup mounted on a 4" Dependex stainless steel blankoff. The four 6" ports are utilized in the following manner: --- One has a 2" Lucite viewing window, 0.25" vacuum sealed with a 2" flat rubber gasket; the outer edge of the Lucite/gasket seal (on the outside of the chamber) was sealed with Torr Seal epoxy to improve the vacuum seal. --- The port opposite to this is a canister that houses a solid-state photon detector. --- The bottom support of the multicross is a standard 6" blankoff Dependex plate. The side of the plate in the chamber has six lines scribed in it at 45° angles to each other; in addition a 360° circular compass made out of plastic is fixed to the bottom of the plate with an Allen screw. The markings on the compass are aligned with the scribe lines of the plate so that 0° defines the beam axis, 90° defines the axis with res-

pect to the photon detector, 150° defines the angle with the surface barrier detector and 45° defines the angle the target makes with respect to the beam. A "flag" made of 4" x 1" x 1/8" Lucite was epoxied to the 45° marking of the compass, the target ladder could then be adjusted from outside of the chamber so that its angle would line up with the flag. The targets had to be initially placed in the chamber at 0 so that the air flow through them was minimal during the evacuation of the chamber with a mechanical roughing pump. Any angle larger than 0° would invariably rupture the fragile thin targets. --- The fourth 6" port supports a vertically mounted target holder. he inside of the chamber is shown in Fiqure 2.

The housing for the photon detector is a standard 4" x 6" Dependex reducer protruding into the multicross. This orientation of the reducer is the inverse of its normal operation. An O-ring groove was machined on the surface opposite to where the O-ring is on the standard 6" flange.

Next a 4" x 2" Dependex was welded (by Anacon Corp.) to the 6" x 4" reducer because the standard 4" coupling had an o.d. larger than the i.d. of the 6" port on the multicross which made it impossible to position the canister inside the multicross using the standard couplings. The front face of the canister is a 2" stainless steel blankoff with a 0.5" aperture to allow photons to enter the detector from the target.

The photons pass through an 8 μm thick Kapton foil which is mounted in the aperture. The Kapton is glued to a brass ring with epoxy cement. the brass ring has an O-ring groove opposite to the Kapton side, which provides the vacuum seal when atmospheric pressure forces it against a seat machined around the aperture. This type of arrangement for isolating a high vacuum (ca. 10^{-6} torr) from normal atmospheric pressure has been patterned

after the beam exit window in the external beam PIXE system at Brooklyn College [20]. Kapton has good thermal and mechanical properties, as well as being reasonably resistant to radiation. In addition, the transmission of low energy x-rays is not significantly effected by the Kapton. When higher energy x-rays or gamma rays are being measured, absorbers or filters can be placed in front of the detector window on the low vacuum side. This has proven to be a very convenient feature in the canister design so that different absorbers or filters can be placed in front of the detector without the annoyance and bother of having to break vacuum. The "cannister" which housed the HPGe detector, and the Kapton window is shown in Figure 3.

The distance from the target to the Kapton window is 1.5", an additional 0.55" of air space is left between the detector and the window inside the canister. The detector is held in a fixed position once it is placed inside the canister so that the solid angle is constant for all experiments.

The hyperpure Ge photon detector, HPGe, is held inside the canister in a fixed position by insertion into a Lucite sleeve which was made to accommodate the dimensions of the specific detector used in this study. The detector used was an UPGRAD intrinsic Germanium detector purchased from Princeton Gammatech of Princeton, N.J. The operation, performance and efficiency calibration of the detector will be discussed in some detail in Chapter IV.

The Lucite sleeve is a cylinder that has dimensions 3" x 4" and has a 2.5" dia. hole cut inside which allows for a "snug" fit with the barrel of the HPGe detector. This snug fit makes for a permanent placement of the detector in terms of the distance from the target or the source, therefore

the solid angle and the orientation of the detector's window are reproducible from one experimental set-up to another

In addition to this important functioning as an accurate holder for the HPGe detector, the Lucite sleeve serves two more important functions in regard to detector performance: a) The Lucite electrically insulates the HPGe detector from ground loops which can degrade detector resolution. b) The Lucite insulates the detector from mechanical vibrations which degrade the detector's pre-amp signal with a resultant loss in the resolution of the detector's output signal and hence the overall sensitivity of the recorded spectra. To further protect against either of the two effects described in a & b, a Teflon guard ring was placed in front of the detector in a recess at the front of the canister. This ring has dimensions 2" o.d., 0.25" i.d., and 0.25" thick. The use of this ring introduces an additional air space in front of the detector, the size of the ring is as large as the air space. However, this doubling of the air space between the detector's window and the target has a minimal effect on the attenuation of even the lowest energy photons measured in this study.

Filters or absorbers can be taped to the front of the detector. Because the air space was fixed in front of the detector, there was no change in the detector distance or in the solid angle, due to the dimensions of the absorber or of a filter. As was already pointed out, having the detector on the atmospheric side of the chamber makes it much easier to change absorbers without the huge inconvenience of opening the chamber to atmospheric pressure.

The chamber is coupled to the handvalve by standard Dependex flanges with a bellows placed in-between the fittings to give flexibility to the

assembly. This flexibility was extremely important in the aligning of chamber. The chamber sits on a Lucite platform 0.5" thick platform and is long enough (30") to support not only the chamber and the HPGe detector. The HPGe detector sits on a 0.25" thick Lucite board (dampening micro-phonics) which in turn rests on a standard "Labjack". Removing the detector from its Lucite sleeve was not particularly difficult and more importantly, not hazardous to the proper functioning of the detector if a modicum of care was exercised when handling it. The platform's width is 14", sufficiently wide not only for the comfortable seating of the platform, but it afforded the opportunity to anchor the platform (and hence the chamber) with four screws. The screws were attached to brass pegs bolted into slotted grooves which allowed for readjustment if the beam parameters (and therefore the beam alignment) should change, either by choice or by happenstance.

The targets are held in position on a target ladder. The ladder assembly is 5.25" long and was originally composed of Al. We switched to a ladder made of Lucite so that x-rays and gamma rays from Al could be avoided. This was a consideration if the chamber was ever to be used for PIXE or PIGE type analytical work. The ladder can hold up to five targets each of which is mounted on a support made of Al. These Al target supports are 0.906" square and have 0.5" dia. holes at their centers. This 0.5" diameter hole in the target support represents the total area the beam can impinge upon and still strike the evaporated metal.

The assembly is connected to a 0.375" diameter, 7" long stainless steel shaft. A hand-operated threaded stationary screw drive supported in a Teflon cylinder allows for placement of the ladder (and therefore of a

target) into the desired position. The shaft is held in place inside the Teflon by two Allen screws which tighten against two grooves cut into the shaft.

What is significant in this arrangement is that by loosening the Allen screws and pulling the shaft free of the Teflon block, the target ladder can be oriented at 0° with respect to the beam axis. As was previously mentioned, this operation is critical to maintaining the thin C backed targets during the initial pumping down stages before the experiment. Once the pressure in the chamber was brought down below approximately 100 millitorr the ladder could be rotated back to a 45° orientation and the shaft reconnected back to the Teflon block. The compass on the bottom plate and the Lucite "flag" were both crucial in the realignment of the targets back to 45°. The targets were in no danger of rupturing once the pressure was low enough so that the hand valve isolating the chamber from the turbo-pumps on the beam legs could be opened.

Two O-ring seals were grooved into two Al support plates forming vacuum seals between themselves, the shaft, and the 6" Dependex plate at the top of the chamber. These Al plates were attached by screws into the top blank-off plate. There is a post marked so that the distance between the marks on the post is the same as the distance between the targets on the ladder inside the chamber. An arm on the shaft can be aligned with the appropriate mark on the post to indicate when a target is properly aligned in the beam. The necessary sighting and alignment of the targets was done by viewing through the 2" Lucite port.

The solid-state surface barrier detector, (SSB), for charged-particle detection was purchased from Paul Downey and Co. of Trenton, N.J. The

relevant dimensions and associated parameters of the detector were as follows: --- axially mounted microdot connector --- active area 100 mm^2 with a depletion depth of 300 μm --- operationally biased at 100-110 V positive and had a revers leakage current of 150-200 nanoamps --- energy resolution was typically between 15-20 keV for 1-3 MeV protons and alphas --- the overall width of the detector was 31.6 mm.

The output signal of the SSB is taken through a BNC vacuum connector in the top 6" blankoff which contained the target assembly. The SSB is mounted in an Al block that has a hole cut in its center to allow placement of the SSB. An Allen screw runs through the top of the block and is used to fix the SSB in position. On the front face of the block, a graphite collimator is attached which covers the entire SSB except for a hole cut in the front face of the collimator. It is through this front face on the collimator that the back-scattered projectiles reach the active surface of the SSB.

Graphite like Lucite eliminates unwanted radiation produced from projectile impact inside the chamber. The geometrical constraints in the chamber are severe, not only from the point of view of the experimenter's comfort in setting up the conditons in the chamber; but just as importantly in terms of data taking. A major source of concern imposed by the tight geometry was high particle counting rates. To eliminate counting rates that would result in deadtimes of greater than 25% with the attendant problems of peak distortion and pileup, it was necessary to use graphite collimators that had rather small entrance holes for the backscattered projectiles. The sizes of the holes used in these measurements were 0.080" and 0.110". The larger size hole was used for the lighter-Z element targets, while the

smaller size hole was used for the measurements for Tm, Ta, and W. As an example of the high deadtime losses possible in the tight geometrical arrangement of the chamber, consider that for a thin Sm target, deadtimes of nearly 90% were observed for 700 nanoamps of 1.6 MeV alpha particles. This situation is a good example of where the L-gamma x-ray normalization developed in this study could be useful. The graphite collimators used for the SSB were 1.375" long and 0.975" wide.

The SSB is seated in its holder atop an Al stand. This stand is attached to the base of the chamber by an Allen screw which allows for the positioning of the SSB in a variety of backward angles. For the experiments described in this thesis, the SSB was positioned at 150°. This angle was the maximum obtainable in the rather close geometry of the chamber without having the beam possibly obstructed. The stand, the holder and the graphite collimator were designed so that the opening of the collimator was approximately the same distance from the bottom of the chamber as the beam. The stand contains a slot through which the Allen screw can slide 1.5 " in distance from the center of the chamber. This allows for some latitude in placing the SSB with respect to the target. A "spike" placed at the bottom of the the stand serves as a marker to align the SSB's angle with respect to the incoming beam. The tail of the spike is aligned with the aforementioned plastic compass in order to get a crude estimate of the backscatter angle.

The Faraday cup assembly used for charge collection was designed to fit on one of the 4" blank-off plates. It sits behind the target ladder approximately 0.5" form the targets attached to the front of the ladder. The cup consists primarily of an outer Al cylinder about 4.5" in length and

approximately 2.5" in diameter. This cylinder is mounted directly to the blank-off plate (the side that is in the chamber) by two Allen screws.

The cup itself consists of three coaxial cylinders, one bias cylinder (ring) and a charge-collection cylinder which are both mounted inside the larger Al cylinder. These two cylinders are each 1" long and 0.5" in diameter. The charge collection cup is supported by a 2" ceramic standoff attached to the blankoff by a screw that runs through the rear of the cup. The bias ring is attached by a pair of 2" ceramic standoffs which again act as insulators as they did for the charge collection cup. The total impedance of the cup is in the range of 10^{-9} ohms.

The bias ring is connected to the negative terminal of a standard 300 V battery. This -300 V applied to the bias ring is a sufficiently high potential to both insure that the secondary electrons from beam impact on the chamber and the target do not enter the cup, and that electrons ejected from the Ta charge collection cup are spiraled in a decaying trajectory so that they are "swept" back to the collection cup [21]. In this way, no negative charge enters the cup to cancel the positive beam current and no negative charge is lost to collection due to ionization of the Ta, which would result in a charge integration higher than the true values. In our experiences to date, we have seen that without a negative bias on the cup, the currents that were measured were about 30% smaller than with the -300 V being applied. This was obviously due to the penetration of secondary electrons produced by beam impact (in the chamber) into the Ta cup. The construction of the Faraday cup is shown in Figure 4. The details of the scattering chamber have been published elsewhere [22].

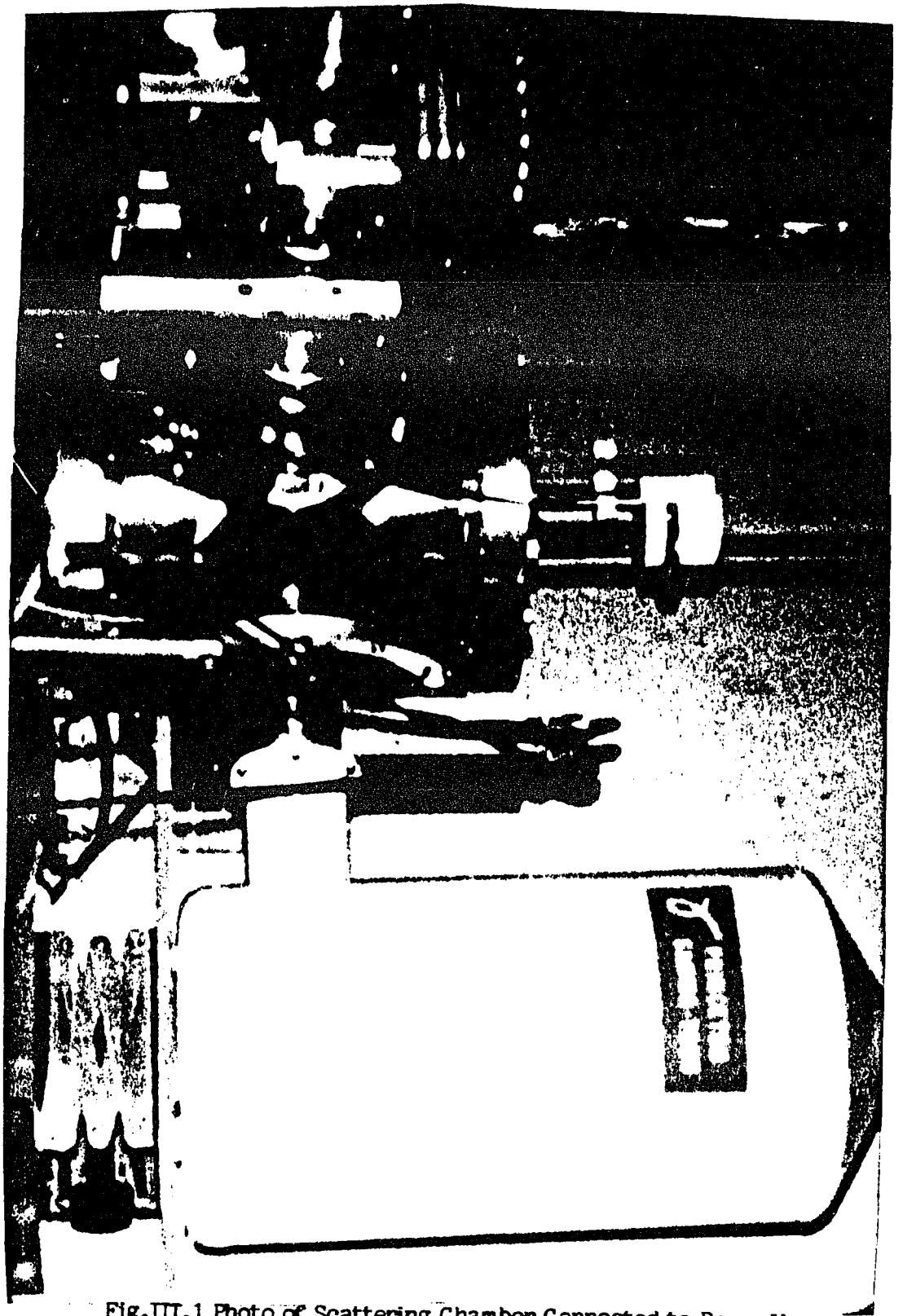

Fig.III.1 Photo of Scattering Chamber Connected to Beam-line

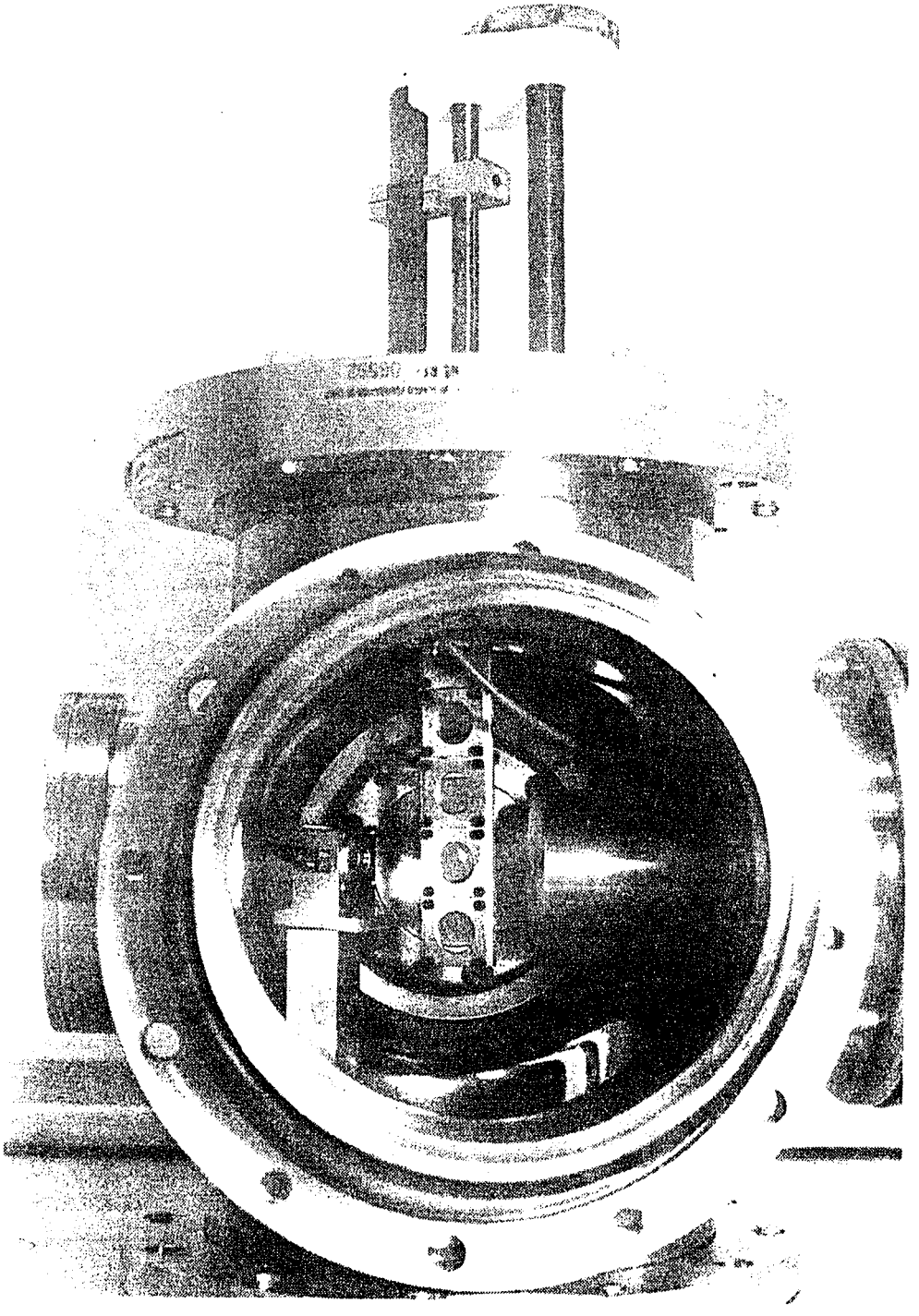

Fig. III.2 Photo of Interior of Scattering Chamber

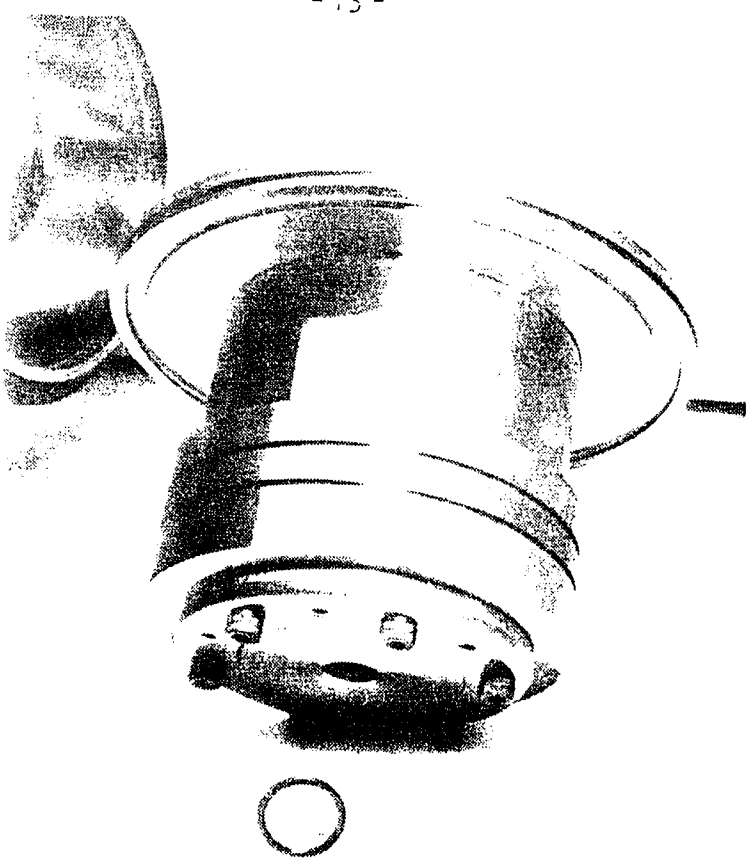

Fig. III.3 Photo of Detector Housing

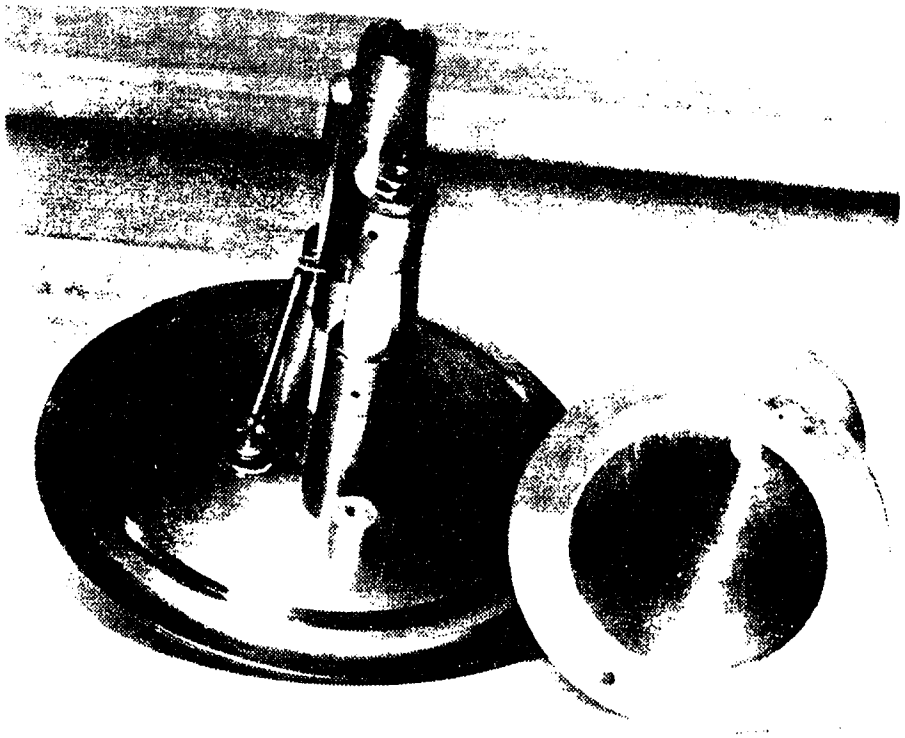

Fig.III.4 Photo of Faraday Cup Construction

Chapter IV Absolute Energy Efficiency Calibration of a Hyperpure Ge x-ray/Y-ray Detector

1.Introduction

A. Some Perspectives Concerning Detector Performance

High resolution HPGe and Si(Li) energy dispersive detectors have been extensively used over the past 20 years [1,2]. Their use has been extended to such diverse areas of research as: trace-element analysis, condensed-matter physics, nuclear and atomic physics [3-6]. In order to perform highly accurate cross section measurements, it was essential for us to know the absolute efficiency of a Princeton Gamma-Tech (PGT) HPGe detector of the UPGRAD series. purchased 14 years ago.

The methods of studying detector performance in the low energy x-ray/Y-ray region are nearly as varied as the areas of research to which these devices are applied. In order to carry out detector peformance studies it is quite often neccesary that the researcher be an expert in some area of "pure" physics. Detector studies can involve the use of facilities as complex as synchrotron light sources [7] and the involvment of computer codes which may contain large databases. These databases frequently have been accumulated over the years by the investigators themselves.

These databases may contain charged-particle or photon induced cross sections, intrinsic linewidths of characteristic x-rays or Y-rays, physical parameters pertaining to fundamental photon-detector interactions such as

Compton scattering amplitudes, transport phenomena of either photons or charge carriers in detector material and absolute decay rates, energies and branching ratios of the most commonly used radioisotopes for calibration purposes.

Many codes are written not only with extensive databases but also with distinctive features that allow the handling of not only the characteristic lines but can also contain sophisticated background modeling, escape peak fittings and area determinations [8] as well as the ability to fit and identify unusual spectral features. One of the most important of these unusual features especially for K x-rays emitted from elements with $Z < 30$, are the radiative Auger (RA) transitions [9]. In the case of background modeling, Compton scattering probabilities and low energy tailing of peaks are two areas which have received sufficient attention to be included in computer codes for data analysis [10].

It was important to enter this complicated and somewhat mysterious area of detector performance not only because accuracy in efficiency calibrations was important, but also to learn more about detector response in terms of overall background intensity and shape, specific backgound and interference effects that are present in spectra and variations in peak shapes as a funtion of photon energy and counting rates. Variations of all of the above can become large in particular energy regions, even over very narrow energy intervals.

To further complicate matters, the manufacturer's design nuances and techniques of production add a new set of complexities. In a not totally unrelated way the manufacturers of radioactive calibration sources introduce their own set of manufacturing nuances. These nuances may involve the

choice of materials in the sealed source, the physical form of the source and the chemical and radiochemical purity of the source.

Detector performance can be evaluated from a number of different perspectives and approaches. These approaches can roughly be divided into two schools. In one approach, researchers make measurement of certain characteristics of a specific detector. These measurements usually are an attempt to understand how the components of a particular detector design are functioning. The other approach assumes the essential properties of detectors to be invariant with respect to design strategies (this can be a very risky assumption) and therefore roughly uniform. The latter school concentrates more on the quality of the obtained spectra than on the performance of any indivdual detector component or design.

Some particularly extensive studies can combine both philosophies in a very comprehensive way. These combined studies usually involve a cooperative effort by a diverse group of scientists. A pooling of their respective talents allows the bridging of any gaps between the two philosophies. Needless to say, the first approach usually takes in scientists that are more involved in detector fabrication and development. The second attitude is common with scientists more concerned with the detector's use in some other area of research. Only at some large research facility such as Lawrence Berkeley Lab [11] can investigations like this occur.

Our approach to detector performance is fundamentally the second one, since all our data are in the form of recorded spectra. Therefore all conclusions are drawn based on this kind of information augmented by the specific design of our detector determined to the best of our abilitiies through experiments, the literature or personal communications. Although

we have never taken apart our HPGe detector we will attempt at least to offer some explanations of why the efficiency results we have obtained are what they are.

2. Methods of Evaluating Detector Performance

A.Methods Concerned with Indivdual Component or Overall Design Physical Measurements

The experimental means of evaluating detector performance can be divided into four distinct categories. The first is practically the sole domain of people who design detectors or are involved in improving detector performance or producing detectors for specialized purposes [12]. In the majority of situations, this type of researcher knows exactly what is inside the detector and therefore is primarily monitoring the response of the detector within some particular set of parameters, such as an energy window or a counting rate of interest.

Photon sources are used primarily as signal generators by this group of workers. The response of the detector to the photon source can then be correlated with the performance and behavior of the detector's components. Usually measurements of physical characteristics such as reverse leakage currents, depletion voltages, I-V characteristics, capacitance and the thicknesses of certain layers of detector components are made in conjunction with the recorded photon spectra.

Researchers not involved with detector design or manufacture have a different experimental concern. First, they can not afford to have a detector perform anamolously or erratically during an experiment. Secondly, they must rely heavily on the manufacturer to supply accurate performance and design specifications of the interior regions of the detector.

Although performance specifications can be checked easily enough in the lab, design specifications are not easily determined. However, photon sources can be used as "probes" as well as signal generators. We use the term probe to signify the ability to "see" what is behind the housing of the detector and in some instances even to determine the quantities. This is made possible by taking advantage of the ability of the calibration source to act as a fluorescer of some of the elements used in the detector construction.

Although the characteristic x-rays produced in this manner are quite small in comparison to the main calibration lines, they can be identified either by close inspection of the recorded spectra or by a computer code used to identify characteristic x-ray lines. Typically, this method turns up the type of metal used for the ohmic (normally a p^+ contact) contact on the front face of the detector. This metal is usually Au, Pd, Al or In, sometimes it can be made of BN, in which case no characteristic x-rays will be seen.

Photon calibration sources can be collimated to produce narrow beams. If they are then mounted on a two-axis vernier then scans of the detector crystal can be made. Peripheral imperfections can be uncovered by checking the peak shapes of lines in the spectra. These imperfections are centers of poor charge collection which produce asymmetric peaks with long low energy

tails. The correct solid angle can also be measured with this technique by determining the actual dimensions of the active area of the crystal and by the determination of the distance between the front face of the crystal and the Be entrance window. This second measurement is made by varying the distance between the Be window and the source and observing the change in the ratios between high and low energy peaks emitted by the same source. This is an alternative way of calculating the solid angle instead of having to rely on the values supplied by the manufacturer which may sometimes be in error.

This dual use of photon sources was first introduced by Hansen, et al. [13]. They proposed that a x-ray/Y-ray detector's performance could be divided into distinct energy regions. The efficiency in each region is determined by factors which differ from each considerably. The low energy region, usually taken for photon energies, E_γ, less than 20 keV, has its effiency, ε, determined primarily by the amount of attenuation that occurs before the photon reaches the active volume of the detector.

This attenuation is due to the presence of absorbers in front of the detector's crystal such as: any entrance windows used to form vacuum seals on the counting chamber, the Be window used to make a thin entrance window in the cryostat for photons, the ohmic contact on the face of the detector, a layer of solid ice that forms over the front face of the detector especially if the detector is always kept at liquid Nitrogen temperatures [14] and a dead layer of either SiO_2 or GeO_2 which is unavoidably formed on the front face of the detector during the processing of the crystal. Most manufacturer's keep this dead layer thickness between 0.2 - 0.3 μm. The high energy values of ε are determined mainly by the thickness of the detector

crystal and the values of the photoeffect cross section, σ_{ph}, for the E_γ's under consideration in this work.

The magnitude of ε for a specific detector, either Si or Ge, at a particular E_γ is determined by μ_{ab}, the mass attenuation coefficient of the detector material. The values of μ_{ab} for E_γ's considered here are almost exclusively determined by the σ_{ph} values. These approximations can be extremely useful and instructive when thinking about a model for x-ray/γ-ray detector performance and response. In a very real sense this parameterization method allows one to "look" inside a given detector and then to evaluate the performance of that detector on the basis of the nature and the quantities of the internal components.

The relative efficiency, ε_r, can then be expressed by (1):

$$\varepsilon_r = \varepsilon\, f_a\, f_{ohm}\, f_{esc}\, f_{dl}\, f_{col}\, f_{ch}\, f_{ice} \qquad (1)$$

where ε is the intrinsic efficiency of the detector material, f_a refers to the amount of attenuation due to absorbers not directly in contact with the detector crystal, f_{ohm} is the factor relating to the attenuation due to the ohmic contact, f_{esc} is the probability for producing escape peaks at a particular E_γ, f_{dl} is the factor referring to the attenuation due to the dead layer, f_{col} refers to the collimation effects if any collimator was used, f_{ch} relates to any poor charge collection effects for a given E_γ and f_{ice} refes to the attenuation due to any ice layer.

The escape-peak production, poor charge collection and dead-layer thickness are somewhat interdependent and a clear delineation as the to the role of each factor at some E_γ is not always possible, particularly

when E_γ is very close to the binding energy E_b of an electronic shell or subshell, of Ge or Si. The parameterization method is an attempt at isolating and therefore understanding how the interactions between photons and detector components are influencing the absolute efficiency, ε_{abs}, for a given E_γ.

The low and high energy regions can be defined by (2), with the first term having the strongest influence on the smaller E_γ's and the second term having greatest impact on larger E_γ's.

$$\varepsilon_{abs} = \Omega \exp [-\Sigma \mu_i(\rho t)_i][1 - \exp (\mu_d)(\rho t)_d] \quad (2)$$

here Ω is the solid angle subtended by the detector usually given in millisteradians, msr, ρ_i and ρ_d are the respective densities of the absorbers and of the crystal, t is the areal thickness of the absorbers and the crystal given in g/cm^2, and μ_i and μ_d are the mass attenuation coefficients of the absorbers and the detector material for a given E_γ.

The first term of eqn.(2) is the one which determines ε_r for small values of E_γ, that is generally taken as $E_\gamma < 20$ keV. The reason for this is that for small E_γ's the attenuation factors are so large that the intensity of these low energy photons is greatly reduced before they reach the active volume of the detector. The values of μ_{ab} for small E_γ's are very high, therefore there is an almost 100% chance that these photons will be absorbed in the detector material. We should still recall however that other factors listed in eqn.(1) such as escape-peak formation and poor charge collection can still influence strongly the values of ε_{abs}.

When E_γ reaches ≈ 20 keV the attenuation factors practically disappear and ε for small E_γ's is nearly unity. The value of ε_{abs} is then determined by the second term of eqn.(2), the high energy term. For larger E_γ's the values of μ_{ab} decrease primarily due to the decrease in the magnitude of σ_{ph}. This translates into a decreasing probabilty that the photon will be absorbed as E_γ becomes greater. The probability that a higher energy photon will be detected is then very strongly dependent on its overall interaction path, i.e. the crystal thickness and on the magnitude of σ_{ph} of the crystal material. Incidentally, due to Z^5 dependency of σ_{ph}, a Ge detector of the same dimensions will be much more efficient than a Si(Li) detector for larger E_γ's.

3. Calibration Methods Based on Models of Parameterization

A. Cipolla's 5-Parameter Non-Linear Least-Squares Method

This last calibration method while fundamentally very sound does have the drawback that it can be a very time-consuming operation. Not only do the measurements themselves require a good of effort and preparation, not to mention some degree of skill, it also requires special instruments to perform the scans. These instruments may either be costly to buy or to be made specially for this use. These considerations have lead to the development of a calibration method first proposed by Cipolla [14]. Cipolla suggested that a model of Hansen's method could be made that was faithful to all of the important aspects. This model assumes that eqn.(2) is an actual physical representation of the processes that determine a detector's effiency. A 5-parameter non-linear least-squares fit of experimentally obtained

data was proposed as a way of extracting much of the same information dealing with the high and low energy behavior of a detector. This modeling precludes having to make the scanning measurements oneself.

While Hansen's method has been originally tried on both Si(Li) and Ge detector's, Cipolla's method was originally proposed only for Si(Li) detectors. We are aware of only one attempt to use the 5-parameter fit for HPGe calibrations [15]. The details of that calibration were not included in the publication however.

The method of Cipolla does not give the values of the crystal dimensions etc. but rather recasts eqn.(2) into (3):

$$\varepsilon_{abs} = \Omega\,[\alpha/E^{\beta}][1 - \exp\gamma E^{\delta}] \quad (3)$$

The values of α, β, γ and δ as well as Ω are determined by the best fit obtained for the experimental data, this generally translates as the lowest value of χ^2 for the fit. In keeping with the spirit of Hansen's method, the first part of (3) is the low energy dependency while the second term determines the high energy dependency. Therefore α and β are to be considered the low energy coefficients since their values are responsible for ε_{abs} for small E_γ's, likewise γ and δ are the high energy coefficients. The solid angle is still defined as Ω.

Implicit in this representation for ε, is that the equation does not hold when $E\gamma$ is close to an absorption edge for any of the detector components in significant abundance. On a practical level this refers mainly to either Si or Ge. At an absorption edge, σ_{ph} does not vary smoothly with increasing E_γ and β can be thought as representing the energy dependency of

σ_{ph} so that the validity of eqn.(3) is severely jeopardized. For Ge detectors this represents an important energy region beginning at 11.10 keV and extending up to approximately 20 keV. Exactly where this region ends is not only difficult to establish experimentally but it also marks another border, that is the one between the low and high energy regions. In terms of a behavior that can be modeled, we are aware of no successful attempt in the literature to fit experimental data for this energy region of a Ge detector. Therefore it remains to be seen how appropriate eqn. (3) is in dealing with three different energy efficiency regions and not just with two as for Si(Li) detectors.

Cipolla [16] subsequently recognised the importance of accounting for the effects of the Si K absorption edge on the accuracy of the 5 parameter fit. This consideration became very important in his attempt to extend this calibration method down in the energy range below the Si K edge at 1.814 keV. He pointed out the inadequacy of relying on one fit for E_γ's which were both above and below the Si K edge energy, and for fits which incorporate absorption edges in general.

For low energy x-rays $E_\gamma < 3.0$ KeV, not only are attenuation factors by absorbers, and in the case of Si(Li) detectors the escape of Si K x-rays from the detector's active volume (for E_γ's > 1.814 keV) important contributer's to the low ε values for these E_γ's, but there is a large degradation in energy resolution and therefore the quality of the peakshapes obtained [17]. This degradation in energy resolution takes the form of long tails extending on down from the low energy side of the peak. These tails which are much longer than any tails that may be seen at higher E_γ's, are not remedied by altering the detector bias or the amplifier shaping time as

This adaptation by Cipolla to accomodate the absorbtion edge effects into his calibration modeling was done by performing two separate 5 parameter fits. One fit contains only the low energy points below the absorbtion edge(s) of importance. For Ge detectors, we need to consider only the K-shell edge at 11.10 keV. Ge L-shell edge efffects although very important in effecting peakshapes particularly for E_γ's < 2.3 keV.

Another 5 parameter fit is made to all of the other points which lie above the energy of the K edge of the detector material. From a practical point of view it usually best to do this fit first. This is because the high energy parameters γ and δ as well as Ω have the identical values for both fits. The values of the low energy parameters α and β will change however. Another 5 parameter fit is then made to find the best values of α and β for E_γ's < E_K, the K-shell binding energy of the detector material.

The values of γ and δ remaining fixed is again very much in line with the proper functioning of eqn. (1). The assumption there was that the energy regions can be viewed as essentially independent of each other in terms of the factors which influence the values of ε_{abs}. This is true particularly for the high energy region, hence γ and δ are constant throughout the entire range of E_γ. This is another way of stating that for E_γ's sufficiently high in energy all the factors relating to absorbtion edge effects are not important. The fact that there is a rather dramatic shift in the values of both α and β indicate how sensitive ε_{abs} is to many of the factors listed in eqn. (1) such as escape peak formation, charge collection effects etc.

Based on the validity of making two separate 5 parameter fits for Si(Li) detectors, we have similarly done two separate fits which included first only E_γ's > 27 keV and then a fit for E_γ's < 11.10 keV. No fit was attempted for 11.10 < E_γ < 22.0 keV, the effects of the Ge K edge elimi-

nate the possiblity of obtaining a smooth fit in this energy region. The values of ε_{abs} in this energy region were the ones obtained from experimental results without any considerations of modeling detector response.

B. Linear Fit Approach to Cipolla's Model of Detector Efficiency

Montenegro, et al. [18], proposed a variation of Cipolla's method based on how the fitting of the experimentally obtained data should be done. Montenegro also suggested an alternative to using calibrated sealed sources for the low energy data points. Recognising that purchased radioactive sources which emit low-energy x-rays and γ-rays ($E_\gamma < 15.0$ keV) are sometimes unreliable due to uncertainities in the thicknesses of both the source and the cover surrounding the source, he suggested an in-beam method of generating K_α and K_β x-rays.

The K x-rays of elements with $Z \geq 19$ could be produced by 1.0 - 2.0 MeV proton bomdardment of targets made by evaporating solutions (containing the elements of interest) deposited on some polymer backing. The elemental targets could be produced by the experimenters themselves thereby removing some of the uncertainties involved with using purchased sources. The procedure of producing the standards is practically identical to the procedure used in our lab for PIXE analysis.

The K_α/K_β ratios, rather than the absolute yields of the indivdual K x-rays, were to be used to obtain the values of the low energy coefficients α and β. The experimentally obtained K x-ray ratios of a given element are "normalized" to the theoretical values for the ratios of Schofield [19]. It was assumed tacitly that no other perturbation to the experimentally obtained ratios would interfere and that the changes in the measured ratios

would be due entirely to the element's higher energy K_β x-ray being detected with a higher efficiency than the element's K_α x-rays. This is consistent with the parameterization approach, ε is larger for the K_β x-rays because they are less attenuated before reaching the detector crystal.

It is known that K_α/K_β ratios can be affected by the mechanism of K-shell vacancy production [20], however it is generally assumed that at least in terms of multiple inner-shell vacancy production K x-ray ratios produced by low energy protons are quite close to Schofield's values [21]. This is not true for heavier, more energetic projectiles impacting on relatively light targets or for inner-shell vacancies produced by some radioactive decay processes.

The values of the high-energy coefficients γ and δ are obtained independently of the α, β values by using the standard calibration sources such as: Am-241, Ba-133, Co-57 etc. The higher E_γ lines, i.e. those above 20 keV, are not appreciably affected by attenuation. Instead of using one fit to find the values of the 5 parameters, one straight line fit using the K x-ray ratios is used for α and β while another straight line fit is used to find the values of γ and δ using data obtained form radioactive sources. The solid angle, Ω, in this method is not obtained from a fit. The value of Ω must then be found either by relying on the manufacturer's values or determined experimentally in a manner similar to that of Hansen [13].

The main advantage of these straight-line fittings, besides removing the uncertainities and the expense of using calibration sources, was that the degree of correlation between two related coefficients (either both low or both high energy) should be more physically significant than one 5-parameter fit of all the coefficients. All of the assumptions built into

Cipolla's methods are left intact concerning the restraints on the validity of the overall approach. An extremely important consideration, especially for Ge detectors (we must still bear in mind that Montenegro's method was proposed for a Si(Li) detector), is that the two energy regions are joined together continously (slopes of nearly zero at the point of intersection of the two energy regions) with no abrupt or long range changes in ε_{abs} as E_γ increases.

The fit to the low energy data is given by:

$$\lambda = \ln (\varepsilon_{K\beta}/\varepsilon_{K\alpha})/\ln (E_{K\beta}/E_{K\alpha}) \qquad (4)$$

where $\varepsilon_{K\alpha}$ and $\varepsilon_{K\beta}$ are the efficiencies for the K_α and K_β x-rays and $E_{K\alpha}$ and $E_{K\beta}$ are the weighted energies for the unresolved K x-ray multiplets

The values of α and β can then be found using:

$$\alpha\beta/(E^\beta) = \ln (\varepsilon K_\beta/\varepsilon K_\alpha)/\ln (E_{K\beta}/E_{K\alpha}) \qquad (5a)$$

where $E = (E_{K\alpha} + E_{K\beta})$

substitutung λ into (5a) and taking logs yields (5b)

$$\ln \lambda = \ln \alpha\beta - \beta \ln E \qquad (5b)$$

a linear least-squares fit of (5b) gives the values of α and β.

Unfortunately, besides the well known discontinunity in ε_{abs} for Ge detectors, there is still another complication in applying the straight line fits, this complication is independent of whether the detector used is a Si(Li) or a HPGe. Additional factors that contribute to measured K x-ray

peakshapes and intensities are not related to the detector material but to fundamental inner-shell atomic processes and are not related to the mechanism of inner-shell vacancy production. These processes need to be considered when K x-ray peakshapes and relative intensities are to be accurately measured relative to theoretical predictions, either for purposes of testing theoretical predictions of radiative branching ratios or in this case an applied purpose.

The presence of RA transitions embedded in the recorded K x-ray peaks of elements with $Z < 30$ can systematically produce experimentally determined values of K_α/K_β x-ray ratios which are actually higher than those predicted by theory. The best explanation for this effect regarding the recording of higher than theoretical K-ray ratios due to the presence of photons from RA transitions in characteristic K x-ray spectra of light elements has been given by Campbell [22].

Campbell has carefully studied the importance of identifying and determining the peakshapes of RA structures for both applied studies such as accurate PIXE determinations [23] and in atomic physics research involving the measurement of x-ray decay rates, branching ratios etc. [24]. Using a very highly developed computer code, HYPERMET, for peak and background fitting, counting for long time periods and being extermely thorough in source preparation and handling he has been able to measure the probabilities for KLL, KLM and KMM RA transitions. Campbell has shown that Schofield's predictions for both the RA transition propbabilities and K x-ray ratios are generally correct and reliable.

For our immediate purposes, however, what is of prime importance is just how RA photons alter K_α/K_β ratios. Again we turn to Campbell whose

explanation is that if one uses a computer code to analyse the x-ray spectra that assumes a Gaussian peakshape for the K x-ray line (ordinarily a good assumption) the non-Gaussian spectral features will be removed from the peak, and along with them, some of the x-ray intensity that is "true" in the sense of it being due to allowed x-ray radiative transitions.

The subsequent losses of events from the peak areas due to the Gaussian fitting routines employed will weigh more heavily on the K_β peaks than on the K_α peaks. Briefly, the reason for this is that the KMM RA transitions are more intense by factors of nearly ten than KLL RA transitions of the same element. The KMM RA transitions have energies close enough to the K_β x-ray energies that they are "embedded" in the K_β peaks. Usually only the KLM RA energies will overlap with the K_α energies.

Therefore, after K x-ray lines of elements with $Z < 30$ are fitted to Gaussian lineshapes, relatively more of the K_β peak intensity has been lost than with the corresponding K_α line. What one finds typically, is then the differences in ε for the two x-ray lines has been "washed out" in the data analysis. Assuming good detector resolution for K x-rays in the range ($3.0 < E_\gamma < 11.0$ keV) and good signal-to-noise ratios, one can find, as we have, K_α/K_β ratios which can be 5% higher than the theoretical values. These types of results were obtained for measurements done in-beam, and with a calibration source, Co-57. These results were obtained by using the x-ray analysis code RACE [25] which does indeed fit characteristic peaks to Gaussian peakshapes.

The high-energy coefficients, γ and δ are obtained from a linear 2-parameter least-squares fit. In this energy region we are essentially free from most of the complexities and subtleties that operated in the low

energy region. Therefore all the datapoints in this region can be obtained from radioactive calibration sources. The high-energy region is approximately 20 keV for Si(Li) detectors; if there was no drop in ε due to the Ge K-edge effects, we would expect this to be significantly lower in energy for a Ge detector of equal size.

To arrive at the values of γ and δ we return to eqn. (3) and assuming a E_γ such that α/E^β is unity we can rewrite eqn. (3) so that we have:

$$\varepsilon = y = 1 - \exp(\gamma/E^\delta) \quad (6a)$$

unity here represents the value α/E^β and y is expressed by:

$$y = \varepsilon_{abs} \exp \alpha/E^\beta \quad (6b)$$

ε_{abs} is the experimentally measured efficiency using an E_γ from one of the sources chosen

The high energy region can be taken independently of the low energy region under the condition that exp α/E^β is unity. In that case eqn. (6a,b) can represented by:

$$\ln [\ln (1-y)^{-1}] = \ln \gamma - \delta \ln E \quad (7)$$

The appropriate values of γ and δ are then determined from a linear least-squares fit of the data just as the values of α and β were obtained.

While Cipolla introduced a variation in his method to account for the effects of the Si K edge, we can see no variation that would allow using these 2 linear fits to incorporate the dramatic effects in ε brought about

by the Ge K edge. This can be seen as the limitation of being able to produce one set of values for α and β and having to assume that the values of these coefficients are practically independent from the high energy ones. On the high-energy side, however, we would be safe to assume that as was the case in the 5-parameter fit, even when there was the provision for the effects of the Si K-edge, the values of γ and δ are not altered by any edge effects.

We should bear in mind that although, from a modeling perspective, the Ge K-edge has not been dealt successfully as yet, it has not been ignored in terms of experimental work [26,27]. It has not been ignored in this work either and will be discussed in terms of our experimental results later in this Chapter.

4. Calibration Methods Based on Absolute Measurements

A fourth philosophy concerning efficiency calibrations exist and one which in all candor probably requires being very knowledgable in either one or more of the specific areas of those outlined in the Introduction. In addition, this last approach is sometimes diverse enough to incorporate many of the features that pertained to the other approaches and even to make improvements on them. These methods have the most intregrated approach in making thorough and accurate measurements. This approach is perhaps best exemplified by the work of Campbell [28] and Cohen [29] and is the approach that benefits the most by the application of one or more of the investigator's indivdual talents.

The data obtained from these type of measurements can be analysed for the goodness of fit and the results then interpreted in terms of either the physical parameters that determine ε or in terms of some design feature or flaw of particular detectors. This method seems to thrive in environments where some other research area is being actively pursued that demands accurate, reliable information of detector performance and response.

A. Experimental Methods Used For Calibration

i). Techniques

We applied three of the calibration methods discussed above: Cipolla's 5-parameter fits both above and below the Ge K-edge (11.10 keV), Montenegro's method using two separate linear fits and an absolute method of Maenhut [30]. This last method involves using elemental foils bombarded in-beam as did the method of Montenegro, however, instead of using ratios of K x-rays, the method of Maenhut depends a great deal on the accuracy of the K x-ray production cross sections of those elements. Fortunately, for protons in the energy range of 1-2 MeV and for the low Z elements for which this latter method is suitable, ECPSSR cross sections are accurate to 3-5% [31]. The values of related quantities needed to convert σ_{KI}'s to σ_{Kx} such as: ω_K, $\Gamma_{K\alpha}$ etc. are generally known within 2-6% [32]. This method also depends on the accuracy of target thicknesses (typically in $\mu g/cm^2$) if charge normalization is to be used, or the recording of a distinct RBS signal from a charged-particle detector if normalization to the Rutherford cross section is used.

a. In-Beam Methods

These considerations of accuracy regarding target thickness and uniformity (very important for normalization purposes) led us to forego the production of targets ourselves for these absolute measurements. Targets of

elemental standards were purchased from MicroMatter Corp. of East Sound, Wash. The targets were mounted by MicroMatter on Al target supports supplied by us that were designed to fit our target ladder in the experimental chamber set-up described in Chapter III. The backing for these elemental foils was 6.3 μm Mylar.

The elemental foils and their thicknesses used in this absolute low energy calibration method were: KCl 39 μg/cm², V 46 μg/cm², $CrBr_3$ 56μg/cm², Fe 30 μg/cm², Ni 48 μg/cm², ZnTe 42 μg/cm², Ga 36μg/cm², Ge 41 μg/cm², Se 51μg/cm² and YF_3 49 μg/cm². The thicknesses of these foils were checked by RBS measurements in our scattering chamber and found to be in agreement with the supplier's values within ± 10%. The E_γ's covered by these elements are from 2.62 keV - 30,85 keV, that is from Cl Kα to Te Kβ x-rays. A RBS spectrum of ZnTe taken with 2.0 MeV protons is shown in Fig.IV.1. The Te and Zn peaks at the higher energy side are resolved, while the Mylar backing peaks of O,N and C are seen at low energy.

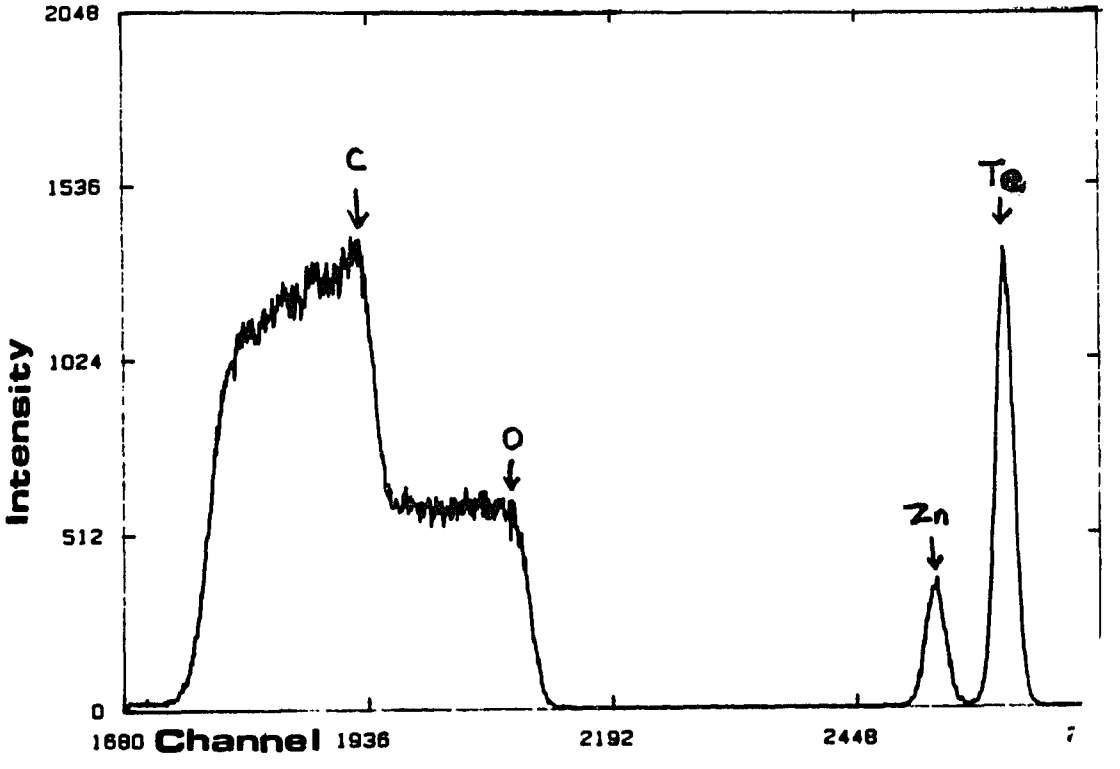

Fig.IV.1 RBS spectrum of ZnTe bombarded with 2.0 MeV Protons

The foils were placed on the target ladder and then oriented at 45 degrees with respect to the beam axis. Protons of 2.0 MeV were used to produce the characteristic x-rays. This energy was a good compromise between the accepted accuracy of ECPSSR cross sections and the overall counting rate of x-rays. We kept the counting rate below 1500 cps in all cases to minimize pileup and peak distortion problems associated with high counting rates.

A Princeton Gamma-Tech, HPGe detector of the UPGRAD series was the detector calibrated. The detector was operationally biased at -1000 V, the suggested value of the maunfacturer. The detector was equipped with a pulsed-optical feedback charge-sensitive preamp, and had an active area of 25 mm^2 as claimed by the manufacturer. A Princeton Gamma-Tech 340 amplifier with a shaping time of 10 μsec was used. An ORTEC 571 amplifier was used for particle counting, its shaping time was typically set at 0.5 μsec. The particle counting was done in the arrangement outlined in Chapter III with the particle detector set at a backward angle of 150 degrees.

The x-ray spectra were analysed using a version of the computer code RACE developed at Brooklyn College [32]. Deadtime corrections were automatically done by RACE in the final output. The detector resolution measured during charged-particle bombardment was 200 eV for Fe K_α x-rays, (6.41 keV) and 250 eV at (11.92 keV), Br K_α x-rays. The resolution of the detector at higher energies using radioactive sources was 625 eV at 86.5 keV and 790 eV at 123.14 keV. The distance from the target position in the chamber to the face of the detector's outer housing was 5.1 cm. There was no collimator placed over the Be entrance window of the detector.

Particle spectra were collected as well as photon spectra both to check the target thicknesses and for normalization purposes. Total integrated charge was also recorded for charge normalization purposes. The ORTEC ADCAM data acquisition system was used in collecting all of the calibration data. The K x-ray spectrum of the V foil is shown in Fig.IV.2. Beam currents of 2 - 35 namps. were used with total integrated charges of 8 - 25 μcoul. The lower currents were neccesary for the lighter elements like K and V_j to keep deadtimes below 10%.

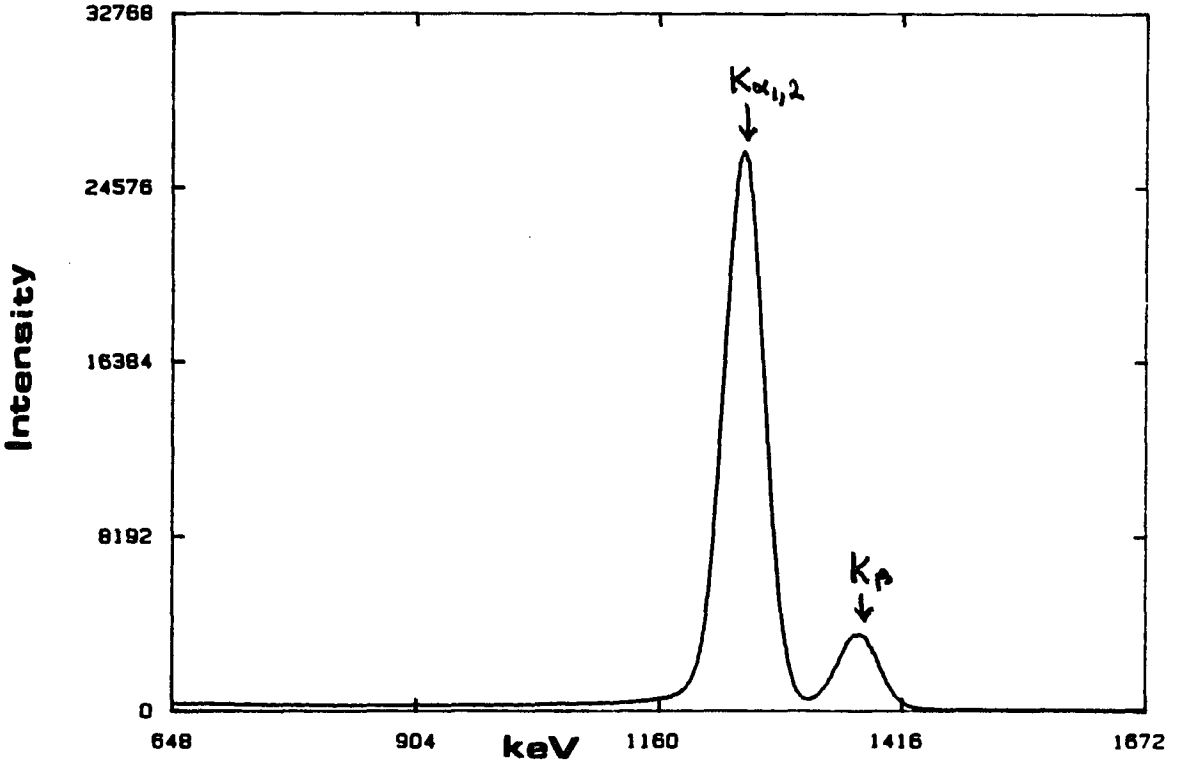

Fig.IV.2 V K x-ray spectrum produced in-beam from 2.0 MeV proton bombardment

For the low energy region using Montenegro's method, aliquots of 100 μl containing between 10-20 μg of the following elements were deposited and

evaporated using an infra-red lamp on 6.3 μm Mylar backings: Ti, V , Cr, Fe, Co, Ni, Cu, Zn, Ga and Ge. This method has been used routinely in our lab over the past 10 years for PIXE analysis.

The RBS spectra collected from these standards did not resemble the well resolved ones we obtained with the MicroMatter standards. Therefore no thickness measurements or RBS normalization could be used in conjunction with the x-ray data. However, for use in this method only, the K_α/K_β ratios are needed so that as long as the respective K x-ray lines of the standards were well resolved the data could be used in the linear fits to arrive at values of α and β. The same counting rate criteria were used in collecting spectra for this method as for the absolute method.

b. Calibration Points Obtained From Radioactive Sources

The high energy data points, $E_\gamma > 27.0$ keV, were obtained from three purchased sealed radioactive calibration sources. These sources were: Co-57, Ba-133 and the mixed source NBS-4275B. This last source contained the three radionuclides Sb-125, Eu-154 and Eu-155. The Co-57 and Ba-133 sources were purchased from Isotope Products, Pasadena, Ca. The NBS source was purchased from National Bureau of Standards, Gaithersburg, Md. The sources were all sealed in plastic. The Co-57 and the Ba-133 were covered by 7.33 mg/cm^2 Kapton while the NBS source was covered by approximately 10 mg/cm^2 polyurethane. The energies, branching and decay ratios of the Co and Ba sources were taken from Campbell [33] while the relevant data for the NBS source was taken from Hoppe and Schima [34].

These sources cover the energy range of 6.41 keV (Fe K_α x-rays from Co-57) to 1.50 MeV (Eu 154 γ-rays). Calibration attempts using the L x-rays of Cs, Te and Gd from the Ba source and the mixed NBS source to supplement the low energy data were discarded. The accuracy of using these L x-rays is suspect not only because of large uncertainities in the associated nuclear and atomic transition probabilities, but also because of the large attenuation in both the source itself and the "thick" plastic coverings. Co-57 provided Fe K_β x-rays at 7.05 keV and 14.41 keV γ-rays as well as the Fe K_α lines.

The sources were placed on the target ladder in the scattering chamber and positioned parallel to the detector face and to the beam axis. The reason the sources were placed parallel to the detector face was because the Co-57 and Ba-133 sources could not be seen through the Kapton covering although the NBS mixed source was clearly visible, if the sources were placed at 45 degrees as the in-beam calibration standards were, large uncertainities would arise as to the actual locations and dimensions of each source that the detector actually saw (recall the discussion on source uniformity when the sources are purchased ones). Cipolla employed correction factors for the non-uniformity in regards to the active source placement, but it is not clear from his papers that these corrections could be applied to any general counting arrangement or were specific to his own experimental arrangement.

The counting times used were 24 hours in order to accumulate good statistics. The chamber was evacuated to a pressure of 10 μm to minimize any attenuation effects by air. Although, as was the case with the data collected in-beam, an air gap of roughly 0.400 cm was interposed between

the 12.5 μm Kapton window on the chamber and the Be entrance window on the detector housing. Fig IV.3 shows the spectra of NBS-4275B. The most prominent lines used in the calibration are Te K_{α} x-rays, Gd K_{α_1},K_{α_2},K_{β_1},K_{β_2} x-

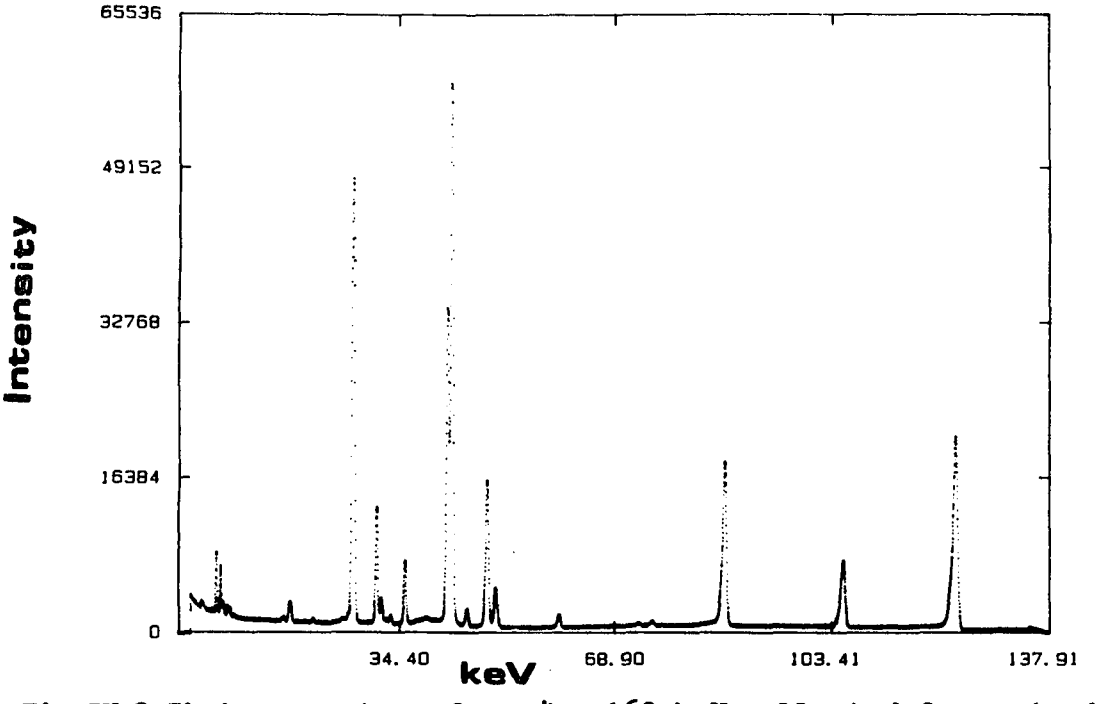

Fig.IV.3 Photon spectrum from 4 - 160 keV collected from mixed source NBS-4275B containing the radioisotopes Sb-125, Eu-154 and Eu155

rays and the γ-rays at 86.5, 105.5 and 123 keV.

B. Experimental Results

i). Absolute Energy Effiency Calibration

The experimentally obtained calibration results incorporating both the absolute in-beam determinations and the photon lines from the three radi-

oactive sources are shown in Table IV.1. Some duplication between the in-beam and source methods of calibration provided a means of checking the accuracies of both . The energies duplicated were 6.41 keV, Fe K_α x-rays and at 27.4 keV, Te K_α x-rays. Also the 14.41 keV γ-ray from the Co-57 source could be compared with Y K_α x-rays at 14.93 keV.

Having two more datapoints in the energy region where ε_{abs} is still lowered due to Ge K edge effects was also thought to be advantagous and was obtained using Y K x-rays. The duplication at the Fe K_α x-ray energy was extemely important because it is precisely for these low energy lines that purchased sources have developed a somewhat suspect reputation for accuracy. This reputation is precisely the impetus behind the innovation of doing in-beam calibrations, either based on absolute measurements, or the fitting approach of Montenegro.

It can be seen from Table IV.1 that the agreement between the values of ε_{abs} for 6.41 keV is not good, the value of ε_{abs} from Co-57 is about 20% too low relative not only to the value of ε_{abs} found in-beam, but also to the values of ε_{abs} obtained for $E\gamma$'s nearby. This is not totally unexpected in the light of our own and other (published) suspicions regarding radioactive low energy x-ray sources.

The agreement between the values of ε_{abs} for the 14.41 keV γ-ray of Co-57 and the K_α x-rays of Y which were produced in-beam and the values of ε_{abs} for the Te K_α x-rays produced from Sb-125 K-Shell internal conversion and those produced from 2.0 MeV proton bombardment is quite good. We feel the absolute in-beam method is reliable when directly compared with x-rays or γ-rays emitted from calibration sources sufficiently energetic so that attenuation problems, source migration etc. are unimportant.

The experimentally obtained absolute efficiency curve from 2.62 - 160 keV is shown in Fig.IV.4. Three distinct regions can be seen, a low energy region below 11.10 keV, a middle energy region where the Ge K edge is very influential in affecting the value of ε_{abs}, and a high energy region which

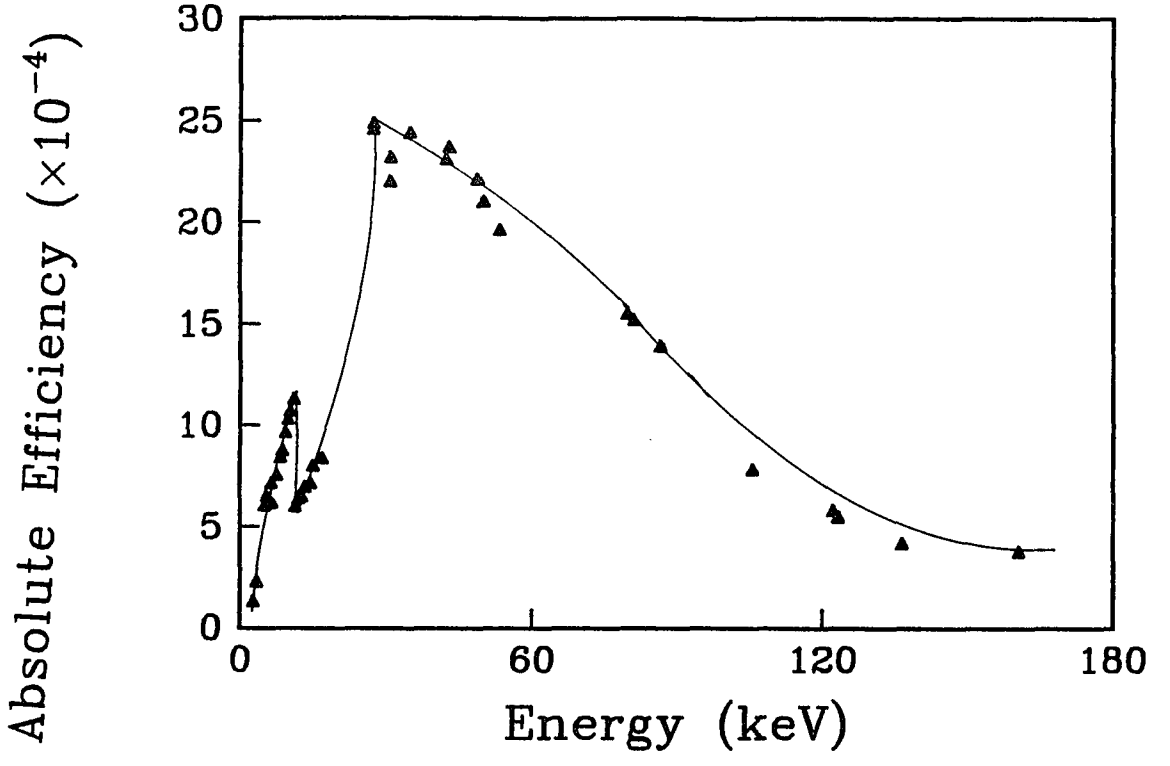

Fig IV.4 Experimentally determined absolute efficiency of a HPGe detector

from our data appears to begin at about 27.0 keV. In addition to the large discontinuity at 11.10 keV, another discontinuity can be seen at the high energy region around 31.00 keV. This discontinuity is not expected from a HPGe detector or any x-ray/γ-ray detector for that matter.

A look at Table IV.1 indicates that for both the Te K_β and the $Cs_{K\alpha}$ x-rays the values of ε_{abs} is lower than for the adjacent E_γ's in the immedi-

ate vicinity. A dropoff in ε_{abs} for one x-ray line of a particular element but without a corresponding drop for ε_{abs} for the other x-ray line whether it be K or L x-rays is usually a good indication that a crtical absorber of the line showing the anomalous behavior is present. The most likely scenario is that the absorber has a K or L absorption edge which is too high in energy for one of the lines while the line whose intensity is affected has an energy just slightly above the absorption edge. If an appreciable quantity of the absorber is present, attenuation effects can be observed due to the large increase in μ_{ab}.

The element responsible for this effect is Sb. Its presence in the detector can be seen in the calibration spectra. Recall the discussion earlier in this Chapter regarding photon sources as "probes". Uncovering Sb in a HPGe detector required a great deal of probing and understanding as to why a manufacturer would place it there and required considerable investigation into detector design.

Both Sb K and L x-rays can be seen in Fig.IV.5a,b. These Sb x-rays are only distinquishable in the spectra of Co-57. This is because in the spectra of NBS-4275B and in Ba-133, both the Sb K and L x-rays are overwhelmed in intensity by the lines emitted from the sources which happen to be close in energy to the Sb lines. The Co-57 source has no lines close in energy to either Sb K or L x-ray lines so that a careful inspection for "unusual" spectral features can turn up something. It is worth mentioning that a look back at the original printout from RACE of the Co-57 data showed that RACE had identified both the K and L x-ray peaks and had assigned peak areas to them.

This was an invaluable bonus to us in our understanding of the overall behavior of this detector and quite unexpected. We were able to use the peak area of the K_α x-ray peak to estimate the quantity of Sb in our detector, using the appropriate values of σ_{ph} for the $E\gamma$'s emitted from Co-57 which are higher in energy than E_K of Sb. A more detailed description of the effect of having Sb in the detector will be dealt with later in the Chapter.

The values of ε_{abs} obtained from the standard sources could be obtained from two well-known normalization methods. These are charge normalization and RBS normalization, both are well established in accelerator physics. We used both methods in arriving at the low energy values of ε_{abs}. The RBS method seemed to be more reliable. This could be due to the amount of beam steering that was done in order to keep the count rates down to minimize deadtime effects, or to the fact that our Faraday cup has a very narrow opening (ca.0.50 cm). This small opening was designed to be used with very thin targets (much thinner than the Mylar backed standards) so that beam dispersion through the targets caused some of the beam to miss the opening.

Regardless, using RBS for thickness measurements as well as normalization is not revolutionary and as can be seen in the RBS spectrum of ZnTe (Fiq IV.1) is quite a high resolution technique. The values of ε_{abs} at specific $E\gamma$'s can be obtained from (8):

$$\varepsilon_{\gamma abs} = \frac{4\pi Y(Kx)\varepsilon_p}{Y_p \sigma_{Kx} T} \left(\frac{d\Omega}{4\pi}\right)_p \left(\frac{d\sigma}{d\Omega}\right)_{ruth} \quad (8)$$

where $\varepsilon_{\gamma abs}$ is the absolute efficiency of the photon detector, Y(Kx) and Y_p are the measured yields of K x-rays and backscattered particles respectively, σ_{Kx} is the cross section for K x-ray production, $(\frac{d\Omega}{4\pi})_p$ is the solid angle of the particle detector, T is the transmission of the K x-rays through any window used as a vacuum seal on the chamber, $(\frac{d\sigma}{d\Omega})_{ruth}$ is the differential Rutherford cross section and ε_p is the efficiency of the par-

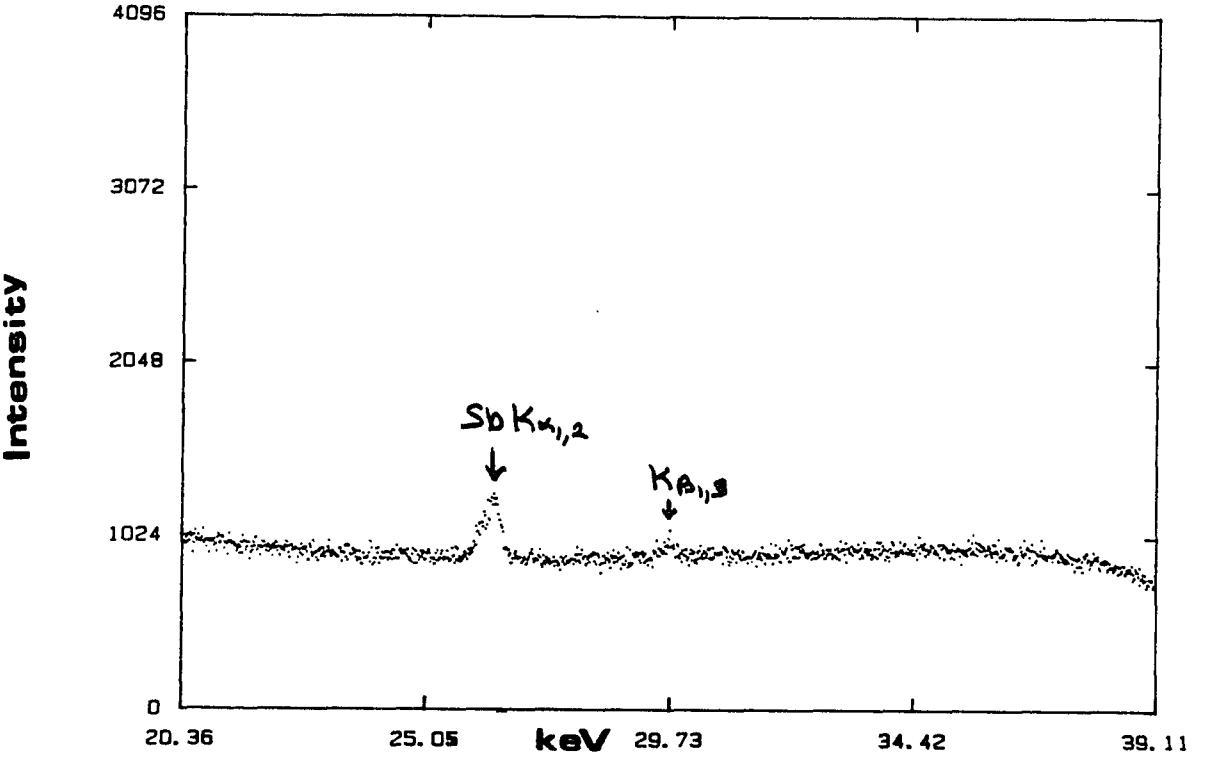

Fig.IV.5a Sb K x-rays found in Co-57 calibration spectrum

ticle detector which at these bombarding energies can be taken as unity.

The experimentally measured quantities in eqn. (8) are the yields of backscattered protons and the yields of the K x-rays. The quantities such as σ_{Kx} and the transmission of the K x-rays through the 12.5 μm Kapton can

be found in the literature. The values of μ_{ab} which were needed to calculate T for the characteristic K x-ray lines were taken from McMaster [35] and the values of σ_{Kx} were taken from the calculations of σ_{KI} by Cohen and Harrigan [36]. The appropriate conversions were made to arrive at the cross

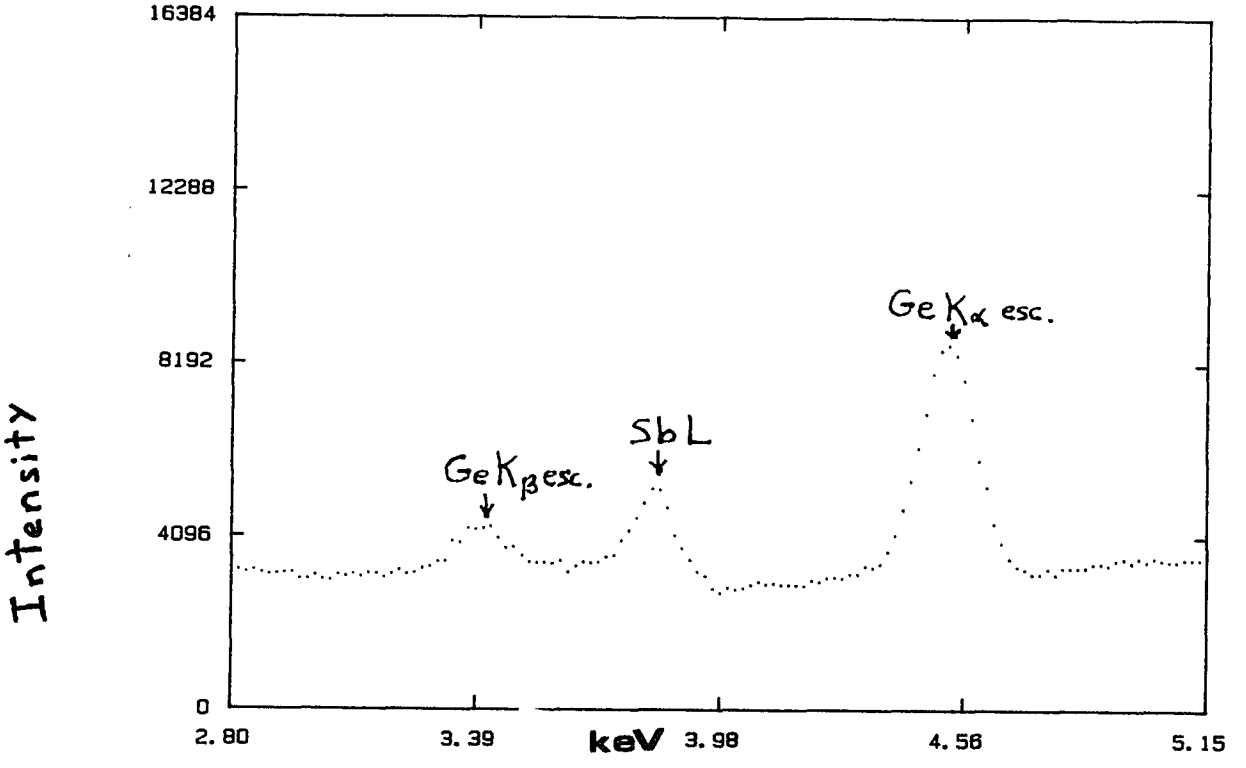

Fig.IV.5b Sb L x-rays and the Ge K escape peaks produced by the 14.41 keV γ-ray of Co-57

sections for K_α and K_β production. The uncertainties associated with the σ_{KI} caculations at these values of ξ_K are in the range of 2-6 % while the uncertainties in the atomic transition quantities needed to convert σ_{KI} to σ_{KX} are also in the range of 2-6 % for the Z's involved.

A very important consideration which, although related to the atomic transition probabilities, is typically overlooked is the inclusion of the effects the RA transitions have on the K x-ray peak areas obtained from a

code which fits the peaks to a Gaussian shape. The effects are generally minor for the K_α peak area, as was previously discussed in relation to Montenegro's method of calibration, the inclusion of the RA effects on K_β peak areas can be significant. This is as important for accurate calibration measurements as it is for accurate atomic physics measuremnts.

A look at Table IV.1 shows that for the elements used for in-beam calibration only the K_α linesof elements lighter than $Z < 28$ were used. This is because the measured $\frac{K_\alpha}{K_\beta}$ ratios were higher than Schofield's predictions. It has been established that RA transition probabilities are larger for the lighter Z elements. For values of $Z > 33$ the consideration of RA transitions affecting peak areas becomes unimportant.

We reiterate then that 2.0 MeV protons could not produce the kinds of multiple vacancy effects to alter these ratios. Even when we applied the correction for RA transitions for these elements the measured $\frac{K_\alpha}{K_\beta}$ ratios were not found to be at least equal to the theoretical predictions. These results meant of course that the values of ε_{abs} for the K_β energies of these elements could not be used since a lower value of efficiency for the higher energy x-rays is not consistent with the parameterization approach to analysing detector efficiencies. We have considered the effects of the Sb content of the detector as being roughly equivalent on both of the K x-ray lines of these lighter elements so that it should not be considered a situation peculiar to this HPGe detector.

The K_β energies that we did use in our calibration were corrected for loss in peak area due to "improper" Gaussian fits. This was done by adding

the intensities to the measured K_β peak areas based on Schofield's calculations of KMM transition probabilities. The corrections to the measured K_β yields varied from 3.8 - 2.9 approximately. The degree of correction necessary decreases with decreasing Z. Only after these corrections were made, were the values of ε_{abs} obtained for the K_β peaks were found to be consistent with the values of ε_{abs} obtained for the corresponding K_α line.

While it may be that the version of RACE used at the time to the data analysis was not quite efficient or sophisticated enough to accurately handle the closer K x-ray lines of these lighter elements, we feel that it is more a reflection on the importance of the effects of not only RA transitions being present and also of other unusual spectral features both in the peaks themselves and in the background. These features are certainly much more prevalent in the low energy region, $E_\gamma \leq 7.0$ keV than for larger E_γ's. The finding of the Sb K and L x-ray peaks and, as will be shown a bit later on, the deconvolution of L x-ray multiplets, indicate that RACE is capable of very accurate peak-fittings and area determinations.

ii). Absolute Efficiency Measurements in the Vicinity of the Ge K Absorption Edge

We paid careful attention to the energy region very close to 11.10 keV, the Ge K absorbtion edge. The closest we came in energy to the Ge K-edge was with Se K_α x-rays at 11.24 KeV. It can be seen both from Table IV.1 and Fig.IV.4 that the dropoff in ε_{abs} is quite steep. Not just for energies within one keV or so, but extending at least up to 17.67 keV, the

highest energy that a calibration point was taken were Ge K-edge effects can still be considered important.

The measured drop in ε_{abs} for the Se K_α x-rays corresponds roughly to 0.487 of the expected value for ε_{abs} if a simple extrapolation of the effiency curve in Fig.IV.4 is made. In fact the measured ε_{abs} of 5.89×10^{-4} is very close to the value of ε_{abs} of 5.94×10^{-4} obtained for V K_α x-rays. This is an interesting result when one considers that the values of μ_{ab} for the K_α x-rays of both elements in Ge have similar values [37]. It can be interpreted therefore, that the mean penetration depths of the the two different E_γ's in Ge must also be similar.

One important distinction between the two K x-rays based on energy considerations must be made, however. The V K x-rays are not nearly energetic enough at 4.95 keV to produce K-shell vacancies in Ge, while the Se K_α x-rays have a very large σ_{ph} for the K-shell of Ge. In fact not only is this the reason why the value of μ_{ab} for Ge makes its dramatic rise in magnitude for E_γ's $\approx$11.10 keV but the ratios between the values of σ_{ph} for

Table IV.2 Escape Probability of Ge K_α x-rays

Emitter	Incident Photon Energy, E_γ (keV)	Percent Escape
Se, K_β	12.47	15.08
Br, K_β	13.29	13.95
Co-57, γ-ray	14.41	11.70
Y, K_α	14.93	9.31
Y, K_β	16.73	8.22
Te, K_α	27.40	3.90
Te, K_α	30.97	3.20
Cs, K_α	30.95	2.81
Cs, K_β	34.92	2.49
Gd, K_{α_1}	43.00	1.05

the Ge K-shell and the Ge L_1,L_2 and L_3 also make a sudden rise [38].

This increase in the production of Ge K x-rays relative to the production of Ge L or M x-rays is the basis of the so-called K-shell jump ratio which takes place for all elements. The relative amount of Ge K_α escape peak area relative to the peak areas of the parent full energy peak is given in Table IV.2 and the relative areas of escape to parent peak plotted on a log-log scale is shown in Fig.IV.6.

The combination of a decreased interaction path in the detector crystal and the enhanced probability of producing Ge K-shell vacancies and therfore Ge K x-rays, results in the escape of Ge K x-rays from the active volume of the crystal, with the loss of either 9.88 keV for Ge K_α x-rays or 10.98 keV for Ge K_β x-rays. The escape peak energy will be equal to either E_γ - 9.88 keV if a Ge K_α x-ray has escaped, or E_γ - 10.98 keV if a Ge K_β x-ray has escaped.

The radiative decay width Γ is about 6.5 times greater for K_α emision in Ge than for K_β emission. Escape peaks for the Ge K_α x-rays will be more prominent than escape peaks from K_β escape. This mechanism of escape of K x-rays is also well known for both Si(Li) detectors [39] and NaI(Tl) [40]. Because of the much smaller values of both ω_K and E_γ for the Si K-shell, the probability of escape is smaller than in Ge.

The escape of Ge K x-rays is usually given as the sole explanation for the dramatic decrease in ε for E_γ's close to 11.10 keV for Ge detectors [41]. If we recall eqn. (1), escape probabilty was a factor that needed to be considered in evaluating ε. We have measured the peak areas of Ge K_α x-rays from incident E_γ's of between 12.47 keV (Se K_β x-rays) to 43.00 keV

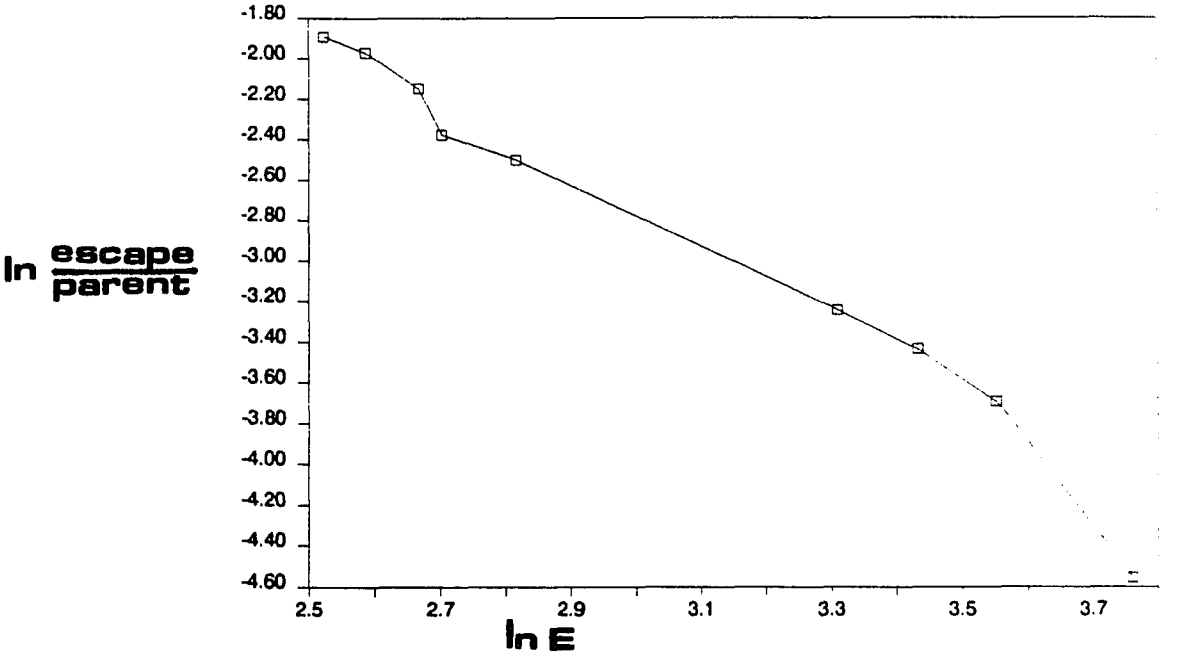

Fig.IV.6 Ge K alpha x-ray escape peak to full parent photopeak ratios

(Gd K_{α_1}). The peaks were identified by RACE and given peak areas after being fit to Gaussians. Fig.IV.5a shows the Ge K x-ray escape peaks from the 14.41 keV Υ-ray emitted by Co-57. In fact it was fortunate that these escape peaks were produced from a Υ-ray and not from K x-rays. In that case there would have additional peaks in that vicinity due to the escape of K_α and K_β x-rays which would have made identification of the Sb L x-rays more difficult. Escape peaks from Te and Gd K x-rays can also be seen in Fig.IV.3 although they are very weak relative to their parent peaks.

The values listed for the $\frac{\text{escape}}{\text{parent}}$ peak ratios as a function of parent peak energy are too small to account for the measured drops of ε_{abs}

particularly for those E_γ's quite close to the Ge K edge. Incidentally, we could not report any reliable values for the ratios for either Se or Br K_α x-rays. The reason for this is in the case of Se the escape peak is at 11.24 - 9.88 keV or 1.36 keV or nearly the identical energy of Se L_α x-rays of 1.38 keV. The Se L x-rays produced by 2.0 MeV proton bombardment are shown in Fig.IV.7. The very long, low energy tail that can be seen accompanying the Se L x-rays is an interesting phenomenon in itself. The subject of low energy tails to characteristic x-ray peaks was touched upon briefly earlier in this Chapter and will be given some more discussion later. The escape peaks from Br K_α x-rays have energy of 11.92 - 9.88 keV or 2.04 keV. Unfortunately, the Mylar backings that the calibration standards were on have high P contents (as any practicing PIXE worker can tell you). The energies of P K x-rays are nearly identical with the escape peaks of Br K_α x-rays so that no accurate peak area could be assigned to the escape peak in the presence of so many P K x-rays.

The amount of escape produced is a function of a number of variables. For a given type of detector material the most important of these are the proximity of the incident E_γ to E_K of the detector material, the counting geometry and the values of μ_{ab} for E_γ and E_{esc}. The ratio of escape peak formation to parent peak area can be calculated by:

$$F(\cos\theta) = \frac{\tau_K}{\tau}\,\omega_k[1 - \cos\theta\; r\; \ln(1 + (r\cos\theta)^{-1}] \quad (9)$$

where θ is the angle between the incident photons and the axis of the detector, r is the ratio of μ_{ab} for the parent and escape peaks in Ge, τ_K/τ is the Ge K-shell jump ratio at the value of E_γ for the incident photon and ω_K is the fluorescent yield of Ge.

Table IV.1
Absolute Energy Efficiency of HPGe Detector

Radioactive calibration source or in-beam elemental target	Energy (keV)	Absolute Efficiency	Type of Emission
Cl	2.62	$1.21 \times 10^{-4} \pm 5.4 \times 10^{-6}$	K_α
K	3.31	$2.20 \times 10^{-4} \pm 3.6 \times 10^{-6}$	K_α
V	4.95	$5.94 \times 10^{-4} \pm 8.6 \times 10^{-6}$	K_α
Cr	5.41	$6.40 \times 10^{-4} \pm 1.7 \times 10^{-6}$	K_α
Co-57	6.41	$6.06 \times 10^{-4} \pm 1.5 \times 10^{-5}$	Fe K_α
Fe	6.41	$7.04 \times 10^{-4} \pm 8.8 \times 10^{-6}$	K_α
Ni	7.47	$7.43 \times 10^{-4} \pm 8.1 \times 10^{-6}$	K_α
Ni	8.26	$8.30 \times 10^{-4} \pm 1.6 \times 10^{-5}$	K_β
Zn	8.63	$8.64 \times 10^{-4} \pm 3.6 \times 10^{-6}$	K_α
Ga	9.24	$9.54 \times 10^{-4} \pm 1.2 \times 10^{-5}$	K_α
Ge	9.86	$1.02 \times 10^{-3} \pm 1.7 \times 10^{-5}$	K_α
Ga	10.26	$1.06 \times 10^{-3} \pm 2.6 \times 10^{-5}$	K_β
Ge	10.98	$1.12 \times 10^{-3} \pm 2.9 \times 10^{-5}$	K_β
Se	11.24	$5.89 \times 10^{-4} \pm 8.4 \times 10^{-6}$	K_α
Br	11.92	$6.29 \times 10^{-4} \pm 7.6 \times 10^{-6}$	K_α
Se	12.49	$6.39 \times 10^{-4} \pm 2.6 \times 10^{-6}$	K_β
Br	13.29	$6.85 \times 10^{-4} \pm 1.5 \times 10^{-6}$	K_β
Co-57	14.41	$7.04 \times 10^{-4} \pm 2.1 \times 10^{-6}$	γ-ray
Y	14.93	$7.89 \times 10^{-4} \pm 1.0 \times 10^{-5}$	K_α
Y	16.73	$8.27 \times 10^{-4} \pm 1.6 \times 10^{-5}$	K_β
Te	27.40	$2.45 \times 10^{-3} \pm 3.4 \times 10^{-5}$	K_α
NBS-SRM-4275B	27.40	$2.48 \times 10^{-3} \pm 5.3 \times 10^{-5}$	Te K_α
Ba-133*	30.85	$2.19 \times 10^{-3} \pm 3.3 \times 10^{-5}$	Cs K_α
NBS-SRM-4275B*	30.91	$2.31 \times 10^{-3} \pm 1.0 \times 10^{-4}$	Te K_β
Ba-133	34.95	$2.43 \times 10^{-3} \pm 3.2 \times 10^{-5}$	Cs K_β
NBS-SRM-4275B	42.30	$2.30 \times 10^{-3} \pm 3.8 \times 10^{-5}$	Gd K_{α_2}
NBS-SRM-4275B	43.00	$2.36 \times 10^{-3} \pm 3.5 \times 10^{-5}$	Gd K_{α_1}
NBS-SRM-4275B	48.70	$2.20 \times 10^{-3} \pm 7.7 \times 10^{-5}$	Gd K_{β_1}
NBS-SRM-4275B	50.00	$2.09 \times 10^{-3} \pm 8.7 \times 10^{-5}$	Gd K_{β_2}
Ba-133	53.17	$1.95 \times 10^{-3} \pm 3.4 \times 10^{-5}$	γ-ray
Ba-133	79.63	$1.54 \times 10^{-3} \pm 5.3 \times 10^{-5}$	γ-ray
Ba-133	81.00	$1.51 \times 10^{-3} \pm 3.3 \times 10^{-5}$	γ-ray
NBS-SRM-4275B	86.50	$1.38 \times 10^{-3} \pm 5.7 \times 10^{-5}$	Eu-155 γ-ray
NBS-SRM-4275B	105.5	$7.69 \times 10^{-4} \pm 1.9 \times 10^{-5}$	Eu-155 γ-ray
Co-57	122.06	$5.70 \times 10^{-4} \pm 2.5 \times 10^{-5}$	γ-ray
NBS-SRM-4275B	123.14	$5.39 \times 10^{-4} \pm 8.0 \times 10^{-6}$	Eu-154 γ-ray
Co-57	136.42	$4.09 \times 10^{-4} \pm 1.7 \times 10^{-5}$	γ-ray
Ba-133	160.63	$3.69 \times 10^{-4} \pm 5.7 \times 10^{-5}$	γ-ray

* Both K x-ray lines not used in the fitted parameter efficiency calculations due their proximity to the Sb K-Shell absorbtion edge, 31.53 kev. See text for more detailed explanation.

The geometry used for the photon counting can be judged as belonging to three categories, good, fair or intermediate and poor based on the overall shape of a curve like Fig.IV.6 and the values of the escape/parent ratios, especially for those E_γ 's close to E_K of Ge. Although we were not able to obtain by experiment, escape/parent ratios for those E_γ's like the Se K_α x-rays, from the shape of our curve we can extrapolate the amount of escape down to E_γ's of 11.10 keV. In truth, most of the published studies do the same thing since it is not easy to obtain reliable peak areas for the lowest energy escape peaks.

From the shape of our curve and the values of the ratios, we can conclude that our counting geometry could be considered good. This means that the amount of escape taking place is very close to the minimum for all E_γ's. If the photons coming either from our calbration sources or in-beam method were not essentially parallel to the detector's axis there would be higher escape probability because the Ge K x-rays produced near the front face of the crystal would have relatively short paths to traverse in the crystal. Unfortunately, this realization that counting losses were kept to the minimum through the Ge K x-ray escape channels meant that total escape losses from both Ge K_α and K_β x-rays could not exceed 0.22, which is less than one half of the drop in ε_{abs} that we measured.

The next mechanism to look at in terms of a physical process responsible for the drop in ε_{abs} is for a loss in charge carriers. Two possible mechanisms which have been proposed are the escape of low energy photoelectrons, like those that would be formed close to threshold i.e. near absorbtion edges and the escape of Ge K-shell Auger electrons. When we

refer to detector escape for electrons, even for Ge K-shell Augers of roughly 9.5 keV energy, we are mainly considering the transport of the charge carriers to regions in the crystal of poor charge collection.

These regions of poor charge collection are generally near the front face and sides of the crystal, specifically the dead layer region. It is known that for $E\gamma$'s between 1.2 and 2.5 keV extremely long low energy tails are formed particularly for $E\gamma$'s near either Ge L edges or the Si K edge [41]. In fact, a look at the Se L x-rays in Fig.IV.7 illustrates these effects.

The mechanism responsible for charge carriers reaching the front dead layer is not completely understood. Originally it was thought to represent a fundamental property of Ge to "thermalize" photoelectrons produced near the front face of the detector. This allowed the photoelectrons to overcome the influence of the electric fields inside the crystal and diffuse to the dead layer without being properly collected. Those electrons arriving at the dead layer would not be registered in the full energy peak and therefore produce a tail. In fact, it became common to refer to this effect as a lenghtening of the dead layer at these specific values of $E\gamma$'s [42].

Recent studies [43] place more emphasis on the type of metal used to make a p type ohmic contact on the front face of the detector. This contact forms a Schotky barrier with the underlying n-type Ge. The height of this barrier and the uniformity and strength of the fields at this barrier plays the more important role in determining the efficiency of charge collection than do the transport properties of Ge.

The two most important considerations at very low photon energies for the situation near the Ge K-edge are: the distance inside the crystal where the photoeffect interaction takes place and that if electrons produced from this interaction do migrate to the dead layer of the detector, counts

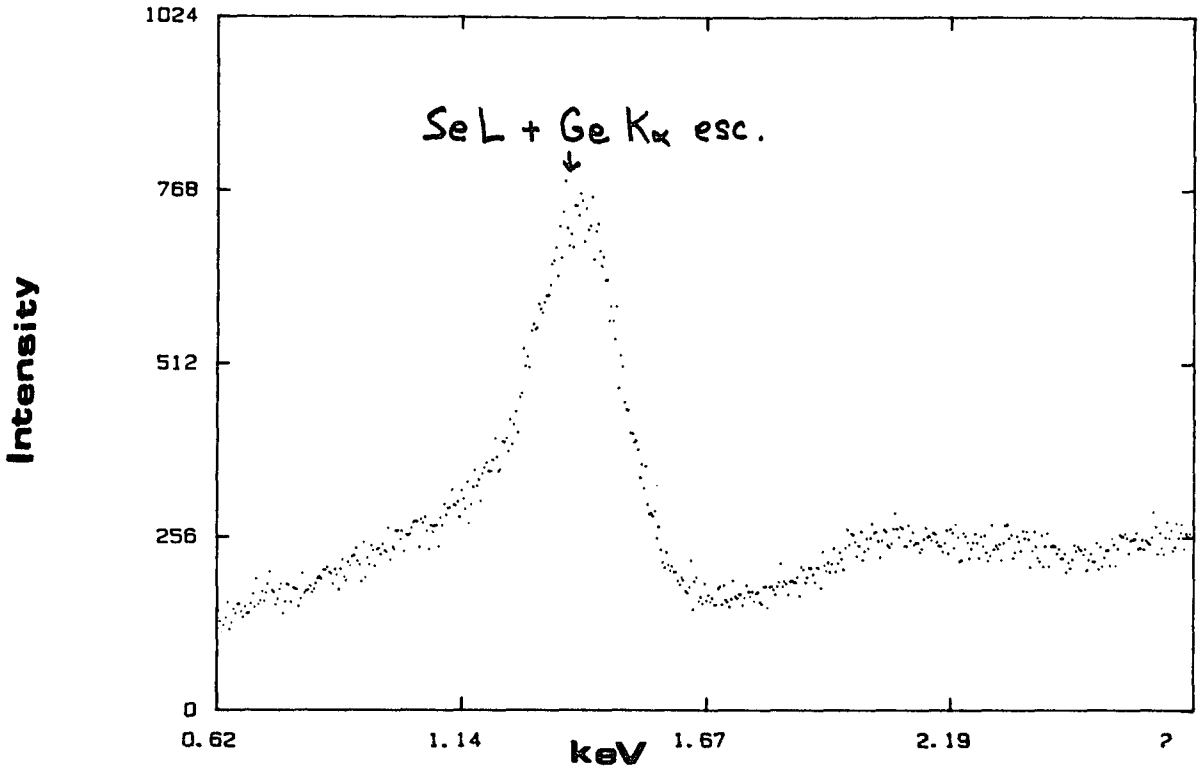

FigIV.7 Se L x-rays and Ge K alpha escape peaks produced from 2.0 MeV proton bombardment

will be registered in the spectrum although not in the full energy peak. The much longer than usual low energy tail that one would expect to see, would indicate that incomplete charge collection was taking place. The inability to collect spectra with well resolved peakshapes for x-rays of less than 2.50 KeV in Ge detectors is what generally convinces researchers not to calibrate Ge detectors at these energies or to use HPGe detectors

for any quantitive work at these low energies.

These effects of poor charge collection are not found in the spectra of any of the K x-rays of the elements that were used in calibration except for the the two lightest Z's, Cl and K. Here, low-energy tailing was observed but to a lesser extent than for the L x-rays of Br, Se and Y, all of which are below 2.0 keV. For both K and Cl, obtaining peak-to-tail ratios would be difficult to do, primarily because of the presence in the spectrum of continous bremstrahlung radiation produced from proton beam impact on the Mylar backing.

However the energy resolution of the Cl K_α peak is still remarkably good when compared to the low energy L x-ray lines that were recorded. The resolution at 2.62 keV is 140 eV FWHM and 240 eV FWTM (full width tenth maximum). Both values are remarkably good and seem to indicate that this HPGe detector may have some special features associated with it. The K x-ray spectrum of KCl produced from 2.0 Mev H+ bombardment is shown in Fig.IV.8. If one looks closely at the K_β peak of Cl, a "spike" almost at the center of the peak can be seen. The energy of that feature corresponds very closely to a KLL RA transition of K. RACE fit the entire Cl K_β peak around the spike, essentially treating the rest of the Cl K_β peak as a continously varying background and assigning a very small Gaussian peak area to the whole of the Cl K_β peak.

While we are quite aware that RACE was not designed to be sensitive enough to identify and assign peak areas to RA structures it is intriguing to see a case where a strong unusual spectral feature attracted so much attention at the expense of a rather obvious (to the eye of this experimenter) K x-ray peak. This occurence would seem to justify our concern

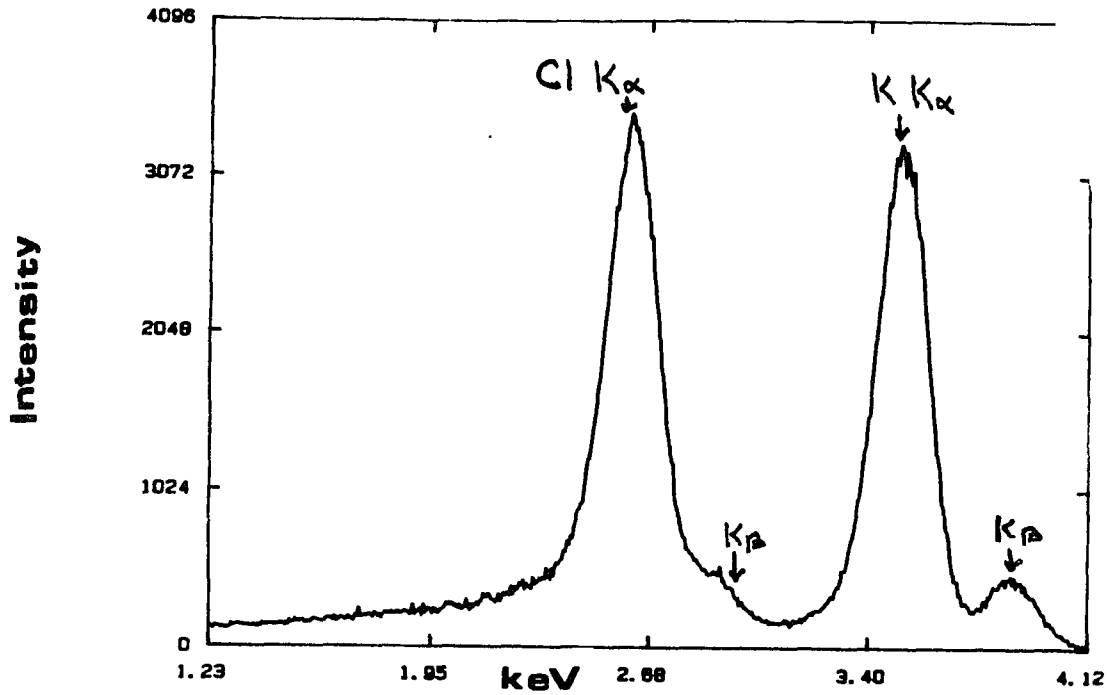

Fig.IV.8 K x-ray spectrum of KCl produced from 2.0 MeV proton bombardment

about the importance of RA transitions especially for accurate K_β peak areas. In addition it is comforting to have our faith in J.L.Campbell's work reaffirmed.

A look at the Se K x-rays, in particular the low energy side of the K_α peak, shows no indications of tailing behavior which could be interpreted as evidence of poor charge collection effects. The Se K x-ray spectrum collected from 2.0 MeV proton bombardment is shown in Fig.IV.9. The resolution of the K_α peak at 11.24 keV is 210 eV FWHM and 400 Ev FWTM. The ratio of peak-to-tail was found to be nearly 30:1. Therefore an argument involving the migration of charge carriers, either Ge K Augers or K-shell photoelectrons, to regions inside the detector or poor charge collection can not be true.

Further analysis of the situation validates this finding. For instance the E_γ used for calibration that was closest to E_K of Ge was the Ge K_β x-

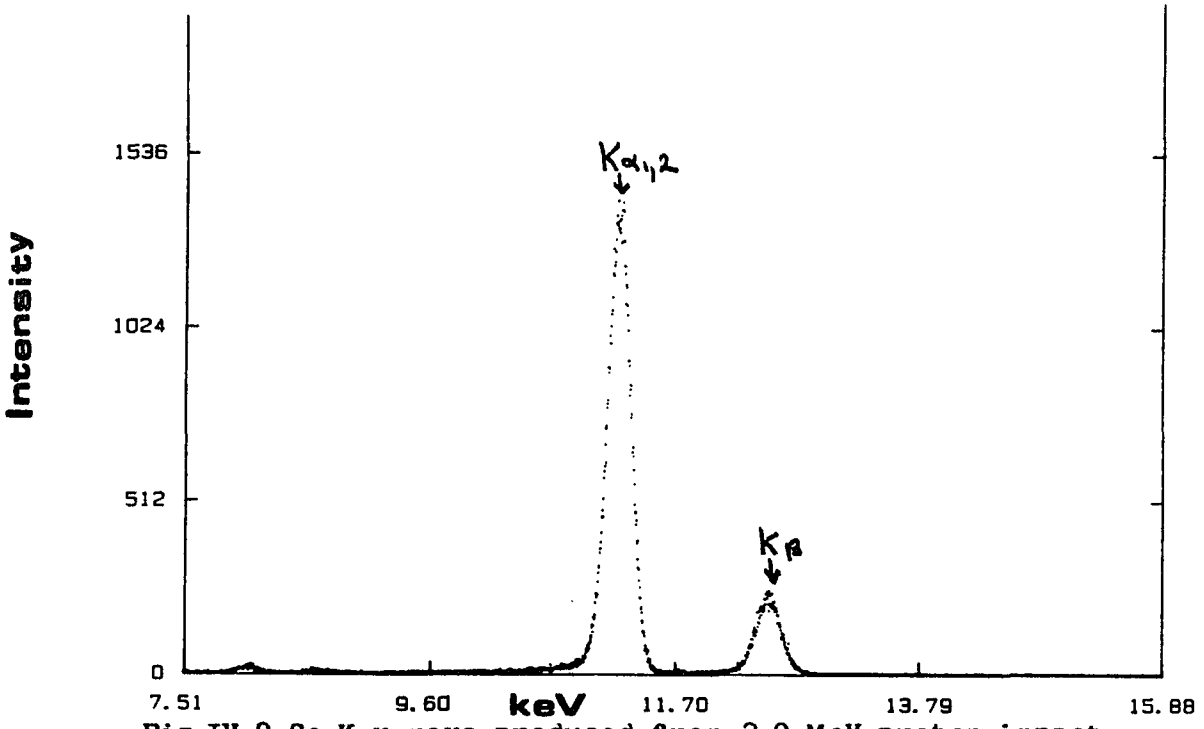

Fig.IV.9 Se K x-rays produced from 2.0 MeV proton impact

rays at 10.98 keV. If we assume that the other factors which contribute to peak shape and energy resolution such as: pre-amp and amplifier noise, and instability, background produced from the beam or from the accelerator, and the Fano factors of the two K x-rays under consideration which should be nearly identical, then we should expect to find practically identical resolutions and peak-to-tail ratios for the two K x-rays. The resolution is a bit better for Ge Kβ, 175 eV FWHM and 290 eV FWTM but the peak-to-tail ratio is only 8.5:1. The number of counts in the Ge K_β peak is only 0.076 of the Se K_α peak, however, so that the statistics are much better for the Se line. The Ge K_β spectrum is shown in Fig.IV.10

It should be kept in mind that the penetration depths of the two K x-rays are not equal. The Se K_α x-ray owing to its higher value of μ_{ab} pene-

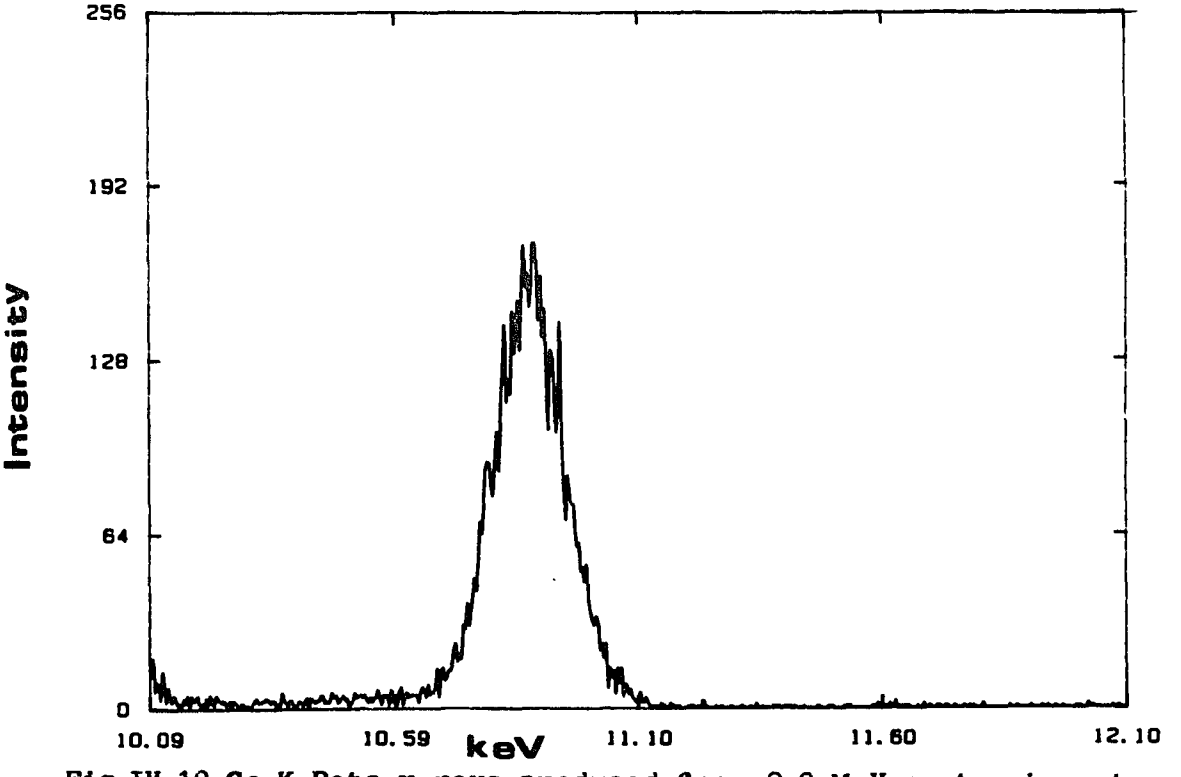

Fig.IV.10 Ge K Beta x-rays produced from 2.0 MeV proton impact

trates to only 0.10 the depth in the Ge crystal that the Ge K_β x-ray does. Therefore if charge migration from Se x-rays interacting with the Ge K-shell via the photoeffect were to occur it would be liklier for Se than for incident Ge K_β x-rays, but no evidence of this is seen in the recorded spectra. Furthermore, the penetration depth of the Se K_α x-rays is on the order of 8.0 μm. We have very good reason to believe from the peak-to-tail ratios for the low energy L x-ray spectra of Se, Br and Y that the dead layer of this HPGe detector is only 0.15 - 0.20 μm thick; a very modest value. This thickness, even at those energies where the dead layer is said

to be elongated is extremely small and probably can be considered roughly 0.10 μm thick for higher $E\gamma$'s.

The ranges of low energy electrons in Ge [44] can be calculated from:

$$R\ (nm) = 90\ \rho^{-0.8}\ E^{1.3} \qquad (10)$$

here R is the range of the electrons in nm in a particular substance, ρ is the density of the substance in g/cm^2 which for Ge is 5.53 and E is the energy in keV of the electron.

For Ge, ω_K is 0.554 so that nearly 0.45 of the K-shell vacancies are de-excited from non-radiative processes, predominantly Auger emission. The energies of Ge K-shell Auger electrons range from 8.28 - 9.75 keV [45]. Using eqn. (10) one calculates that for the ranges of Ge K-shell Auger electrons are between 0.35 - 0.40 μm. This is a much shorter mean free path than the average penetration depth of, say Se K_α x-rays, so that is not very probable that K-shell Augers emitted following K-shell vacancy formation after photoionization induced by Se K_α x-rays could migrate out to the dead layer on the front face of the detector's crystal even if a very large dead layer thickness of perhaps 1.0 μm was assumed. The ranges of very low energy Ge K-shell photoelectrons have much shorter values and are even more unlikely to reach the dead layer.

Even without physically acceptable mechanisms we feel reasonably confident that the values of ε_{abs} for this energy region as well as the low energy region are accurate. As another piece of evidence of the efficiency drop measured is realistic, we offer some relative measurements taken with

elements that either have K x-rays or L x-rays that straddle the Ge K-edge.

The elements used for this were: As which has K_α x-rays at 10.53 keV and K_β x-rays at 11.72 keV, Ta which has $L\gamma_1$ x-rays at 10.89 keV and $L\gamma_{2,3}$ x-rays at 11.25 keV and W which has all of its $L\gamma$ lines above the Ge K-edge, the most intense being the $L\gamma_1$ at 11.29 keV. In a manner similar to using K_α/K_β ratios we can use the changes in the intensity drops of the L lines as a strong indicator as to whether our absolute measurments were accurate. Of course for the As K x-ray we are using ratios but with a little twist in that here the higher energy K x-ray is significantly less efficiently detected. Also for As the changes in ε are so large that small effects like RA transitions make insignificant contributions.

One can in a somewhat crude but nevertheless accurate way, assume that the K x-ray ratios are not affected by the beam energy used, which is far from true for L x-ray relative intensities. Therefore, in order to interpret our results properly we must be aware of some of the collision dynamics of low energy proton induced L-subshell cross sections for high Z elements such as Ta and W.

To use the relative x-ray intensities for proton bombardment we have two concerns: the first is the accuracy of σ_{Li} cross section obtained from a well tested and reliable theory such as ECPSSR and the second; the accuracy of the atomic parameters that relate to values of ω_{Li}, f_{12}, f_{13} etc. Fortunately, Cohen and Harrigan [46] have taken much of the bother out of these considerations by tabulating σ_{Lx} for proton impact over the energy range of 0.100 - 10.0 MeV.

Cohen [47] has tabulated the expected accuracy of the L_1, L_2 and L_3 subshell ECPSSR cross section calculations for H^1 and He^4 impact compared to the published experimental results as a function of ξ_L. Not surprisngly, at larger values of ξ_L (higher projectile energies) ECPSSR and the experimental values of σ_L are nearly identical. This is precisly the situation for σ_{KI} values for the elements that were used in the low energy calibrations. Incidentally, Campbell [48] has recently published some new experimental results of L subshell transition probablities such as ω_{L_1},f_{12} etc. for high Z elements which should be very useful in making accurate conversions of σ_{Li} to σ_{Lx}.

Our results of the relative intensities of Ta and W L x-rays represent the yields of L x-rays produced by 2.0 and 3.0 MeV proton impact. At these projectile energies and for these target L subshell electron velocities the values of ξ_L range between 0.7 - 0.8. The values of σ_{L_3} as predicted from ECPSSR are found to be lowere than the measured values by about 6.5 %. For σ_{L_2} the underprediction is about 19 % and for σ_{L_3}, ECPSSR underpredicts the experimental results by 3 % .

Those limits on the accuracy of ECPSSR σ_{Li}'s are important to keep in mind when judging our L x-ray ratios. The experimentally obtained ratios for Ta and W L x-ray ratios are shown in Table IV.3 a,b. corrected for the differences in ε_{abs} which were determined from our low energy calibrations. These ratios were chosen on the basis of the following considerations: firstly to indicate the relative drop in ε for two x-ray lines similar in energy such as Ta $L\gamma_1$ and Ta $L\gamma_{2,3}$ but on opposite sides of the Ge K-edge. Secondly, $L\beta_1/L\beta_2$ ratios of W were chosen both as an indicator of the accuracy of the low energy points since for both Ta and W these L x-ray

lines are close in energy to the in-beam calibration points obtained with Ni, Zn and Ga. Thirdly, the $L\alpha_{1,2}/LY_1$ of Ta and W was chosen because $L\alpha_{1,2}$ is statistically the most significant line and because for W this ratio represents the drop in ε for the LY_1 line which lies over the Ge K-edge but a drop which is not as severe as for Ta $LY_1/L_{2,3}$ ratios. The Lβ ratios demonstrated to us the ability of RACE to accurately deconvolute L x-ray multiplets. A spectrum showing Ta LY_1 and Ta $LY_{2,3}$ x-rays produced by 3.0 MeV

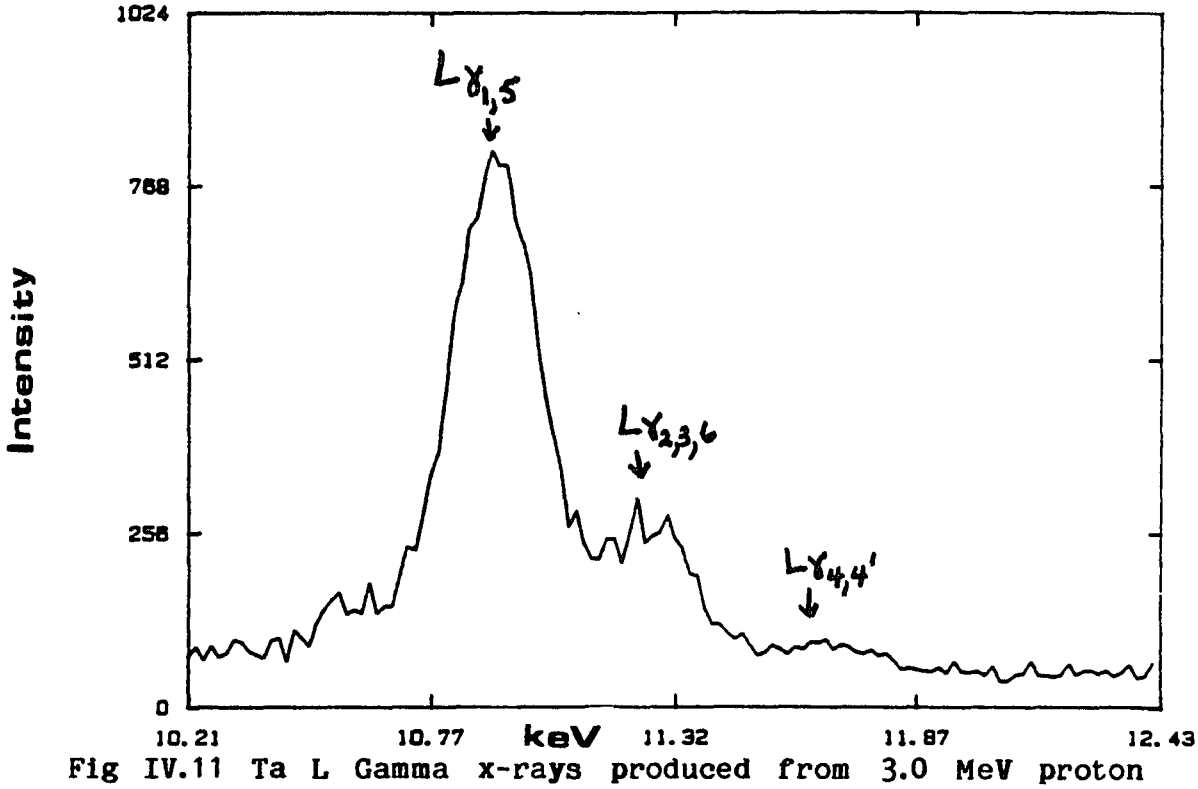

Fig IV.11 Ta L Gamma x-rays produced from 3.0 MeV proton impact

proton bombardment is shown is Fig.IV.11.

These results showing the changes in the measured L x-ray ratios predicted from ECPSSR (while paying some attention to the magnitude of deviation from the experimental results) lead strong credence to the auth-

enticity of both our low energy values of ε_{abs} and the values of ε_{abs} very close to Ge K edge.

The As relative measurements produced a Kα/Kβ ratio of 8.99, whereas Schofield's theoretical value is 5.41. We can extrapolate from the efficiency curve of Fig.IV.4 a value for ε_{abs} at 11.72 keV, the As Kβ x-ray energy as if ε had not dropped to the extent it had. A value of ε_{abs} for the As Kα x-ray at 10.55 KeV can be found by interpolating between the values of ε for the Ga Kβ and Ge Kβ x-rays. These two values can be used to predict the As Kα/Kβ (if no Ge K-edge effects had intervened). The Kα/Kβ ratio with no edge effects would have resulted in a smaller Kα/Kβ ratio than the theoretical value, a value of 5.06. The difference between this predicted value if no Ge K edge effect was present and the measured one of nearly 9.00 represents a drop in ε_{abs} of roughly 44 %. We emphasize that these relative measurements are not as valid as our absolute ones, however they certainly agree quite well with each other. The As K x-ray spectrum is shown in Fig.IV.12.

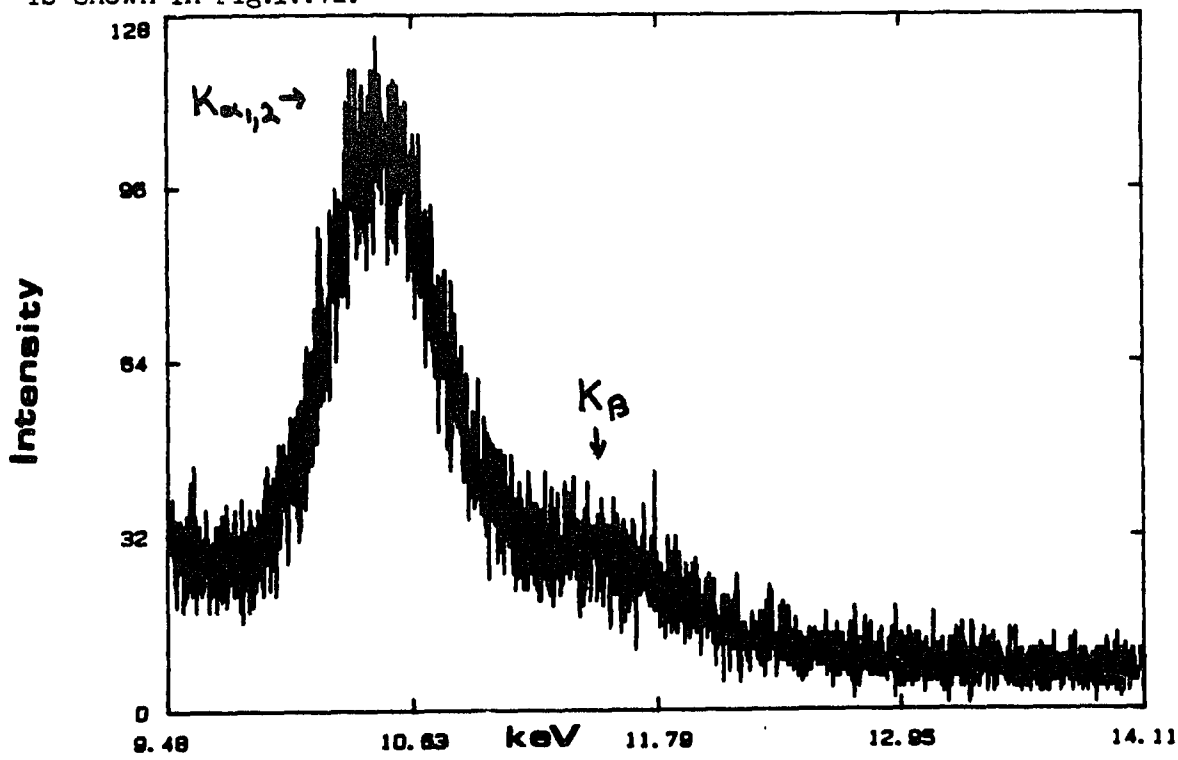

Fig.IV.12 As K x-rays produced from 2.0 MeV proton impact

Table IV.3a
Ta L x-ray ratios produced by Proton Impact

	$L\gamma_1/L\gamma_{2,3}$			$L\alpha_{1,2}/L\gamma_1$		
	Measured	Corrected for ε_{abs}	ECPSSR	Measured	Corrected for ε_{abs}	ECPSSR
2.0 MeV	8.05	3.95	3.65	16.97	21.11	16.60
			(4.02)[1]			(19.1)
3.0 MeV	4.02	1.97	2.09 (2.19)	17.8	21.83	15.27 (18.94)

[1] values in parentheses represent best fit of previously published experimental data according to Cohen [47]

Table IV.3b
W L x-ray ratios produced by Proton Impact

	$L\beta_1/L\beta_2$			$L\alpha_{1,2}/L\gamma_1$		
	Measured	Corrected for ε_{abs}	ECPSSR	Measured	Corrected for ε_{eps}	ECPSSR
2.0 MeV	2.06	2.12	1.55 (1.79)	25.42	18.09	16.82 (20.86)
3.0 MeV	2.30	2.36	1.68 (1.95)	23.96	17.04	15.44 (18.73)

4. Absolute Efficiency Measurements in the High Energy Region

The high energy region was taken as $E_\gamma > 27.0$ keV, and for our purpose extended to measurements up to 160 keV. From eqn.(2), this is the region where almost all of the photons are energetic enough to reach the active area of the crystal. Nearly all of the factors which served to either lower ε_{abs} or to degrade performance are inconsequential for E_γ's of this energy. As was pointed out previously in this Chapter, an advantage of using a Ge detector with the same area as a Si(Li) detector is that due to the Z^5 dependence of σ_{ph}, a Ge detector will be considerably more efficient at higher E_γ's.

All of the calibration points used in this energy region were obtained from the three calibration sources mentioned earlier. One advantage of the mixed NBS source (besides the large number of calibration lines it provides) is that the decay rates as of a specified date are provided by NBS upon receipt of the source. This makes life a bit easier in terms of not only the work involved in calculating the emission rates of particular E_γ's on particular date but also one develops a sense of security when using a NBS certified calibration source. There is a tendency to do much less cross referencing of decay rates, etc. with a NBS source than with a source supplied by a commercial distributer. Also we found workers at NBS to be very cooperative and helpful in both supplying information about the sources and calibration methods.

Branching ratios for the other radioisotpes used in the calibrations were found to have "literature" values that quite often varied by 10% from each other. It is therefore conceivable that the differences between values of ε_{abs} for γ-rays that are very close in energy but were emitted from different sources arose from uncertainies in branching ratios, internal conversion probablities, electron capture probabilities from K,L_1 shells etc. The same can be said about the atomic parameters such as ω_K etc. especially for the K x-rays that were used.

The pronounced anomaly that was observed in the case of the Te Kβ and the Cs K$\alpha_{1,2}$ x-rays was at first thought to be traceable to the types of uncertainites mentioned in the preceding paragraph, particularly in the case of the Cs x-rays. The evidence of Sb being present in the detector as witnessed by the presence of Sb x-rays, is a very likely cause for the observed changes in the Kα/Kβ ratios of these elements. The fact that the Te K x-rays of the NBS source deviated in their ratio as much as the Cs K x-rays which were emitted from the Ba-133 source is a good sign that the effect of Sb attenuation was real and not an artifact or calculation error.

Nevertheless, the Te Kα calibration point was checked in-beam by 2.0 MeV proton bombardment of ZnTe and the value of ε_{abs} determined using the previously described calibration method. No attempt was made to use the Te Kβ x-rays produced in-beam as a calibration point. The agreement between the NBS source at 27.4 KeV (the energy of the Te Kα x-rays) and the in-beam results is shown in Table IV.1. We measured a value of ε_{abs} of 2.45 x 10^{-3} in-beam and 2.48 x 10^{-3} from NBS-4275B. The Cs Kα and Te Kβ lines which are both within less than 400 eV of the Sb K absorption edge of 30.49

keV were not included in the model fitting approaches to calibration. These data points are shown in the effiency curve however.

The rest of the high energy points are rather well behaved with two possible small exceptions, the Gd Kα x-rays, and the points in the vicinity of 122 - 123 Kev. As for the Gd Kα x-rays we may have been a bit overzealous in our application of RACE in using it to separate completely the $K\alpha_1$ x-rays from the $K\alpha_2$ x-rays. At these energies (42.00 keV), the Kα lines of the rare-earths are just becoming visibly distinct from each other. In the next Chapter K x-ray spectra of rare-earths taken in-beam will be shown.

The background produced in-beam with low energy protons is quite a bit less than background generated by Compton scattering of high energy γ-rays. Recall that NBS-4275B emits γ-ray lines of nearly 1.50 MeV. NBS did not recommend using the two Gd Kα lines in calibrations but rather gave an emision rate for the total Gd Kα x-rays. Again the (mis)application of some of the atomic data pertaining to K-shell emission rates of Gd could have contributed to some discrepancy in efficiencies obtained experimentally.

The disagreement between the ε values at 122.06 keV (Co-57 γ-rays) and 123.14 keV (Eu-154 γ-rays) of some 5.4 % could best be explained either by source positioning uncertainties or uncertainty in the decay rates of the γ-rays. NBS claims [34] a total uncertainity of 1.1 % in the emission rate of the 123.14 keV γ-ray. The Co-57 source was not visible to the eye while the NBS source is clearly visible through its plastic covering. The decay rate of the γ-rays of Co-57 were taken from Lederer [49] while the decay rates of Ba-133 were taken from Campbell [33].

A. Energy Efficiency Results From the Modeling Methods of Calibration

We have applied the modeling methods of calibration of both Cippola and Montenegro to a HPGe detector although both methods were originally proposed in the literature for Si(Li) detectors. The philosophy of both methods are identical and the roots of both lie in the parameterization method of Hansen, although the data are treated and acquired in slightly different manner.

For Ge detectors the 5-parameter non-linear fit method of Cippolla seems to be more appropriate overall than the 2 separate linear fits of Montenegro. In this regard a recent study of Budner [50] involving the effects of the Ge K edge on the performance of a HPGe detector seems to substantiate our findings that the linear fit of $K\alpha/K\beta$ ratios does not produce accurate values of ε_{abs} in the low energy region of a HPGe detector.

The two main problems, as we see it, with applying Montenegro's method to the low energy region is first the strong discontinuity in ε_{abs} caused by the Ge K edge. This seems to immediately invalidate the linear fit which appears to us to be predicated on a ε_{abs} smoothly varying with increasing E_γ's. This smooth variation guarantees that the low and high energy regions "mesh" seamlessly at some value of E_γ. From our experimental results this is clearly not possible for a HPGe detector.

The problem of the detector material's K-shell absorption edge severely effecting an attempt to arrive at accurate ε_{abs} values was dealt with by Cipolla for the case of Si(Li) detectors. Using two separate 5-parameter non-linear fits, one for low energy points below E_K of Si and one for all of the points above E_K, Cipolla was able to arrive at two distinct sets of values of the low energy coefficients α and β while the high energy coeffiecients γ and δ were invariant. It was this modeling approach

that worked best in our case.

In addition to problems of dealing with the Ge K-edge effects on ε_{abs}, we have also encountered difficulties in obtaining $K\alpha/K\beta$ ratios for light Z elememts ($Z \leq 28$) that are smaller than predicted by theory when the K x-ray peaks are fitted to Gaussian shapes, in our case the peak fitting and analysis was done by the code RACE. If the values of $K\alpha/K\beta$ are not smaller then the theoretical ratios than no values of α and β can be obtained by the linear fitting method. It should be pointed out that the low energy linear fit gave a value of 1.18 for χ^2. Nevertheless the values of ε obtained from using the α and β from that fit were still 2 - 3 times higher than the experimentally determined in-beam values or for that matter the ε_{abs}'s derived from the α and β values of the 5-parameter fit for E_γ's < 11.10 keV.

The main contributions to this situation is the presence of radiative Auger lines embedded in the characteristic K x-ray lines of light elements. As pointed out by Campbell [9], the presence of RA transitions in K x-ray peaks fit to Gaussians invariably leads to reductions in the $K\beta$ peak areas, regardless of the mechanism of K-shell vacancy production. The $K\beta$ peaks are more heavily contaminated by KMM RA lines.

We attempted to compensate for the presence of RA peaks by adding intensities to the K x-ray lines of elements with $Z \leq 28$. We used Schofield's calculations for radiative two electron emission to estimate the amount of peak area lost by the Gaussian fitting. When this is done, $K\alpha/K\beta$ ratios smaller than predicted are obtained. This technique was also used to obtain meaningful $K\beta$ peak areas in our absolute in-beam method.

Unfortunately, the results when applied to the low energy linear fit are not impressive either in appearance or in their relation to the other

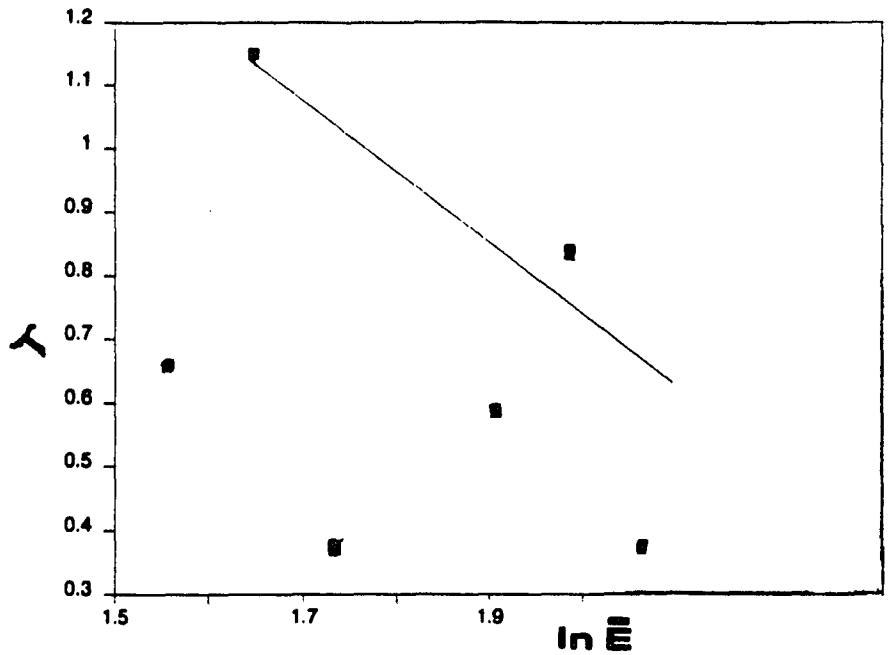

Fig.IV.13 Straight line fit of K x-ray ratios including RA corrections

low energy calibration data.The straight line fit including the effects of RA's is shown in Fig.IV.13

The results of the fits to both of the approaches are given in Table IV.4. There are two sets of values for α and β for both methods. The values of α and β for the 5-parameter non-linear fit is due to one fit for energies less than 11.10 keV and another fit for in our case $E\gamma$'s > 27.0 keV. The high energy coefficients are the same in both fits, an indication that the high enrgy region is practically independent of Ge K-edge effects.

This independence of the high energy region is manifested in the linear high energy fit as well. Inspection of Table IV.4 shows that contrary to the low energy condition the values of Υ and δ obtained from both fits are relatively close. The 5-parameter fit also gives the value of Ω which is very useful when making comparisons to the absolute efficiencies. The results of the straight-line fit for the high energy coefficients are shown in Fig.IV.14.

When compared with our absolute measurements, the values of ε_{abs} obtained using the values of α and β obtained with the linear fit both with and without the inclusion of RA's are between 2 - 3 times too high. The values of ε_{abs} obtained from the 5 parameter fit below 11.10 keV are within 10 - 15 % of our experimental values. The values of χ^2 for the 5-parameter fits were 118 for the low energy fit and 382 for the high energy fit

The high energy coefficients Υ and δ generated by the 5 parameter fit are found to give values of ε_{abs} which are within between 0.5 - 7 % of the experimental values for 27.4 keV < E_γ < 86.5 keV. For E_γ > 105.6 keV the agreement becomes progressively worse until it overpredicts the value of ε_{abs} at 160 keV by 44 % . This could be due to either an overweighting of data in the 30 - 90 keV region or to a inadequacy of the 5 parameter fit at higher E_γ's. The linear high-energy fit of Montenegro gives much better agreement with the ε_{abs} values precisely in the region above 90 keV. For instance it only overpredicts ε_{abs} by 15% at 105.5 keV and by 27 % at 160 keV. The reason for this behavior at higher E_γ's is not known at the present time.

Table IV.4

Values of Fitted Parameters Which Determine the Absolute Efficiency of a HPGe Detector Following the Various Methods of Montenegro and of Cippolla

Fitted parameter	Montenegro 2 linear fits 2-parameter	Cippolla et al. 2 separate 5-parameter non-linear fits	Cippolla 5-parameter non-linear
α	-4.06 -12.14*	-8.79[a] -	- -88.3[b]
β	-1.40 -1.88*	-0.963[a] -	- -2.00[b]
γ	-1212.2	-882.3	-
δ	-1.75	-1.60	-
Ω	N.A.[c]	2.75 msr	2.78 msr

a) Fit below K_{abs} edge of Ge only, no high energy data points used i.e. no points above 10.98 keV (Ge K_β x-rays)

b) Fit to high energy points only, i.e. above 27 keV

c) Montenegro's method does not give a fitted value for Ω

* Fit includes contributions to measured $K\alpha/K\beta$ ratios from Radiative Auger Transition Probabilities as recommended by J.L.Campbell

5. Effects on Detector Performance due to Sb Content

It was shown in a previous section of this Chapter that Sb was quite likely present in the HPGe detector used for this calibration study. If it was present it was also in all likelihood present at the front face of crystal. This was at first quite puzzling, typically the elements placed on the front face to form ohmic p^+-type contacts and Schottky barriers [51] are metals like Au, In, Pd, etc. Recall eqn. (2) used in the parameterization method which uses the amounts of absorbers at the front face of the detector in order to calculate the degree of attenuation for low energy x-rays.

Sb would not form a p^+-type contact on intrinsic Ge so there was apparently no good reason for a manufacturer to put it there. This puzzle became clearer upon stumbling onto a paper by Marrello [52] discussing Al and Sb epitaxial regrowth layers and contacts for Ge detectors. Interestingly enough, the paper stems from the same era as does the HPGe detector used in this study. It was claimed that contacts made by low temperature annealing ca. 300° C would be durable while the regrowth layer underneath the contact would be heavily doped with either Al or Sb. This doped layer was an alternative to ion implantation of Ge. It is known that ion implanted Ge has better charge collection properties at the front of the crystal [53]. This results in thinner dead layers with better low-energy resolution.

A n-type injecting contact and n-type regrowth layer of Ge at the front face of the detector would give better resolution according to the

predictions of Pehl [54] and of Hansen [55]. This is because of the higher uniformity of the electric fields produced by a n-type contact.

Armed with a motive on the part of the manufacturer for incorporating Sb, it became more likely that the K and L x-ray peaks of Sb we observed were due to some amoumt of Sb being present at the front face of the detector. We next performed a calculation of how much Sb could be present based on the amount of Sb Kα x-rays found in a Co-57 calibration spectrum which had been accumulated during a 24 hour counting period.

The Co-57 source was an ideal source to use to quantify and identify Sb. This is because there are no large peaks in the vicinity of the Sb K x-rays at 26.36 keV to obscure the small Sb peak. Also because Co-57 emits only two high energy γ-rays with energies higher than E_K of Sb it was realtively easy to use σ_{ph} for Sb at 122 and 136.4 keV to obtain the amount of Sb present in the detector. The calculation also required the values of ω_K, $\Gamma_{K\alpha}$ etc. as well as the emission rates of the γ-rays.

An amount of Sb equivalent to roughly 3.00×10^{18} atoms was calculated to be present. At first we rather naively thought that this amount of Sb was uniformly spread on the face of the detector producing a film of Sb approximately 9750 Å thick. This was before reading Marrello's paper whereupon we realized that more likely the contact was only 1500 - 2000 Å thick. The rest of the Sb would reside in the regrowth Ge layer at the face of the detctor.

The importance of this amount of Sb in whatever form or layer at the front of the detector was primarily its effect on the attenuation of low energy x-rays, in particular x-rays in the vicinity of 4.132 - 8.5 keV. The lower energy is the Sb L_3 edge and for photons of the range mentioned σ_{ph}

for Sb is nearly 1.97 x 10^5 b ! [56].

For instance if we apply eqn. (2) to V Kα x-rays at 4.93 keV and calculate the attenuation due to the various absorbers listed in Table IV.5 we would arrive at value of ε of 0.37. This is compared to a measured ε of 0.236. This was done with a uniform Sb content in mind. Some more investigation into Sb/Ge layers [57] lead us to believe that Sb/Ge regrowth layers are quite non-uniform. If for instance we assumed the 2000 Å contact layer and then the rest of the Sb residing in a front layer of the detector, but nonuniformly, we could calculate a ε of V Kα x-rays for 0.267. This is not a bad assumption considering the reputation of nonhomogeneity that Sb/Ge regrowth layers have [58].

The actual amount of attenuation caused by the Sb is not important because it is practically impossible in a consistent and verifiable way to

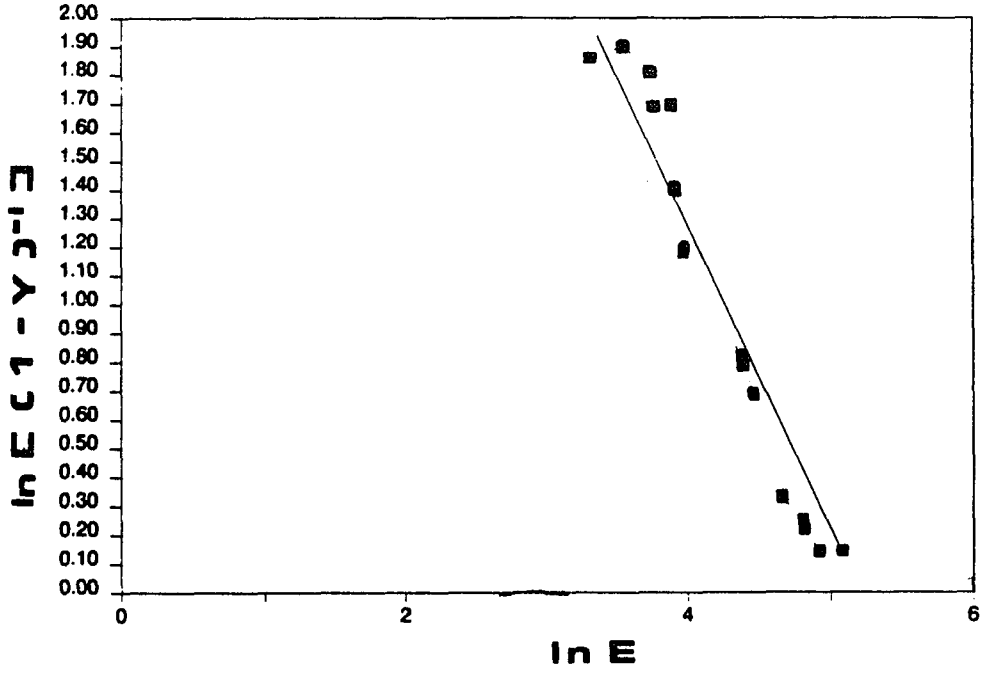

Fig.IV.14 High energy straight line fit

determine the total Sb content and its homogeneity. From our escape peak data we can feel relatively confident that the large majority of photons, whether emited from sources or produced in-beam, strike the detector parallel to the crystal's axis and are focused mainly on the center of the crystal. If the Sb were to migrate preferentially to center of the Ge crystal at some point in the low temperature annealing, or soon afterward, then attenuation effects of between 0.55 - 0.35 could easily be produced for E_γ's between 4.5 and 8.0 keV.

We feel that the possible ranges of Sb content at the front face of the detector are large enough to significantly affect ε for low energy x-rays. The excellent low energy resolution of this detector as witnessed by the KCl K x-ray spectrum and the anomalous behavior of the Te Kβ and Cs Kα x-rays are further evidence that this HPGe detector has a n-type contact layer of Sb and a regrowth layer of n-type Ge doped with Sb at the entrance window of the detector crystal. An illustration of how a regrowth layer of Sb/Ge could be prepared is shown in Fig. IV.15.

7. Conclusions

We have measured the absolute efficiency of a HPGe x-ray/Y-ray detector which apparently contained a Sb injecting contact layer on the front face. While the Sb contact may play a role in the good low energy resolution of this detector, the value of ε for low energy x-rays is strongly affected by the amount of Sb present. It should be remembered that this type of contact probably has a major positive influence on the detector's

low energy resolution when compared to other x-ray detectors.

The absolute efficiencies over a range of $E\gamma$'s from 2.62 - 160 keV were measured using a combination of calibration sources and in-beam standards. Particular attention was paid to obtaining data in the region where the Ge K-edge strongly effects the values of ε_{abs} for $E\gamma$'s near 11.10 keV. This region can not have its behavior modeled. Indeed, the influence of the Ge K edge may severely alter the accuracy of any modeling attempt that we are presently aware of.

The measured ε's in the Ge K-edge represent nearly 50% drops in ε for $E\gamma$'s very close to the Ge K-edge. These changes in ε are larger than can be accounted for from a consideration of Ge K x-ray escape peak production. Mechanisms of charge-carrier loss either through the detector volume or into the dead layer are not observed or can be shown by calculations to be highly improbable

Agreement between the measured ε_{abs} and the predicted ε's based on the modeling methods of detector performance in the case of a HPGe detector have been shown to be limited to certain narrow energy regions. In some regions and depending on the model used, agreement is very good. However no one model has demonstrated a high degree of accuracy over the full range of energies for a HPGe detector. The particular HPGE detector used in this study had some unusual characteristics which make it difficult to ascertain how much general information concerning the modeling approach to efficiency calibrations can be obtained based on the results of this study.

Table IV.5

Thicknesses of Absorbers In Front of Active Volume of the Detector Crystal

Type	Thickness of Absorber (g/cm^2)	Purpose
Kapton	1.25×10^{-4}	vacuum seal between detector and chamber
Be	4.9×10^{-2}	vacuum seal between detector crystal and outer environment, entrance window for photons
Au	1.1×10^{-5}	Ohmic contact between crystal and pre-amp
Sb	6.5×10^{-4}(a)	used by manufacturer to form injecting n type contact to improve detector performance
Ge (dead-layer)	1.09×10^{-5}	formed unintentionally during the detector's manufacture

(a) More accurately, we know the Sb content to be roughly 3.0×10^{19} atoms, the actual physical form and distribution of the Sb is not known to us but on the bases of information in the literature we can make some educated guesses.

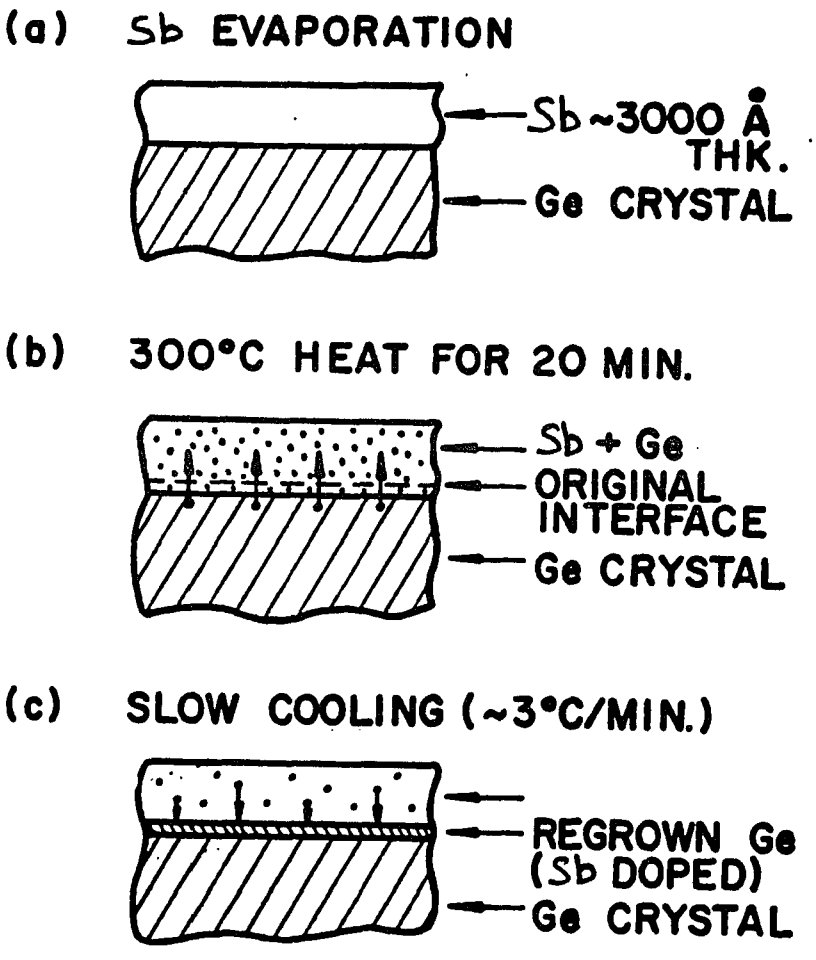

Fig. IV.15 Schematic diagram illustrating the concept of solid-phase regowth of an Sb film on a Ge substrate. During slow cooling the Ge regrows epitaxially on the Ge substrate. Taken from ref. 52.

Chapter V. Experimental Results and Discussion

1. General Outline of Goals and Methods

We have measured the K-Shell ionization cross sections, σ_{KI}, of the elements $_{59}Pr$, $_{60}Nd$, $_{62}Sm$, $_{69}Tm$, $_{73}Ta$ and $_{74}W$ with 1.0 - 3.0 MeV protons produced from the 3.75 MeV Dynamitron accelerator at Brooklyn College. The Nd target was prepared from 95% isotopically enriched Nd^{142}, while the targets of Sm contained natural Sm, 87.4% enriched Sm^{150} and 98.6% enriched Sm^{154}. The Sm^{150} and Nd^{142} targets were chosen on the basis of their nuclear properties, both are relatively spherical nuclides eliminating the contribution from K-Shell internal conversion following Coulomb excitation, IC-CE. Pr^{141} is a spherical nuclide.

The target of Sm^{154} represents the most strongly deformed Sm isotope and therefore contributes the most to the total K x-ray yield of Sm from the nuclear inelastic channel. The use of this target not only allowed us to check on the reliability of subtracting the K x-ray contribution from IC-CE (when compared to the total K x-ray yield from Sm^{154}) but also allowed us to try using a method of normalization which until now has only been tried on thick targets. This normalization method of Goclowski [1] relies on the accurate measurement of the yield of CE γ-rays while simultaneously measuring the yield of K x-rays.

The proton beam from the accelerator was magnetically analysed through two 60 degree bends before being directed into the scattering chambers where the targets were housed. The spread in beam energy was believed to be less than 2 keV. The design of the chamber was discussed previously in Chapter III.

Beam currents of between 70 - 300 na were used to produce both the x-rays and the CE γ-rays (in the cases where the targets contained deformed nuclides). Total integrated charges ranged from between 140 -3000 μ C and were collected in a Faraday cup at the exit of the chamber. The larger values of charge represent the longer running times needed to collect photon spectra with good counting statistics at the lowest beam energies and for the heavier targets, such as Ta and W.

Thin targets backed on 15 - 20 μ g/cm^2 C foils supplied by Arizona Carbon Co., Tucson, Arizona were used in all of the experiments. The lone exception to this was the WO_3 which was obtained from MicroMatter,Corp., EastSound, Washington. The use of thin targets reduces greatly the need to make any corrections to the beam energy due to losses of energy in the targets. Thin targets also eliminate the need to make corrections for losses in x-ray intensity due to attenuation effects in the targets.

Energy losses in the beam were calculated to be no more than 13 keV in the most severe cases i.e. the lowest beam energies with the thickest target. The typical energy loss was estimated to be between 8 - 10 keV. This amount of energy loss was to small too be measured using a solid-state particle detector placed at 150 degrees with respect to the beam. The resolution of the particle detector was usually in the range of 20 - 22 keV for the proton energies used. This was aproximately the quoted

energy resolution by the manufacturer (Paul Downey) for a 100 mm^2 area detector. The particle detector was covered by a graphite collimator in order to cut down on the particle counting rates which can become quite large if large beam currents are used. Graphite was used to prevent any x-rays or γ-rays from reaching the photon detctor and producing any unwanted background.

Target thicknesses had to be determined using a 1.6 MeV He+ beam. This was a bit risky because the target then had to survive the full range of proton energies first before switching to the He+ beam for the thickness measurement.

The thicknesses of the targets were: Pr 6.36 $\mu g/cm^2$, Nd 7.17 $\mu g/cm^2$, Sm (nat.) 32 $\mu g/cm^2$, Sm^{150} 21.5 $\mu g/cm^2$, Sm^{154} 32.5 $\mu g/cm^2$, Tm 29.3 $\mu g/cm^2$, Ta 17.7 $\mu g/cm^2$ and WO_3 54 $\mu g/cm^2$. The WO_3 target was backed on 6.3 μ m Mylar and its thickness was found to be within 10% of the quoted value of the supplier. The rare-earth targets were prepared in the manner described in Chapter III. The Ta target was prepared by passing 130 amps through a Ta tube placed in an evaporating bell-jar. The bell-jar was kept at 1×10^{-6} torr and the Ta metal deposited onto thin C foils.

The Nd^{142}, Sm^{150} and the Sm^{154} were obtained from Oak Ridge National Laboratory Isotopes Division. The remaining material in the samples were the other naturally ocurring isotopes of that particular element.

A 25 mm^2 HPGe Princeton Gamma-Tech solid-state x-ray/gamma-ray detector biased at -1000 V was used along with a Princeton Gamma-Tech 340 amplifier. The data acquisition system used was the EG & G ORTEC MCA software emulation system coupled to the amplifier via an EG & G ADCAM 911 multiplexer/ADC. Particle spectra were collected in the same manner as

the photon spectra.

A version of the program RACE [2] used in x-ray spectral analysis and modified for use by S.H.Greenberg was used to analyse the recorded photon spectra. Only peaks that were identified by RACE, that is, peaks that met the criteria established by RACE as having the proper widths, heights above neighboring background, etc. were used in the evaluation of experimental cross section calculations. This standard of peak identification and peak area determination practically eliminated the use of any of the CE gamma-rays except for the 82 keV gamma-rays from Sm^{154}.

RACE was routinely able to separate the $K\alpha_2$ x-rays of Sm from the $K\alpha_1$ x-rays based on line-shape considerations although they were not fully resolved by the photon detector. The two K x-rays are separated by about 430 keV. The values for the peak areas of the two Sm $K\alpha$ x-rays was usually within 10 % of the theoretical values of Schofield [3]. On some occasions when the overall background was quite low, RACE gave peak areas for the $K\alpha$ components of Pr and Nd. Figure V.1 shows the K x-ray spectrum of

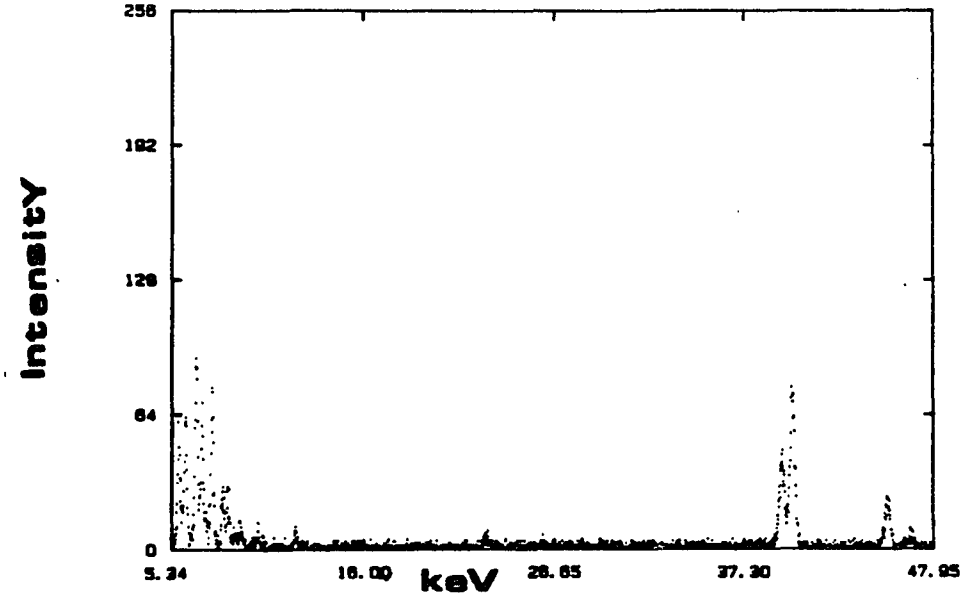

Figure V.1 Sm K x-rays from 2.0 MeV proton bombardment

Sm.

The photon detector was well insulated both electrically and mechanically to avoid losses in energy resolution due to either microphonics or grounding problems. The energy efficiency calibration of this HPGe detector was discusssed in Chapter IV.

The energy resolution of the detector was checked by using the Fe K x-rays from Co^{57}, Se K x-rays produced in-beam by 2.0 MeV H+ bombardment, Gd K x-rays emitted from NBS 4225B "mixed source" and from the 86.5 keV and 123.14 keV γ-rays emitted from the same NBS mixed calibration source. The resolution was typically 190 ev at 7.04 keV (Fe Kβ x-rays), 210 ev at 11.24 keV (Se Kα x-rays), 530 ev at 48.71 keV (Gd Kβ x-rays), 625 ev at 86.5 keV and 790 ev at 123.14 keV (both γ-rays from NBS 4225B).

Counting rates were never larger than 500 counts/sec and on occasion as low as 25 counts/sec. This situation resulted in very low deadtime losses, typically between 1 - 5 %. RACE automatically made deadtime corrections to the analysed peak areas which made it easier to calculate corrections directly from the data.

A. Methods of Normalization

Three methods of normalization were employed in the measurements of of σ_{KI}. These methods were:

a.) The normalization to the yield of Rutherford backscattered projectiles. This method has been extensively used in both nuclear and atomic physics.

b.) The previously mentioned method of normalizing to the yield of CE γ-rays. While the RBS method is generally applicable to all elements regardless of their nuclear properties; this method is valid only for those elements that have at least some highly deformed nuclides.

c.) The third method was developed for the first time in this study. It involves using the yield of the $L\gamma_{1,5}$ x-rays of the element whose K-Shell cross section is being measured. In order not to overwhelm the photon detector with the more intense lower energy L x-rays, some sort of filter must be placed in front of the detector so that only the desired $L\gamma_{1,5}$ lines reach the active volume of the detector. The $L\gamma_{1,5}$ lines must also be intense enough so that good counting statistics are obtained despite the use of a filter.

A more complete description of each method will now be given.

i.) RBS Normalization

The method of normalizing to the yield of Rutherford scattered projectiles is usually the most straightforward and general method available. The method requires accurately measuring the yield of the back-scattered projectiles and depends on the validity of the differential Rutherford cross section at that bombarding energy and scattering angle (center of mass). The value of σ_{KI} can then be extracted from the experimentally determined values of x-ray and particle yields using:

$$\sigma_{KI} = 4\pi \frac{Y(Kx)\Omega_p}{\omega_k \epsilon_k Y(p)} \left(\frac{d\sigma}{d\Omega}\right)_{ruth} \qquad (1)$$

where Y(K) is the yield of K x-rays produced at a specific bombarding energy, Ω_p is the solid angle subtended by the particle detector, ω_K is the K-Shell fluorescence yield of the element studied, Y(P) is the yield of backscattered projectiles, ε_{abs} is the absolute effiency of the photon detector for those particular K x-rays and $(d\sigma/d\Omega)_{ruth}$ is the differential Rutherford cross section

There are some restrictions and limitations to the application of this method that should be addressed. These are:

a.) Deviations From Pure Coulomb Scattering

Deviations from purely Coulomb scattering can occur at backward angles for bombarding energies (lab) either near or above the Coulomb barriers (the differential elastic cross section can change dramatically from pure Coulomb scattering). While it has been proposed [4] that deviations from pure Coulomb scattering due to the effects of the nuclear potential do not substanially alter the probability for K-Shell ionization, it does make it a difference in terms of the experimental results if only RBS normalization is used.

Corrections for the inclusion of nuclear effects can be made by using the proper optical-model [5] or distorted wave Born approximation [6] (DWBA), calculations. These calculations are far from simple and can be very time-consuming. Also if one is dealing with an element like Sm which has 7 naturally ocurring isotopes, most of which have very different nuclear properties, an interpretation of the experimentally obtained particle spectra could be nearly impossible.

Even bypassing the computational problems, using the previously established elastic scattering cross sections would not be very helpful in practical terms as long as a multiisotopic element was being studied.

b.) Geometric Experimental Constraints

The geometry of the experiment also plays a role in limiting on occasion the usefulness of the RBS method. The reason for this is that in a very "tight" experimental arrangement where the target holder is placed very close to the particle detector (as in this work) very large particle counting rates can result if slow, heavy projectiles are used to measure small cross sections. A situation like this occured during one or our experiments.

We allowed 700 na of 1.6 MeV He+ to strike a thin Sm^{154} target in our scattering chamber. Due to the relativley large solid angle of the particle detector, large current and the value of $(d\sigma/d\Omega)_{ruth}$, deadtime losses of nearly 93% were observed for the particle detector. Needless to say the energy resolution of the particle spectrum was not particularly good under these conditions.

This amount of current was needed because of the small cross section values for these energies. In 45 minutes of bombarding, not one Sm K x-ray nor a 82 keV γ-ray was observed. Obviously if He+ projectiles of these energies were to be used, RBS normalization would not be acceptable.

We have also observed the effects on the yield of backscattered projectiles of a nuclear elastic scattering resonance although not at the energies that would affect the scattering behavior of the elements whose

cross sections were measured. It would require proton energies of nearly 9.0 MeV before nuclear effects would become significant.

However, the effects of a nuclear scattering resonance can be seen in the particle spectra from the $C^{12}(p,p)C^{12}$ elastic resonance at 1.73 MeV. Figures V.2 a,b,c shows the change in the relative peak height of the C backing to the Sm deposited in front of it. The spectra were taken at 1.6, 1.8 and 2.0 MeV and the scattering angle is 150 degrees (lab). This would not be easily observed if C^{12} was not the dominant isotope and the 1.73 Mev resonance was not well isolated. Thus in multisotopic targets this phenomenon is a potential source of error.

Another restriction on the use of the RBS method is if one wishes to measure σ_{KI} of an element(s) in a chemical compound which has two or more elements so close together in mass that the RBS peaks from each could not be fully resolved. Unless one knew for certain the relative amounts of each element present, Y(p) could not be used for normalization purposes. Similar circumstances may arise if the target surface is very rough or non-homogeneous.

Finally, there is the situation where a chamber designed for either PIXE or micro-PIXE may be suitable for cross section measurements but may not be able to accomodate a particle detector inside. This could be true for a chamber designed for work with a He at atmosphere for instance.

ii.) Normalization to the Yield of CE Gamma-Rays

A number of elements that are in the region of strong permanent nuclear deformation have had their values of σ_{KI} determined by normalizing the

yield of K x-rays to the yield of γ-rays produced via Coulomb excitation [7,8]. The value of σ_{KI} can be found through the use of (2):

$$\sigma_{KI} = \frac{Y(Kx)\varepsilon_\gamma \sigma_{ce}}{Y(\gamma)\varepsilon_x p(1+\alpha_t)} \qquad (2)$$

where σ_{KI} is the cross section for Coulomb excitation, ε_γ is the effiency of the photon detector for the CE gamma-rays, α_t is the value of the total internal conversion coefficient for the individual levels that are populated and p is the isotopic abundance for the particular nuclide that is being Coulomb excited.

The conditions that must be met for this method to produce good results are:

a.) There must be a significant probability for the Coulomb excitation process to occur so that CE γ-ray yields are large enough to be measured reliably and accurately. This limits the application of the method to only those elements which contain strongly deformed nuclides such as the rare-earths. Indeed, all of the work done so far using this method has been done for the elements of the lanthanide and actinide groups.

b.) Bombarding energies must be kept below the Coulomb barrier to insure that the excitation is strictly electromagnetic.

c.) The values of σ_{ce} may be obtained either from calculations or by measuring the σ_{ce} values oneself. If the values of σ_{ce} are to be measured experimentally, then another means of normalization must be used such as RBS or charge normalization. We have measured σ_{ce} for Sm^{154} over the range of proton energies used here by employing the RBS normalization technique. The results are shown in Table V.1.

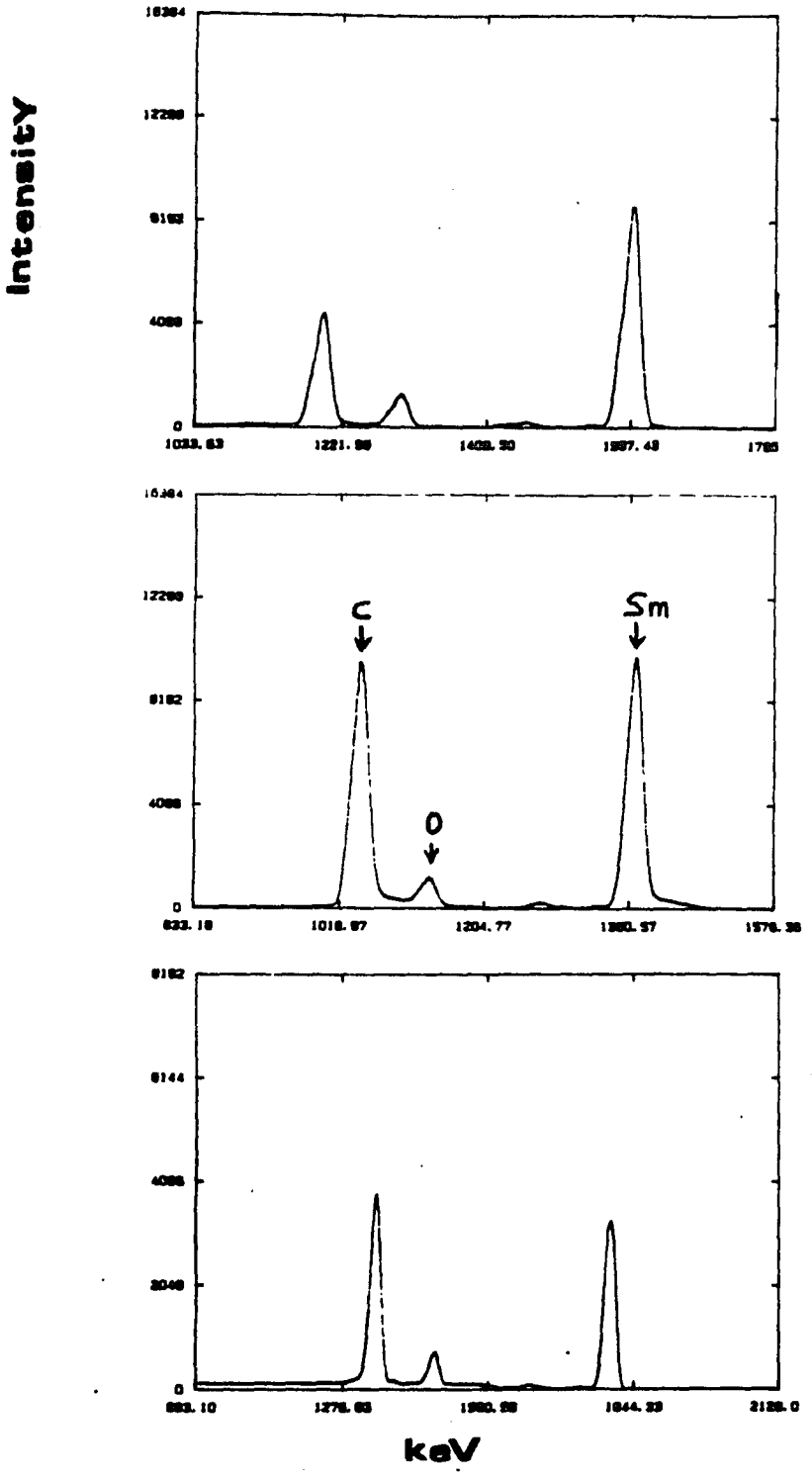

Figure V.2 a,b,c Particle spectra at 1.6 MeV, 1.8 MeV and 2.0 MeV showing the effect of the C12(p,p)C12 elastic scattering resonance on the relative yield of H^{+}'s scattered from thin C backing of a Sm target

The calculation of σ_{ce} values is not particularly difficult following the Bohr-Winther SCA ansatz [9] (see Chapter II), complications can arise even when low energy protons are used. The validity of using a first-order calculation may fail and then a more complicated approach is needed to calculate the value of σ_{ce}.

iii.) Normalization to the Yield of L x-rays

This method was developed for the first time here and is similar to the CE method in that only photons need to be measured. The values of σ_{KI} can be extracted from the relative yields of the two x-rays. The two basic assumptions of the method are:

1) Accurate values of $\sigma_{LY_{1,5}}$ can be obtained from existing literature values, through the use of the L subshell ionization probabilites as predicted by ECPSSR or RSCA or by measuring them for the elements one wishes to apply the method to.

We have chosen to measure the values of $\sigma_{LY_{1,5}}$ for the energies and the elements of this study. The results are shown in Table V.2. The overall trend is that our values tend to be lower than the values predicted by ECPSSR for the lowest proton energies but higher as the energy is raised. Typically our cross sections are 10-15 % higher than predicted by ECPSSR which is consistent with other experimental values [10].

By using cross sections that were determined by the same experimenters who are doing the K-Shell work, some accuracy and consistency can be introduced into the normalization method.

2) The absolute yields of the $L\gamma_{1,5}$ x-rays can be obtained if the transmission factor through the filters can be reliably calculated. We have found that the most reliable way to do this is to weigh the metal foil before using so that the thickness is known very well. This has proven to give more accurate results than relying only on the thickness values provided by the manufacturer. In fact, small changes in the thickness used in the calculation of the transmission factor, T, introduces a greater uncertainty for the value of σ_{KI} than does any of the other parameters.

This is basically due to the large sensitivity in the values of $T_{l\gamma}$ when a filter is used which has a very high value of μ_{abs} for the L x-ray energies involved. We have found that the most efficient way to prevent the more intense L x-rays from reaching the detector is to use a filter whose K_{abs} edge is very close to the $L\alpha_{1,2}$ x-ray energy (or in the case of Ta, $L\beta_{1,2}$ x-rays).

In that case, the filter acts like a "critical absorber" and attenuation factors for the x-rays very close in energy to the K_{abs} of the filter are extremely high. For instance in the case of Sm $L\alpha_{1,2}$ x-rays, attenuation

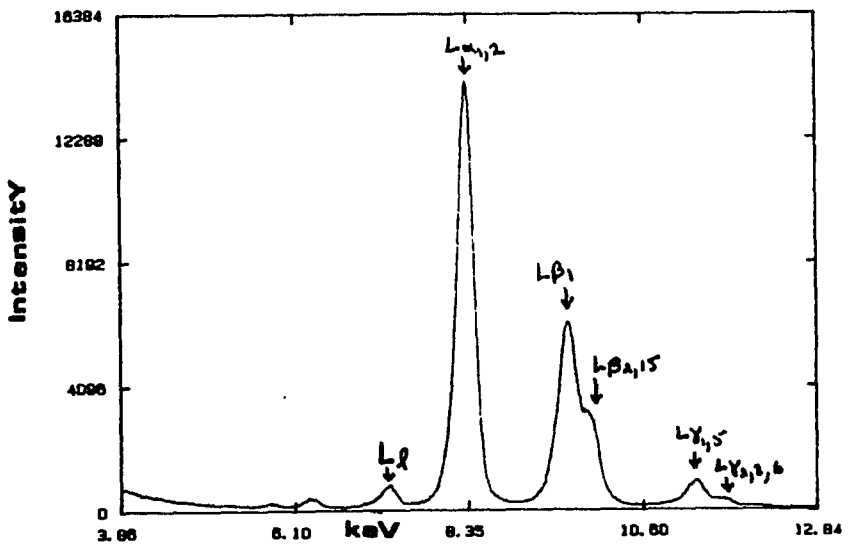

Figure V.3a W L x-rays from 1.6 MeV proton bombardment

factors of nearly 1 x 10^{-5} can be reached.

The $L\gamma_{1,5}$ x-rays being further removed from the K_{abs} of the filter are far less attenuated and reach the detector in sufficient intensity to give

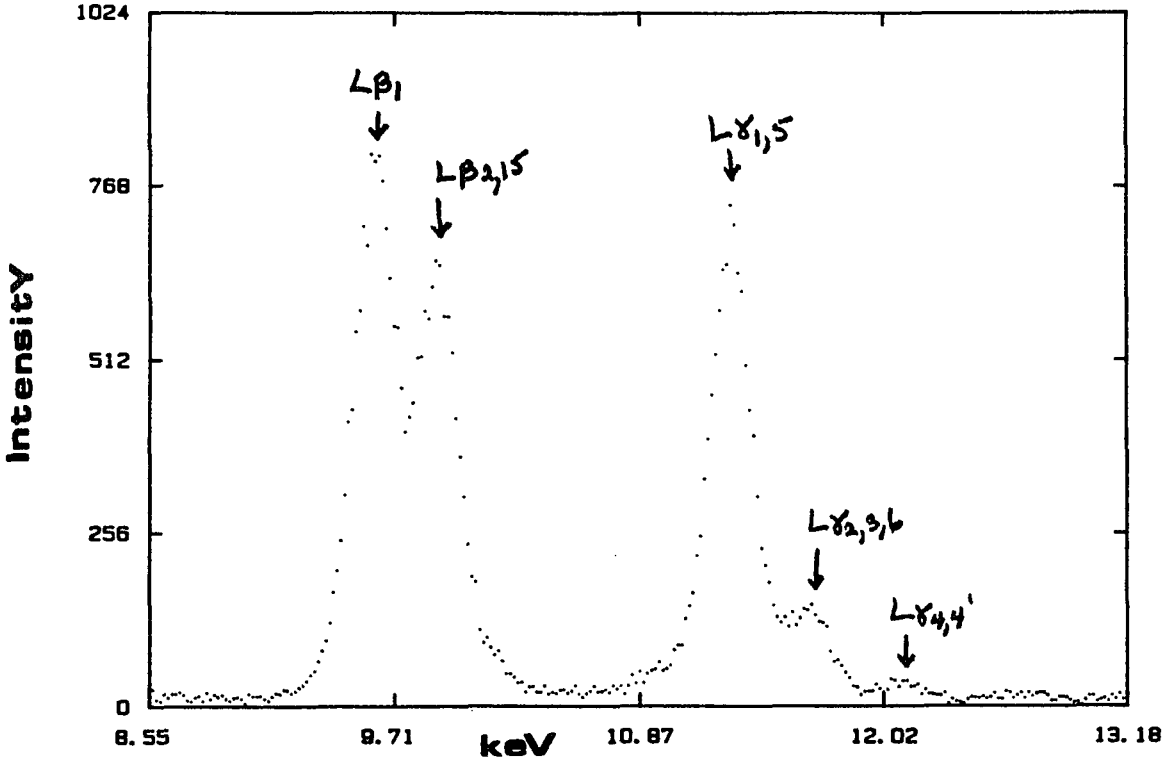

Figure V.3b W L x-ray spectra showing the effects of a Ni critical absorber

good counting statistics. An example of the kind of dramatic changes in the relative intensities of the L x-rays of W when a critical filter of Ni is used is shown in Figure V.3 a,b.

The value of σ_{KI} can be found by using (3)

$$\sigma_{KI} = \frac{Y(Kx)T_1\sigma_1\varepsilon_1}{Y(L\gamma)\varepsilon_k} \quad (3)$$

where Y(Lx) is the yield of the $LY_{1,s}$ x-rays, ε_l is the efficiency of the detector for the $LY_{1,s}$ x-rays, σ_l is the cross section for $LY_{1,s}$ x-ray production and T_l is the transmission factor for the $LY_{1,s}$ x-rays.

This method has all of the advantages of a method that relies on measuring the relative yields of photons as the does the CE method but does not have as many limitations and disadvantages. These limitations of the γ-ray method are:

a.) It is limited only to those elements which have permanent nuclear deformation.

b.) The γ-ray yields rapidly decrease relative to the K x-ray yields as the beam energy is raised especially if protons are used. This is because σ_{ce} does not rise nearly as dramatically as the direct atomic collision channel as the energy is raised.

Normalization to the $LY_{1,s}$ cross section does have some practical limitations in terms of which filters may be used. Some of the more desirable filters for particular elements are not readily commercially available in the form of foils (eg. Mn or Co). Usually it is most convient to use a metal foil as the critical filter, by simply placing the foil over the face of the detector.

An important consideration in the application of this method is that μ_{abs} is smoothly varying as E_γ increases past the K_{abs} edge. This is not generally true for the 3d elements in the immediate vicinity of the K edge. The variation in μ_{abs} for Ti, which was used as a critical absorber for the Lα x-rays of Pr and Nd, and that of Ni, which was used as a critical absorber for Ta and W, is shown in Figures V.4 a,b.

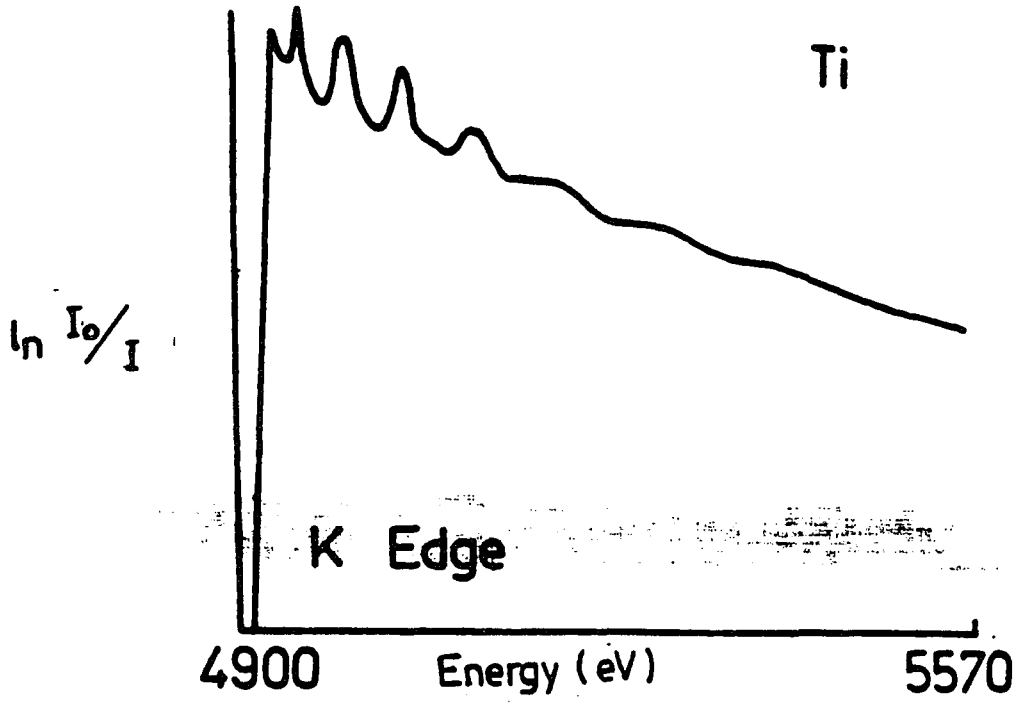

Figure V.4a Variation in the absorption coeffiecent of Ti as a function of photon energy taken from ref. 11

The oscillatory behavior near the K-Shell binding energy is due to the EXAFS [11] or extended x-ray absorption fine structure behavior of these 3d transition elements. Fortunately, in the case of normalization, the behavior of μ_{abs} has become quite predictable by the time the $LY_{1,5}$ x-ray energies are reached. This means that the value of $T_{L\gamma}$ can be calculated from the thickness of the foil and the value of μ_{abs} at the appropriate energy.The value of μ_{abs} has at its origin the value of $\sigma\gamma$ at that photon energy.

For the elements studied here, foil thicknesses range from 12.45 - 24.95 mg/cm^2, which resulted in $T_{l\gamma}$'s of 1 - 3.5 x 10^{-2}. The values of μ_{abs}

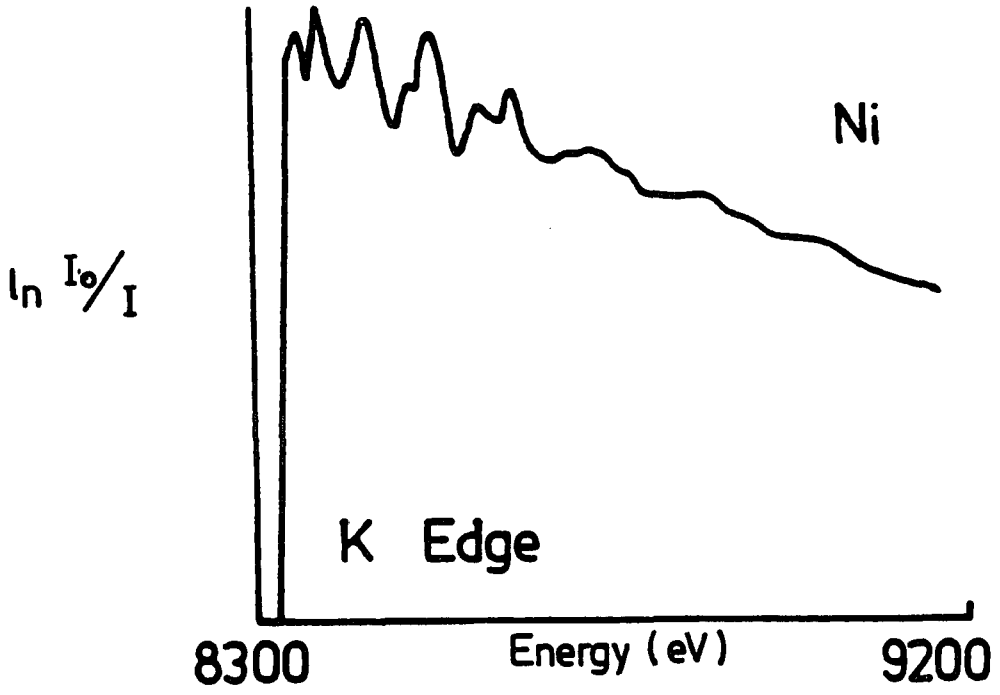

Figure V.4b Variation in the absorption coeffiecent of Ni as a function of photon energy taken from ref.11

for the indivdual $LY_{1,5}$ lines were taken from the compiliation of Montenegro, et al. [12]. The values of μ_{abs} for the $LY_{1,5}$ energies and the thicknesses of the foils used are shown in Table V.3.

It has come to our attention recently that a critical absorber of Zn has been used to separate the $L\alpha_1$ from the $L\alpha_2$ lines of Au [13] produced by 500 keV proton bombardment. This was done not in a normalization method but in order to separate the two $L\alpha$ lines and to determine the M1-E2 mixing ratio for some of the L_3 subshell transitions.

2. Results

A. Comparison between the Results of the Different Normalization Methods

In Tables V.4 a - l , we show the results obtained with the various methods of normalization. For the CE normalization method we have only results from Sm^{154} because while our computer analysis code identified the 82 keV γ-ray of Sm^{154}, RACE was unable to quantify the other low energy γ-rays from Sm^{152}(found in the natural Sm target), Tm, Ta and W.

Although the 110 keV γ-ray of Tm^{169} could usually be made out as appearing in the recorded spectrum (as displayed on the MCA) as could occasionally the 100, 110 and 122 keV γ-rays of W^{182}, W^{184} and W^{186} respectively, intensities of these peaks relative to the overall background was very low. The uncertainties in peak areas (determined using the ORTEC spectral analysis program) were so large we felt it unwise to use the peak areas for these γ-rays to obtain meaniful values of σ_{KI}. The 136 keV γ-ray of Ta^{181} and the 122 keV γ-ray of Sm^{152} were never observed at all. Even in the case of the 82 keV γ-rays of Sm^{154}, the yield of γ-rays was in the range of 0.02 to 1 per μ C over the range of proton energies used. The 82 kev γ-ray as well as the Sm K x-rays are shown in Figure V.5 and the Tm Kx-rays as well as a peak which is probably the 110 keV γ-ray is shown in Figure V.6. The energy region where the γ-rays from natural W are expected to appear is shown in Figure V.7

The values of σ_{KI} have been determined using the CE γ-ray method of normalization of Sm (Sm^{154} was used in that study as well), Gd, Ho, Tm, W

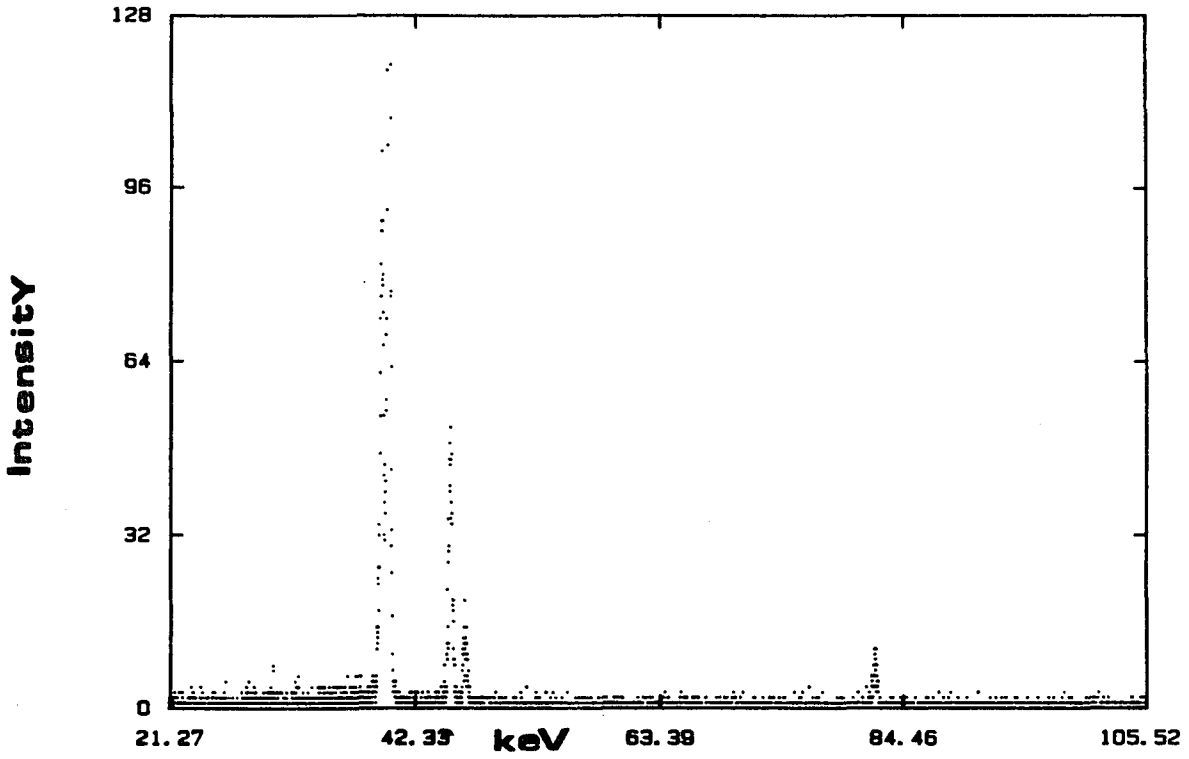

Figure V.5 Sm154 Kx-rays and 82 keV gamma-ray produced by 1.0 MeV proton bombardment

and Au but thick targets were always used in these studies. Thicknesses in the range of 1 - 2 mg/cm^2. Aside from the factor of target thickness, there are three other factors which influence the absolute yield of CE γ-rays. These are:

a.) Internal conversion not just into the K-Shell, but the overall conversion into the higher atomic shells as well such as L_1,L_2,L_3 etc. For instance the 100 keV, 2^+ level of W^{182} is nearly 75% converted. This means that automatically the yield of 100 keV γ-rays is lessened by a factor of almost 3, from a pure W^{182} target (which can be quite costly to prepare) regardless of any techniques the experimenter may use to improve the qual-

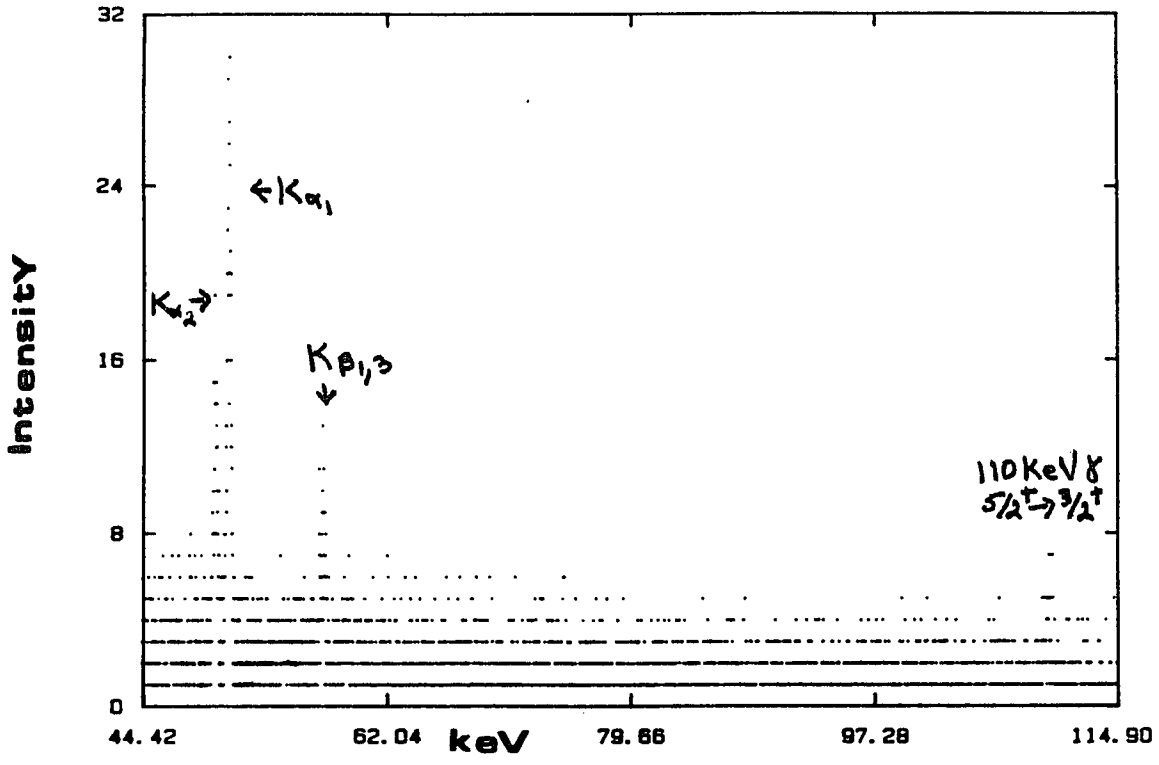

Figure V.6 Tm K x-rays and indication of 110 KeV gamma-ray produced with 1.4 MeV protons

ity of his results.

b.) Multisotopic targets lower the overall intensity of one particular gamma-ray. Natural W for instance, contains three isotopes which are nearly equally abundant. This fact also lowers the intensity of any one specific gamma-ray that is produced from CE; the probability of Coulomb exciting the three major even isotopes of W is roughly equivalent.

c.) The anisotropic emission of the CE gammas, especially at the lowest bombarding energies, makes the placement of the photon detector an important consideration in the design of the experiment if gamma-ray intensity is to be maximized. This calls for placing the detector at either 55° or

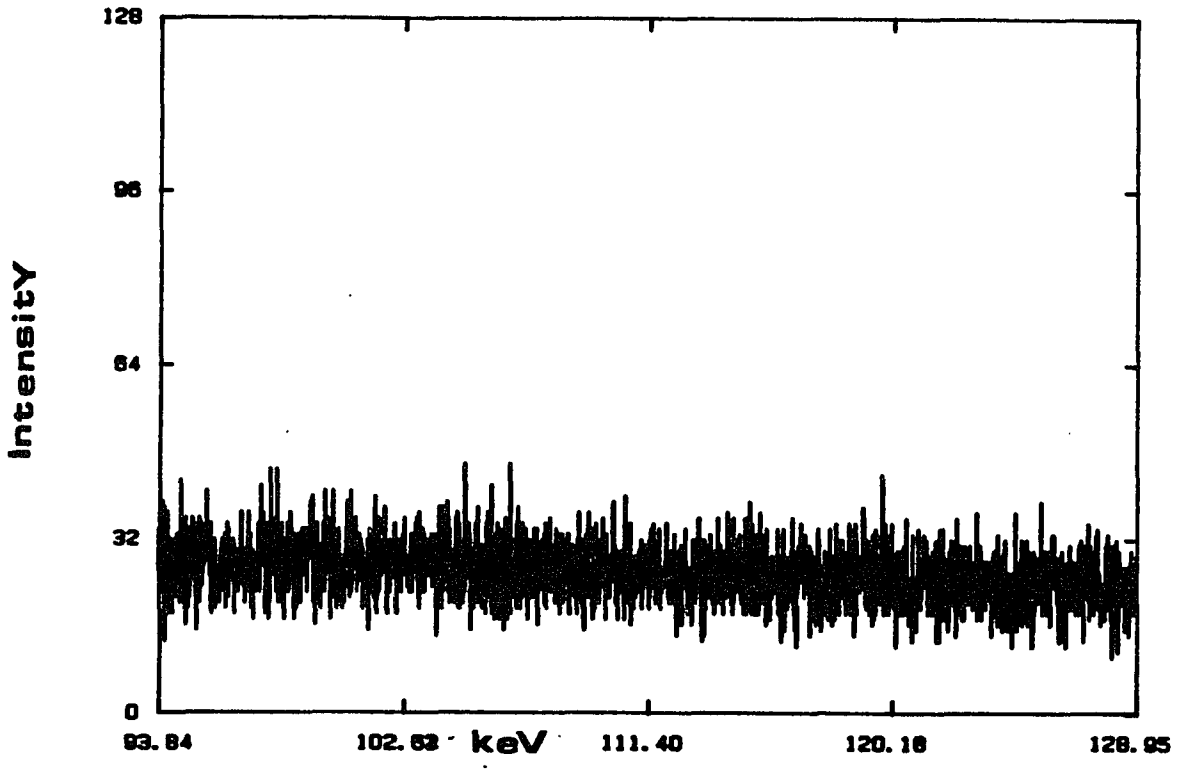

Figure V.7 W photon spectra in the energy region of 95 - 125 keV taken with 2.8 MeV protons

125° with respect to the beam axis in order to minimize the effects of anisotropic emission of gammas.

In our work, unfortunately, the constraints of the geometry of the chamber forced us to place the photon detector at 90° with respect to the beam axis. This maximizes the anisotropy for reasons that will be explored in more quantitative detail a little later on in this section.

The $LY_{1,5}$ normalization method suffers from none of these problems. The emission of $LY_{1,5}$ x-rays of the same energy and with the same probability is independent of the nuclear properties and therefore of the isotopic composition of any element. All of the atoms in the target emit $LY_{1,5}$

x-rays with the same energy and with equal probability.

In addition, the $LY_{1,5}$ x-rays are isotropic (to very high degree of accuracy) throughout the entire range of bombarding energies. No special consideration has to be given to the placement of the detector relative to the beam axis. This allows an experimenter to be more flexible in using the scattering chamber.

If one choosesto make measurements of σ_{KI} with an isotope that needed no corrections to its K x-ray yield such as a spherical one like Sm^{150}, the $LY_{1,5}$ method could be used while the CE method would be inappropriate. For the type of projectiles used in this study, the maximum amount of K x-rays from IC-CE was never greater than 35 - 40 %; there can be instances where the total yield from IC-CE could easily attain the values of 90 - 95% of the total K x-ray yield. Given the degree of uncertainty in the quantities needed to make the corrections for CE, such as the values of B(E2), α_K, etc., it may be worthwhile to have an option which eliminates the CE contribution to the total K x-ray yield.

The yields of the $LY_{1,5}$ x-rays through the various filters that were used ranged from 2 - 21 $LY_{1,5}$ x-rays per uC. This represents a relative increase in the total peak areas of between 10 - 300 as compared to the CE γ-ray yields.

The combinations of filters used with elements were: Pr,Nd/Ti filter, Sm/V filter, Tm/Fe filter and Ta,W/Ni filter. For all of these combinations the filter was chosen for the proximity of its K edge to the $L\alpha_{1,2}$ x-ray of an element studied (for Ta it was $L\beta$, Co would have been the ideal choice but it is difficult and expensive to acquire as a foil).

B. Auxillary Data Needed to Calculate K-Shell Cross Section values from the Experimental Data

In addition to the the experimentally determined yield of photons and backscattered projectiles, there are many other factors that need to be calculated accurately in order to arrive at values of σ_{KI} that are reasonable. These factors range from the basic atomic and nuclear data, such as ω_K, $K\alpha_1/K\alpha_2$ etc., to trivial calculations like the value of $(d\sigma/d\Omega)_{ruth}$, to some fairly complicated calculations such as the anisotropy of the CE γ-rays. We will now list the source of the more significant factors used.

i.) The basic atomic and nuclear data were taken from the literature sources and include: values of ω_K from Krause [14] K x-ray branching ratios from Schofield [15], values of B(E2), the reduced transition matrix element for E2 transitions needed to calculate σ_{ce} from Raman [16] and the values of α_K and α_t from Rosel [17].

ii.) The last two factors are essential for removing the K-Shell internal conversion contribution from the total K x-ray yield for the deformed nuclides. For all of the deformed nuclides of this study, which includes all of the elements studied except for Pr, Nd, Sm^{150} and all of the Sm isotopes of natural Sm except for Sm^{152} and Sm^{154}, corrections to the total K x-ray yield must be made by subtracting the calculated amount of K x-rays produced from IC-CE.

The direct comparison between Sm^{150} and Sm^{154} affords the opportunity to examine any discrepancy between the calculated contribution from IC-CE and the observed differences in the total K x-ray yields of the two nuc-

lides. It has been generally assumed that for the type of E2 transition that can be Coulomb excited, the theoretical values of α_K and α_t are accurate to within 3 - 5 %.

One source of inaccuracy that can not be dealt with on a theoretical basis is the value of the mixing ratio, δ^2, for a mixed M1/E2 transition that is very common for odd-A nuclides. This concern is relevant here because two of the elements studied are both deformed nuclides and odd-A, Tm^{169} and Ta^{181}. Both the $5/2^+ \rightarrow 3/2^+$, 110 keV transition in Tm^{169} and the $9/2^+ \rightarrow 7/2^+$, 136 keV transition in Ta^{181} are this type of transition.

The values of δ^2 that were used in this work in order to determine the value of α_K were in the case of Tm^{169} taken from Verma [18] and for Ta^{181}, from Avignone [19]. The other odd-A deformed nuclide that is present in the target elements studied is W^{183}. However, the mixed M1/E2 53.5 keV Y-ray which is the crossover transistion between the second and the first excited states of W^{183} which can be reached via CE is too low in energy to be K-Shell converted. Therefore, from a practical point of view the value of δ^2 for this transistion is not of concern to us.

iii.) The values of σ_{ce} for nearly all of the deformed nuclides studied here could be calculated using the Bohr-Winther first-order SCA method. However, for both Tm^{169} and W^{183} that approach does not provide accurate values of σ_{ce}.

This is due to the fact that the excitation probabilities for the first and second excited states of Tm^{169} and W^{183} can not be considered separately as was the case for the even-A deformed isotopes of Sm and W. This coupling of probabilities for both nuclides is caused by both the relatively low energies of the first excited states, 8.4 keV for the $3/2^+$ state of Tm^{169} and 46.5 keV for the $1/2^-$ state of W^{183} and the degree of coupling

between the first and second excited states. Therefore, in order to calculate the values of σ_{ce} for the second excited states of both Tm^{169} and W^{183} (these states are our major concerns since the first excited states of both nuclides are too low in energy to be K-Shell converted) a coupled-channels approach was needed.

The strength of the excitation coupling is given by the value of $\chi_{i\rightarrow f}$, which indicates the degree of coupling that is taking place during the excitation process at a particular bombarding energy. The value of χ, in our case we can refer to $\chi_{2,3}$,depends on the projectile's charge and velocity, the value of B(E2) for the two states and on Q_0, the static quadrupole moment of that particular nuclide. The larger, slower projectiles are capable of producing more coupling between the excited states during the excitation process.

Therefore, it is a little bit of surprise to find out that for H^+ the degree of coupling is sufficient in the case of these two nuclides that first-order SCA does not work. For instance, at 1 MeV H^+ velocities, the value of $\chi_{2,3}$ is 0.7423 for Tm^{169} and 0.4938 for W^{183}. The condition for first-order perturbation to be correct is $\chi << 1$. Obviously, that is not true in these cases.

The values of σ_{ce} and more importantly for our purposes, the contributions from IC-CE as a function of projectile energy used for the nuclides Tm^{169} and W^{183} were obtained from the DeBoer-Winther [20] coupled-channels code. The values of σ_{ce} were supplied to us by I.Y.Lee of Oak Ridge National Laboratory.

The use of the coupled-channels results were very important in arriving at the proper values of σ_{KI} for Tm^{169} at the lowest H^+ energies. This is because of the familar scenario where the relative IC-CE contribution to the K x-ray yield is maximized at the lowest beam energies. If first-order

calculations were used for the σ_{ce} values instead of the coupled-channels approach then the IC-CE contribution would have been overestimated by roughly 30 % due to the nearly doubling of the calculated σ_{ce}. We assume that the accepted valued of δ^2 (and therefore the accepted value of α_K) for the 110 keV Y-ray is valid.

As the H^+ velocity is raised, the value of $\chi_{2,3}$ drops, until by 3.0 MeV the value of $\chi_{2,3}$ has reached 0.1747 or nearly within the limits of first-order pertubation. It should be kept in mind that at these higher velocities the IC-CE contribution has dropped to approximately 5 % in the case of Tm^{169}.

In regard to the W^{183} situation, the importance of using a coupled-channels approach to arrive at the values of σ_{ce} has been generally overlooked by most workers in the field of inner-shell ionization who have measured natural W σ_{KI} values. Perhaps a reason is that W^{183} is only 14.3 % naturally abundant so that its σ_{ce} behavior has been overlooked. However, it has come to our attention via our interest in the the coupled channels approach that W^{183} would make an interesting target that would serve nearly the same purpose as using targets of Nd^{142},Sm^{150} and Eu^{151} have in that the IC-CE contribution could be significantly lowered. The relevance of this approach in reducing the IC-CE contribution and thereby reducing some uncertainites of the measured σ_{KI} values for W will be discussed more thoroughly later in this Chapter.

iv.) The values of $\sigma_{LY_{1,2,3}}$ were taken from our own experimental data as was stated previously. The σ_{LI} of all of the elements studies here were measured using thin targets and employing the RBS method of normalization. Much lower beam curents were used in obtaining the L x-ray spectra with much shorter running times reflecting the much larger values of σ_{LI} than for σ_{KI}. No critical filters were used in these experiments.

The values of $\sigma LY_{1,5}$ were measured ourselves because of our concern over the underestimate of $\sigma LY_{1,5}$ by theories such as ECPSSR and an attempt

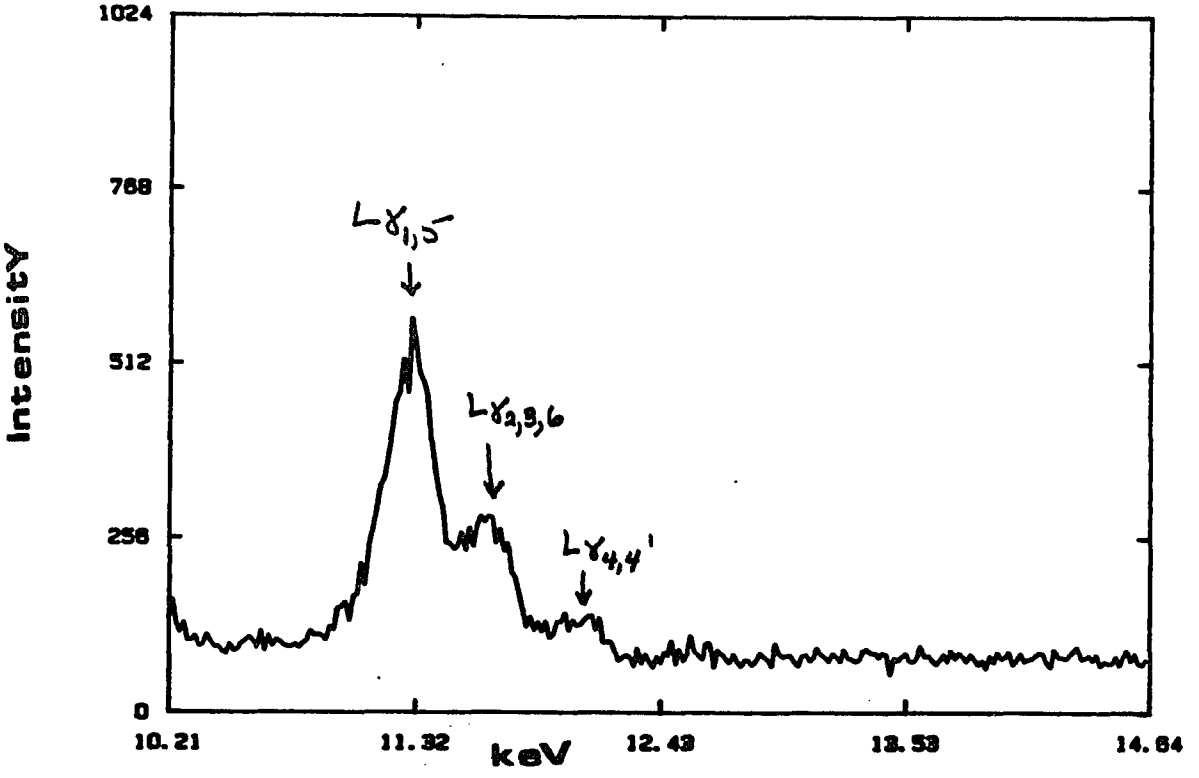

Figure V.8 W L Gamma x-rays produced by 2.8 MeV protons

to be somewhat selfconsistent in terms of how we handled the L x-ray peaks.

The two main causes of inaccuracy in obtaining the $\sigma LY_{1,5}$'s ourselves would be uncertainties in the value of εl_Y at the particular x-ray energy in question and the ability of RACE to deconvolute the LY multiplets of $LY_{1,5}$ $LY_{2,3,6}$ and $LY_{4,4'}$. An example of the LY x-rays of W produced by 2.8 MeV H^+ is shown in Figure V.8.

We believe that the values of εl_Y for the $LY_{1,5}$ x-rays used in our normalization method are accurate to within 1-2 %. The ability of RACE to

reproduce the relative LY intensities at a given bombarding energy is typically around 5%. The values of the $LY_{1,5}$ cross sections for the elements studied are given in Table V.2. Table V.2a shows the comparison between our experimental values for W and the predicted values of ECPSSR.

v.) The values of $T_{1\gamma}$ are very sensitive to the thickness of the foil used and the values of μ_{abs} obtained from the literature. We assume that at the energies of the $LY_{1,5}$ x-rays of interest here that μ_{abs} is well behaved and devoid of any fine stucture. With that in mind the most important factor in determining the value of $T_{1\gamma}$ is the measured thickness of the foils. The values of the foil thicknesses used as well as the μ_{abs} for the filters are given in Table V.3.

vi.) One of our intial concerns in using the CE γ-ray method of normalization was the loss in intensity of the gammas due to the anisotropy of the CE γ-rays which was compounded by our detector being placed at 90° with respect to the beam. The importance of accurately accounting for losses in the yield of γ-rays due to anisotropic emission as well as the importance of using a coupled-channels approach in calculating the σ_{ce} for some cases has often been overlooked in experiments designed to measure σ_{KI} [21].

The anisotropy for a given gamma produced from CE is defined by (4):

$$W(\theta) = 1 + G_2 a_2 A_2 P_2(\cos\theta) + G_4 a_4 A_4 P_4(\cos\theta) \quad (4)$$

where $W(\theta)$ is the degree of anisotropy, G_2 and G_4 are the finite solid angle attenuation coefficents, a_2 and a_4 are the particle parameters for

Coulomb excitaion, A_2 and A_4 are the gamma-ray angular correlation coefficients and $P_2(\cos\theta)$ and $P_4(\cos\theta)$ are the associated Legendre polynomials of order 2 and 4 respectively.

At 90°, both $P_2(\cos\theta)$ and $P_4(\cos\theta)$ have their maximum(minimum) values of -0.500 and 0.375 respectively. This has the effect of enhancing the anisotropy of the γ-rays. In contrast, placement of the photon detector at 55° or 125° serves to minimize the anisotropy because the $P_2(\cos\theta)$ term goes to zero. Since the a_4A_4 terms are usually small in comparison wtih the a_2A_2 terms, $W(\theta)$ approaches the values of unity at these angles. For a spin sequence of $0^+ \rightarrow 2^+ \rightarrow 0^+$, the values of A_2 and A_4 are fixed at 0.3571 and 1.143. This spin sequence is the one typical for E2 transitions of even-even nuclides in terms of cascades produced by low energy Coulomb excitation.

For our counting geometry, we calculate values of $W(\theta)$ as small as 0.78 for the 122 keV gammas produced from 1.0 MeV proton bombardment on W^{186}. This includes the quantum mechanical effects on the values of a_2 and a_4 [22]. Since gamma yields from only Sm^{154} were used in our calculations the above illustration is merely academic with regard to our results. The values of $W(\theta)$ for the 82 keV gammas of Sm^{154} ranged from 0.84 to 0.96, with the lower values pertaining to the lower proton energies. Again as for the W^{186} calculation, quantum mechanical corrections were introduced. These values of $W(\theta)$ were used in the σ_{KI} values obtained using the CE γ-ray method of normalization. In the case of the 110 keV gammas of Tm^{169} the values of $W(\theta)$ had to be calculated from the values of the statistical tensors obtained at each bombarding energy from the coupled-channels cal-

culations.

All of this was done not only to obtain the most accurate values of the gamma yields possible but in the case of all of the other nuclides besides Sm^{154} to insure that the low γ-ray yields were not in large part due to the 90 degree orientation of the photon detector. The calculations involving the statistical tensors from Tm^{169} excitation indicated that the 110 keV gammas were essentially isotropic. As for the 136 keV gammas of Ta^{181} which were not ever observed, the high spin sequence involved ($7/2^+ \rightarrow 9/2^+ \rightarrow 7/2^+$) means that these γ-rays are essentially isotropic. For both Tm and Ta, the mixing ratio enters into the calculations of $W(\theta)$ as they did with the values of α_K since the values of A_2 and A_4 are dependent on δ^2 as well as the spin sequence. In fact, the largest value of $W(\theta)$ for Tm which is obtained at 1.0 MeV bombarding energy, is 0.96. As the proton energy is raised the value of $W(\theta)$ approaches unity indicating that the gammas are isotropic.

Finally, in regards to the values of $W(\theta)$, one has to also consider the values of G_2 and G_4 for the soild angle subtended by the photon detector. These values can be extrapolated from the tables of Avignone [23]. In the case of our detector geometry both G_2 and G_4 are essentially unity due to the small solid angle subtended. Counting losses as large as 40% can be encountered because of the effects of finite solid angle attenuation. These effects are quite often neglected by experimenters performing σ_{KI} measurements [21].

vi.) Due to the smallness of the values of the Sommerfeld parameter, η, (6 - 11), for the bombarding conditions used here, there was some concern over the valdity of the SCA approach in calculating σ_{Ce} and $W(\theta)$. It

is generally accepted that η should be large compared to unity in order that the SCA be strictly valid. Usually a value of 10 is considered adequate.

It was not immediately obvious whether the SCA would provide accurate results. However a closer look at the CE process reveals that the corrections to the total value of σ_{ce} are quite small, on the order of η^{-2}, whereas the correction to both a_2 and a_4 are on the order of η^{-1} [24]. For second-order probabilities the corrections to the total cross section are on the order of η^{-1}. Therefore, quantum mechanical corrections were applied to values of $W(\theta)$ of the 82 keV γ-rays of Sm^{154} and the total cross sections of Tm^{169}.

C. Discussion of Cross Section Results with the Three Normalization Methods

The results of the values of σ_{KI} are presented in Tables V. a - 1. What we find is that the RBS and $LY_{1,5}$ methods agree with each other over the full range of proton energies covered to within the following limits: Pr ±12.5%, Nd ±12%, Sm(nat) ±16.1%, Sm^{150} ±10.5%, Sm^{154} ±0.2%, Tm ±11.7%, Ta ±9.3% and W ±19.8%. In comparison, the Sm^{154} CE γ-ray method gave agreement with the RBS method to ±0.5% (although the σ_{KI} values using the CE γ-ray normaliztion method had larger errors associated with them).

These results can be interpreted in two ways:

a.) The variations between the two methods reflects the degree of accuracy of the some of the more important factors in the $LY_{1,5}$ method such as the $\sigma LY_{1,5}$ values at a particular energy for a given element, the

measured foil thickness which has a strong infuence on the value of $T_{1\gamma}$ or the values of ε_γ at the $LY_{1,5}$ energies of these elements. Using ECPSSR $LY_{1,5}$ cross sections does not seem to make any dramatic changes in the $\sigma LY_{1,5}$ values as shown by the comparison in Table V.2 between the $\sigma LY_{1,5}$ values of W.

b.) The other explanation for the differences can lie in the relative degree of uncertainty in factors pertaining to the RBS method. The particle detector was by neccesity placed very close to the targets due to the "tight" geometrical arrangement of the the chamber. This means that a small absolute difference in the actual distance of the detector from the targets relative to the one used in the normalization calculations could be responsible for a large uncertainty in the particle detector solid angle. This is compounded by the need to collimate the backscatterd beam into the particle detector and add further uncertainty to the value of the solid angle.

These effects concerning particle detector and collimator placement relative to the target holder could become more important at low beam energies where long counting times were needed and particle count rates where much higher than photon rates. Damage to the targets during these long runs results in peeling or flaking of target material could enhance the effects of geometrical uncertainty. On the other hand, the photon methods of normalization tend to minimize any variations in target quality by using just one solid angle, i.e, the one of the photon detector.

The fact that the largest discrepancies between the photon and RBS methods are seen at the lowest beam energies are either due to the decrease in correlation between the particle and photon yields because of target

irregularities induced by high beam currents and longer counting times or due in some measure to the greater uncertainty in the values of $\sigma LY_{1,5}$ at these lower energies. The poorer counting statistics generally encountered at the lower proton energies may also cause problems.

3. Comparison of Experimental Results With Theory and Previous Experimental Results

The results obtained here are in good agreement with the previous results of Anholt for $_{59}Pr$, $_{62}Sm$ and $_{73}Ta$ [21], da Castro Faria for $_{74}W$ [25], Wilson for $_{59}Pr$ and $_{60}Nd$ [26], Goclowski for $_{74}W$ [1], Zelazny for $_{60}Nd$, $_{62}Sm$, $_{69}Tm$ [8] and Divoux for Nd^{142} and Sm^{144} [27].

The results of the different normalization methods are compared with the theoretical values of σ_{KI} from ECPSSR calculations provided by G.Lapicki and SCA calculations of E.C. Montenegro. What can be seen from the comparisons is that at the lowest proton energies both theories tend to overpredict the values of σ_{KI} by factors of between 1.5 - 2 depending on the degree of adiabacity involved in the collision. This is consistent with a compiliation and analysis of the experimental data by Paul and Muhr [28] who break down the experimental results into sets of Z_2 which span decades of atomic numbers.

These collisions where both theories overpredict the σ_{KI} values are in the vicinity of values of ξ_K from 0.18 - 0.275; the largest discrepancies are for the slowest collisions, i.e., smallest values of ξ_K. Our value of σ_{KI} at 1.0 MeV H^+ energy on $_{74}W$ however, is very close to Montenegro's pred-

icted value. In general, Montenegro's SCA approach [29] which takes into account the effects of transient molecular orbital formation and variable charge due to relaxation of the passive electrons and the modification of the active electrons wavefunctions usually gave better agreement at smaller ξ_K.

What we see in terms of the rest of our results (for all three normalization methods, the trends are identical) is that for ξ_K values of between 0.300 - 0.375, the experimental results obtained in this work are in good agreement with the theoretical values of both Montenegro and Lapicki. The analysis of the previous experimental proton data by Paul also indicates that in this range of ξ_K's there is very good agreement between theory and experimental results for the target atomic numbers represented in this work.

At higher values of ξ_K, which in this work take the values of 0.380 - 0.450, it is found by Paul that ECPPSR overpredicts the values of σ_{KI} by amounts varying from 0.10 - 0.20. A look at the σ_{KI} data presented here shows that this trend is repeated with our reported measurements.

The most often given explanations for this behavior of the theories is that at the low projectile velocities the Coulomb deflection term is thought to be inadequate for protons. At the higher velocities, where the values of σ_{KI} predicted are too high, a deficiency in the polarization term is thought to exist.

One reassuring aspect for workers involved in the measurement of σ_{KI} and in calculating ICC's is that the same amount of disagreement is found between theory and experiment for spherical and deformed nuclides after the corrections for IC-CE are made. However, a tidy picture is not com-

pletely justified when the values of σ_{KI} for Ta and W are compared between 1.6 and 2.2 MeV. This degree of "untidiness" may in part be due to our old nemesis, uncertainties in the values of α_K due to uncertainties in the value of δ^2 in the case of the 136 keV transition of Ta^{181}.

We see that in this energy region (and with the two methods of normalization used) the values of σ_{KI} are larger for $_{74}W$ than for $_{73}Ta$. From the point of view of pure atomic collision physics this is an impossibility. However, a main focus of this thesis from its conception has been to unravel any uncertainties (if possible) encountered in measuring σ_{KI} values when both nuclear and atomic inelastic channels need to be considered. In the case of the nuclides Sm^{150} and Sm^{154} any uncertainty was removed by subtracting the appropriate amount of K x-rays arising from IC-CE. This agreement between the experimental σ_{KI} values may be due in large part to the more accurate handling of α_K in the cases involving pure E2 transitions.

The values given for the two elements, $_{73}Ta$ and $_{74}W$ represent the corrected ones using the methods of calculating and subtracting the IC-CE contributions. The proton energies where the discrepancy between the values of σ_{KI} arrived at after making the IC-CE corrections are the ones where for these elements σ_{ce} should be largest relative to σ_{KI}. Therefore, the uncertainties in all of the quantities used in calculating the IC-CE contributions are quite capable of "conspiring" to invert the expected values of σ_{KI} in this range of proton energies, where their relative importance is maximized.

As was pointed out previously W^{183} required a coupled-channels approach in calculating the values of σ_{ce}. However, the appropriateness of this approach (although seemingly quite justified) would not have a major effect

on the amount of IC-CE subtracted from the raw K x-ray yield of $_{74}W$, if for instance the coupled - channels method used here was in error.

More likely, the discrepancy is due to the accuracy of the B(E2)'s used for the three major W isotopes and in both the value of the B(E2) use for the 136 kev level in Ta^{181} and the value of the K-Shell ICC for this level. Recall that this transition is a mixed M1/E2 one so that the values of α_K used (and therefore the amount of subtraction of K x-rays) for this level is very dependent on the best value of δ^2, which we chose from the literature.

We propose the use of W^{183} as a $_{74}W$ target as was suggested earlier in this Chapter. The reason for this is to greatly reduce the IC-CE contributions. W^{183} in addition to having a lower value of σ_{CE} for its 99 keV, $5/2^-$ level (the only one that could be reached via CE with low-energy, light projectiles that could be K-Shell converted) the coupling between the first two excited states lowers the probability for exciting this state relative the similar excited states in the even-A W nuclides which can produce K x-rays from internal conversion. The level structure of W^{183} is given in figure V.9.

4. Summary

We have developed a new method of normalization which can be used to experimentally determine the K-shell ionization cross sections of elements in the rare-earth region. This method appears to give cross section values for protons in the low-energy range which are in good agreement with both previously obtained values and the values of σ_{KI} we measured ourselves using the standard RBS method.

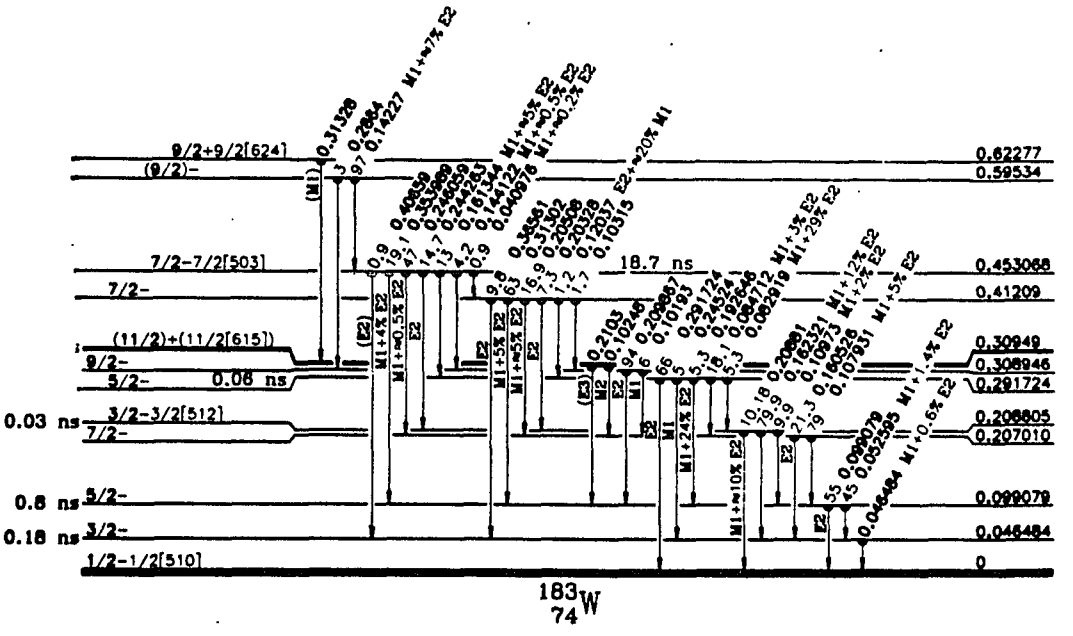

Figure V.9 Level structure of W183 taken from Table of Isotopes, 7th ed.

This method of normalizing to the yield of $LY_{1,5}$ x-rays can be used in tandem with the technique of choosing a particular isotope of elements which lie in the region of strong, permanent nuclear deformations. The selection of the proper isotope can be very effective in reducing the contributions to the total K x-ray yield from IC-CE.

Table V.1
Comparison Between Experimentally Obtained CE Cross Sections for 82 keV level of Sm^{154} and Theoretical Values Calculated Using Bohr-Winther SCA. Experimental uncertainties are± 15 %

Energy (MeV)	Experimental* (mb)	Bohr-Winther SCA (mb)
1.0	2.05	1.74
1.2	2.74	2.80
1.4	4.92	4.45
1.6	6.54	5.66
1.8	8.40	7.46
2.0	9.65	8.65
2.2	10.62	9.67
2.4	11.98	10.84
2.6	12.56	11.92
2.8	14.20	13.20
3.0	16.52	14.30

* CE cross sections obtained using RBS normalization

Table V.2
Experimentally Obtained L Gamma X-ray Cross Sections. Experimental uncertainties are± 6 -7 %

Energy (MeV)	Pr (b)	Nd (b)	Sm (b)	Tm (b)	Ta (b)	W (b)
1.00	0.79	0.70	0.62	0.40	0.20	0.18
1.20	1.15	0.85	0.70	0.58	0.44	0.41
1.40	2.30	1.63	1.25	0.97	0.59	0.54
1.60	3.42	3.09	2.88	1.55	1.18	1.10
1.80	4.72	4.08	3.62	2.29	1.63	1.55
2.00	6.44	5.06	4.43	2.60	2.25	2.16
2.20	7.71	6.51	5.36	3.31	2.73	2.62
2.40	8.13	7.62	6.89	3.97	3.06	2.87
2.60	8.96	8.59	7.40	4.30	3.58	3.08
2.80	10.37	9.57	8.36	5.04	4.18	3.56
3.00	12.78	11.23	10.38	5.90	5.05	4.67

Table V.2a
Comparison Between the L Gamma X-ray Production Cross Sections of W Predicted by ECPSSR and Obtained Experimentally

Energy (MeV)	Experimental (b)	ECPSSR* (b)
1.00	0.18	0.28
1.20	0.41	0.49
1.40	0.55	0.73
1.60	1.10	1.19
1.80	1.55	1.53
2.00	2.16	1.70
2.20	2.62	2.14
2.40	2.87	2.58
2.60	3.08	2.79
2.80	3.56	3.85
3.00	4.67	4.12

*ECPSSR values of Cohen and Harrigan

TableV.3
Data Pertaining to Critical Filters Used in This Work

Target Element	$LY_{1,s}$ Energy[1] (keV)	Absorber Element	Foil Thickness (mg/cm^2)	K_{abs} [1] of absorber (kev)	μ abs[2] (cm^2/g)
Pr	6.32	Ti	12.45	4.97	376.4
Nd	6.60	Ti	12.45	4.97	336.1
Sm	7.17	V	17.04	5.46	294.3
Tm	9.43	Fe	20.52	7.11	198.7
Ta	10.85	Ni	29.45	8.33	166.1
W	11.28	Ni	29.45	8.33	151.4

[1] values taken from J.A.Bearden and A.F.Burr, Rev.Mod.Phys.,39, 125, 1967
[2] values taken from E.C.Montenegro et al., Atomic Data and Nuclear Data 22, NO.2, 1978

Table V.4a

Comparison Between the Experimentally Obtained Values of the K-Shell Cross Sections of Pr using RBS Normalization and the Values Predicted by ECPPSR and Montenegro's SCA

Energy (MeV)	ξ_K	Pr (exp) (mb)	ECPSSR (mb)	SCA (mb)
1.0	0.241	2.59 ± 0.26	5.83	5.6
1.2	0.263	6.00 ± 0.51	12.4	12.5
1.4	0.275	12.2 ± 1.0	22.6	23.2
1.6	0.286	15.9 ± 1.6	37.1	38.5
1.8	0.304	32.7 ± 2.3	56.4	58.9
2.0	0.323	54.9 ± 4.2	81.2	84.8
2.2	0.357	95.0 ± 6	112	117
2.4	0.373	124 ± 10	149	155
2.6	0.388	164.9 ± 12	192	199
2.8	0.402	317.9 ± 18	243	250
3.0	0.417	366.8 ± 20	300	308

Table V.4b
Comparison Between RBS Normalization for Nd142 and Theoretical Values

Energy (MeV)	ξ_K	Nd (exp) (mb)	ECPSSR (mb)	SCA (mb)
1.0	0.236	2.59 ± 0.22	4.80	4.54
1.2	0.258	4.03 ± 0.24	10.3	10.2
1.4	0.278	10.1 ± 0.84	18.8	19.2
1.6	0.298	12.9 ± 0.82	31.0	32.0
1.8	0.316	26.0 ± 1.7	47.3	49.1
2.0	0.334	51.7 ± 4.1	68.2	71.0
2.2	0.350	80.0 ± 5.0	94.1	97.8
2.4	0.365	107.9 ± 7.5	125	130
2.6	0.381	154.3 ± 12	162	168
2.8	0.394	283 ± 17	205	211
3.0	0.410	333.2 ± 22	254	261

Table V.2c Experimental K-Shell Cross Sections of Pr, Nd142 and Sm150 Using L Gamma X-ray Normalization Method

Energy (MeV)	Pr (mb)	Nd^{142} (mb)	Sm^{150} (mb)
1.0	3.81 ± 0.40	2.33 ± 0.25	2.20 ± 0.30
1.2	6.70 ± 0.73	3.24 ± 0.24	2.74 ± 0.27
1.4	11.6 ± 1.7	8.35 ± 0.87	8.01 ± 0.83
1.6	17.3 ± 2.0	13.4 ± 1.2	24.3 ± 1.6
1.8	21.2 ± 1.9	30.0 ± 2.4	39.4 ± 3.4
2.0	54.8 ± 5.5	49.6 ± 4.2	52.9 ± 3.2
2.2	90.9 ± 8.0	70.1 ± 6.5	70.5 ± 6.5
2.4	115.5 ± 11	93.7 ± 10	110.6 ± 8.2
2.6	149.8 ± 14	145.1 ± 16	138.1 ± 13
2.8	291 ± 24	317.2 ± 34	209.7 ± 20
3.0	312.2 ± 29	337.3 ± 33	262.9 ± 19

Table V.2d
Comparison of Experimentally Obtained K-Shell Cross Sections of Sm150 Using RBS Normalization With Predicted Theoretical Values

Energy (MeV)	ξ_K	Sm^{150} (mb)	ECPSSR (mb)	SCA (mb)
1.0	0.228	1.82 ± 0.21	3.05	3.01
1.2	0.248	3.09 ± 0.19	7.15	6.96
1.4	0.268	7.85 ± 0.51	13.2	13.3
1.6	0.288	14.2 ± 0.87	21.8	22.3
1.8	0.305	29.6 ± 1.5	33.5	34.5
2.0	0.321	47.5 ± 2.6	48.5	50.2
2.2	0.336	62.6 ± 4.2	67.1	69.5
2.4	0.352	101.8 ± 5.4	89.7	92.7
2.6	0.365	139.8 ± 7.5	116	120
2.8	0.380	192.9 ± 9.6	147	152
3.0	0.394	223 ± 11	183	187

Table V.2e

K-Shell Cross Sections of Sm(nat.)* and Sm^{154}* using RBS Normalization

Energy (MeV)	ξ_K	Sm(nat.) (mb)	Sm^{154} (mb)
1.0	0.228	1.66 ± 0.21	1.64 ± 0.24
1.2	0.248	2.84 ± 0.20	3.55 ± 0.69
1.4	0.268	8.29 ± 0.51	7.43 ± 0.42
1.6	0.288	16.4 ± 1.0	17.5 ± 0.91
1.8	0.305	26 ± 1.4	33.6 ± 2.0
2.0	0.321	42.9 ± 2.9	42.3 ± 2.2
2.2	0.336	66.6 ± 3.6	68.2 ± 3.6
2.4	0.352	109 ± 5.8	98 ± 4.9
2.6	0.365	147.7 ± 7.6	129 ± 9.5
2.8	0.380	182.2 ± 8.9	192.9 ± 9.3
3.0	0.394	248.7 ± 12	223.4 ± 10

* corrected for IC-CE K x-ray contribution from 122 keV, 2^+ level of Sm^{152} 26.2 % naturally abundant and from 82 keV, 2^+ level of Sm^{154}, 22.6% abundant in the case of natural Sm using Bohr-Winther SCA

Table V.2f

K-Shell Cross Sections Obtained Experimentally Using L Gamma X-ray Normalization For Sm(nat.) and Sm^{154} and Results for Sm^{154} using Coulomb Excitation Gamma-rays For Normalization

Energy (Mev)	Sm(nat) σ_{LY} (mb)	Sm^{154} σ_{LY} (mb)	Sm^{154} (γ-ray) (mb)
1.0	1.83 ± 0167	1.87 ± 0.195	1.54 ± 0.24
1.2	2.97 ± 0.342	2.73 ± 0.240	3.69 ± 0.69
1.4	7.38 ± 0.728	7.99 ± 0.686	9.12 ± 1.4
1.6	22.9 ± 2.19	23.2 ± 1.74	19 ± 2.5
1.8	37.7 ± 3.51	41.5 ± 2.56	30.6 ± 4.3
2.0	55.8 ± 4.67	56 ± 3.33	46 ± 6.4
2.2	85.7 ± 7.64	73.5 ± 6.49	69.5 ± 15
2.4	127.6 ± 10.7	127 ± 10.1	103 ± 19
2.6	153.2 ± 12.4	157.8 ±12.8	139.8 ± 30
2.8	203 ± 17	207 ±16.4	188 ± 9.3
3.0	240.9 ±22	233.2 ± 17.5	221.8 ± 10

Table V.4g

Comparison Between Experimental K-Shell Cross Sections of Tm169* Obtained Using RBS and Predicted Theoretical Values

Energy (MeV)	ξ_K	Tm (exp) (mb)	ECPPSR (mb)	SCA (mb)
1.0	0.199	0.383 ± 0.06	0.937	0.742
1.2	0.213	0.886 ± 0.08	2.18	1.92
1.4	0.230	1.9 ± 0.15	4.18	3.91
1.6	0.244	3.83 ± 0.30	7.09	6.88
1.8	0.261	8.60 ± 10.	11.2	11.0
2.0	0.274	14.7 ± 0.60	16.2	16.3
2.2	0.289	19.1 ± 1.8	22.7	22.9
2.4	0.301	31.0 ± 3.3	30.6	31.0
2.6	0.312	42.7 ± 3.3	40.0	40.6
2.8	0.325	52.9 ± 4.5	50.9	51.7
3.0	0.346	71.1 ± 4.3	63.5	64.4

* Corrected for IC-CE K X-ray contribution using calculated values of σ_{ce} obtained from De-Boer-Winther coupled-channels code

Table V.4h

Comparison Between Experimentally Obtained K-Shell Cross Sections of Tm169 Using L Gamma X-ray Normalization and Predicted Theoretical Values

Energy (MeV)	ξ_K	Tm (exp) (mb)	ECPSSR (mb)	SCA (mb)
1.0	0.199	0.424 ± 0.07	0.937	0.742
1.2	0.213	0.750 ± 0.09	2.18	1.92
1.4	0.230	1.64 ± 0.16	4.18	3.91
1.6	0.244	3.89 ± 0.40	7.09	6.88
1.8	0.261	8.45 ± 1.1	11.2	11.0
2.0	0.274	11.5 ± 0.96	16.2	16.3
2.2	0.289	18.4 ± 1.8	22.7	22.9
2.4	0.301	27.9 ± 2.9	31.0	31.2
2.6	0.312	43.3 ± 4.4	40.0	40.6
2.8	0.325	56.2 ± 6.3	50.9	51.7
3.0	0.346	75 ± 9.4	63.5	64.4

Table V.4i
Experimental K-Shell Cross Sections of Ta181* Obtained Using RBS Normalization Compared With Predicted Theoretical Values

Energy (MeV)	ξ_K	Ta (exp) (mb)	ECPSSR (mb)	SCA (mb)
1.0	0.188	0.263 ± 0.06	0.477	0.338
1.2	0.206	0.452 ± 0.05	1.16	0.947
1.4	0.223	1.17 ± 0.10	2.29	2.03
1.6	0.238	1.84 ± 0.27	3.95	3.68
1.8	0.253	3.16 ± 0.31	6.24	5.99
2.0	0.266	4.75 ± 1.1	9.22	9.03
2.2	0.279	8.22 ± 1.3	13.0	12.9
2.4	0.292	16.7 ± 2.0	17.5	17.5
2.6	0.303	22.8 ± 5.4	23.0	23.1
2.8	0.316	26.5 ± 2.0	29.4	29.5
3.0	0.326	34.4 ± 4.6	36.7	37.0

* Corrected for IC-CE K x-ray contribution using Bohr-WInther SCA

Table V.4j
Comparison Between K-Shell Cross Sections Obtained Using L Gamma X-ray Normalization and Predicted Theoretical Values

Energy (MeV)	ξ_K	Ta(exp) (mb)	ECPSSR (mb)	SCA (mb)
1.0	0.188	0.343 ± 0.08	0.477	0.338
1.2	0.206	0.430 ± 0.07	1.16	0.947
1.4	0.223	1.51 ± 0.25	2.29	2.03
1.6	0.238	2.05 ± 0.40	3.95	3.68
1.8	0.253	3.20 ± 0.5	6.24	5.99
2.0	0.266	4.54 ± 1.1	9.22	9.03
2.2	0.279	8.31 ± 2.0	13.0	21.9
2.4	0.292	22.4 ± 3.9	17.5	17.5
2.6	0.303	31.6 ± 7.7	23.0	23.1
2.8	0.316	37.9 ± 3.5	29.4	29.5
3.0	0.326	46.0 ± 7.4	36.7	37.0

Table V.4k

Comparison Between Experimentally Obtained K-Shell Cross Sections for W(nat.)* obtained Using RBS Normalization and Predicted Theoretical Values

Energy (MeV)	ξ_K	W (exp) (mb)	ECPSSR (mb)	SCA (mb)
1.0	0.182	0.245 ± 0.03	0.404	0.278
1.2	0.200	0.373 ± 0.02	0.995	0.796
1.4	0.217	0.928 ± 0.18	1.98	1.73
1.6	0.232	1.96 ± 0.18	3.43	3.16
1.8	0.244	3.92 ± 0.49	5.34	5.17
2.0	0.257	6.14 ± 0.35	8.50	7.83
2.2	0.270	9.33 ± 0.90	11.3	11.2
2.4	0.283	15.0 ± 1.6	15.4	15.3
2.6	0.293	21.0 ± 1.3	20.1	20.1
2.8	0.306	30.8 ± 2.3	25.8	25.8
3.0	0.317	35.5 ± 4.4	32.2	33.4

* IC-CE contribution for even-A isotopes calculated from first-order SCA, W^{183} σ_{ce} calculated using DeBoer-Winther code

Table V.4l

Experimentally Obtained K-Shell Cross-Sections Using L Gamma X-ray Normalization Compared With Predicted Theoretical Values

Energy (MeV)	ξ_K	W (exp) (mb)	ECPSSR (mb)	SCA (mb)
1.0	0.182	0.210 ± 0.03	0.404	0.278
1.2	0.200	0.517 ± 0.04	0.995	0.796
1.4	0.217	1.19 ± 0.10	1.98	1.73
1.6	0.232	2.95 ± 0.33	3.43	3.17
1.8	0.244	4.14 ± 0.14	5.43	5.35
2.0	0.257	8.54 ± 0.75	8.05	7.83
2.2	0.270	13.1 ± 1.4	11.3	11.2
2.4	0.283	15.7 ± 2.3	15.0	15.4
2.6	0.293	23.3 ± 2.1	21.0	20.1
2.8	0.306	32.1 ± 4.1	25.8	25.8
3.0	0.317	39.0 ± 5.9	35.5	32.2

References for Chapter I

[1]. A.Berinde, C.Deberth, I.Neamu, C.Protop, N.Scintei, V.Zoron, M.Dost and S.Rohl, J. Phys. B **16**, 2875 (1978).

[2]. J.Seidel, S.Rohl, R.Lorek, S.Huchler and M.Dost, Phys. Rev. A **32**, 2142 (1985).

[3]. H.Tawara, Y.Hachiya, K.Ishii and S.Morita, Phys. Rev. A**13**, 572 (1976).

[4]. E.C.Montnegro and A.G.dePinho, J. Phys. B **15**, 1521 (1982).

[5]. D.J.Land, Nucl. Instr. and Meth. B **27**, 491 (1987).

[6]. M.Grysinski and J.A.Kunc, J. Phys. B **19**, 2479 (1986).

[7]. K.M.Barfoot, I.V.Mitchell and H.L.Eschbach, Nucl. Instr. and Meth., **168**, 131 (1980).

[8]. L.Avaldi, I.V.Mitchell and H.L.Eschbach, Nucl. Instr.and Meth. B **3**, 21 (1984).

[9]. T.D.Benyon, Nucl. Instr. and Meth. B **9**, 767 (1985).

[10]. D.Chmielwska, Z.Sujkowski, R.V.F.Janssens and M.J.A.DeVoigt Nuc.Phys **A366,** 142 (1981).

[11]. G.Soff, B.Muller, and W.Greiner, Phys.Rev.Lett. **40,** 540 (1978).

[12]. H.Paul, Nucl. Instr. and Meth. **192,** 11 (1982).

[13]. H.Paul and J.Muhr, Physics Reports **135.** 47 (1986).

[14]. G.Soff, T.DeReus, J.Reinhardt, B.Muller and W.Greiner Nucl.Instr. and Meth. B **9** 747 (1985).

[15]. M.E.Rudd, Proc.Int.Sem.High Energy Ion-Atom Coll., Debrecen, Hungary, Elsevier Sci.Pub. Amsterdam 1982.

[16]. U.Becker, N.Grun, W.Scheid and G.Soff, Phys.Rev.Lett. **56,** 2016 (1986).

[17]. G.Basbas, W.Brandt and B.Ritchie, Phys.Rev. **A7,** (1973) 1971

[18]. J.F.Reading, A.L.Ford and J.S.Smith, **IEEE Trans.Nuc.Sci.**. Vol NS-30 Apr.1983.

[19]. G.Lapicki, E.Carolina Univ., personal communication

[20]. W.E.Meyerhof, Phys.Rev.Lett. **31,** 1341 (1973).

[21]. V.V.Afrosimov, Y.U.S.Gordeev, A.N.Zinoviev, D.H.Rasulov and A.P.Shergin, Proc.Int.Conf. of Elect. and Atom Coll. J.S.Risley, Ed., Univ.Wash.Press, Seattle, 1975.

[22]. W.R.Thorson and J.H.Choi, Phys.Rev.A **15**, 550 (1977).

[23]. G.Lapicki and W.Lichten, Phys.Rev.A **31**, 1354 (1985).

[24]. E.Liarokapis, J.J.M.Zouros and J.S.Greenberg, Phys.Rev. A **36**, 1883 (1987).

[25]. H.P.Trautvetter, J.S.Greenberg and P.Vincent, Phys.Rev.Lett.**37**, 202 (1976).

[26]. M.O.Krause, J.Phys.Chem.Ref.Data **8**, 307 (1979).

[27]. M.R.Zalutsky and E.S.Macias, Phys.Rev.A **11**, 71 (1975).

[28]. B.E.Gnade, R.A.Braga, and R.W.Fink, Phys Rev C **21** 2025 (1980).

[29]. K.Deheimer, J.Ullrich, K.E.Steibing, W.Schadt, S.Kelbch, C.Kelbch R.Schuch, S.Zehendner and H.Scmidt-Bocking, J.Phys.B **19**, 3083 (1986).

[30]. L.Sarkadi, J.Phys. B **19**, 2519 (1986).

[31]. M.H.Chen and B.Crasemann, Phys.Rev A **24**, 177 (1981).

[32]. J.H.Scofield, Phys.Rev.A **10**, 1507 (1974).

[33]. S.I.Salem and P.I.Lee, Phys.Rev.A **10**, 2033 (1974).

[34]. S.T.deZwart, Nucl. Instr. and Meth. B **23**, 239 (1987).

[35]. M.Mack, Nucl. Instr. and Meth. B**23**, 74 (1987).

[36]. N.Stolterfoht, Physics Reports **146**, 315 (1987).

[37]. M.W.Charles and B.A.Cooke, Nucl. Instr. and Meth. **61**, (1968).

[38]. R.L.Kaufman and P.Richard, Meths.of Exp.Physics Vol.13 Spectroscopy, D.Williams, Ed. Acad.Press N.Y.1976.

[39]. R.P.Bhalla, F.D.McDaniel and G.Lapicki, Phys.Rev.A **35**, 3655 (1987).

[40]. Y.Cauchois and G.Restelli, Atomis Inner-Shell Processes, B.Crasemann, Ed., Acad.Press, N.Y. 1975.

[41]. H.D.Hagstrum, Phys.Rev. **96**, 336 (1954).

[42]. R.L.Park, Physics Today **28**, 52 (1975).

[43]. I.Kadar, S.Ricz, V.A.Shchegolev, B.Sulik, D.Varga, J.Vegh,

D.Berenyi and G.Hock, Nucl. Instr. and Meth. B **9**, 451 (1985).

[44]. R.S.Sokhi and D.Crumpton, At.Data and Nucl. Tables **30**, 49 (1984).

[45]. I.Ellis and C.Aston, Proc.Roy.Soc.A **129**, 180 (1930).

[46]. H.R.Hulme, N.F.Mott, F.Oppenheimer and H.M.Taylor, Proc.Roy.Soc. A **155**, 315 (1936).

[47]. M.E.Rose, G.H.Goertzel, B.I.Spinrad, J.Harr and P.Strong, Phys.Rev. **76**, 1883 (1949).

[48]. E.W.S.Burhop, The Auger Effect, Univ.Press Cambridge 1952.

[50]. G.P.Huffman, Nucl. Instr. and Meth. **137**, 267 (1976).

[51]. J.C.Mcgeorge, H.-U.Freund and R.W.Fink, Nucl.Phys. A **154**, 526 (1970).

[52]. R.E.Price, H.Mark and C.D.Swift, Phys.Rev. **176**, 3 (1968).

[53]. M.E.Rose, Nuclear Spectroscopy, Acad.Press, London 1960.

[54]. T.A.Green and M.E.Rose, Phys.Rev. **110**, 105 (1958).

[55]. E.Church and J.Weneser, Phys.Rev. **103**, 1035 (1956).

[56]. P.Hornshoj, B.I.Deutch and A.Miranda, Nucl. Phys. A **95**, 65 (1967).

[57]. C.P.Bhalla, Phys. Rev. **157**, 1137 (1967).

[58]. S.G.Nilsson, Kgl.Dans. Vid.S els. Mat-fys. Medd. **29**, 16 (1955).

[59]. S.G.Nilsson and O.Prior, Kgl. Dan. Vid. Sels. Mat-fys. Medd. **32**, 16 (1961).

[60]. J.P.Davidson, Rev. Mod. Phys. **37**, 105 (1965).

References for Chapter II.

[1]. K.Alder and A.Winther, Ed. Coulomb Excitation, 1966 Acad. Press New York and London.

[2]. K.Way, Ed. Internal Conversion Coefficients, 1973 Acad. Press New York and London.

[3]. H.Paul, Nucl. Instr. and Meth. B**4**, 211 (1984).

[4]. J.S.Briggs, Structure and Collisions of Ions and Atoms, I.A.Sellin, Ed. 1978 Springer-Verlag, Berlin and Heidelburg.

[5]. J.D.Garcia, R.J.Fortner and T.M.Kavanagh, Rev. Mod. Phys. **45**, 111 (1973).

[6]. K.W.Hill and E.Merzbacher, Phys. Rev. A **9**, 156 (1974).

[7]. B.H.Choi, E.Merzbacher and G.S.Khandelwal, At. Data **5**, 291 (1973).

[8]. D.H.Madison and E.Merzbacher, Atomic Inner-Shell Processes, B.Crasemann, Ed., 1975 Acad.Press New York.

[9]. M.H.Chen and B.Crasemann, At. Data and Nucl. Data Tables, **33**, 218 (1985).

[10]. D.D.Cohen and M.Harrigan, At. Data and Nucl. Data Tables **33**, 255 (1985)

[11]. W.Brandt and G.Lapicki, Phys. Rev. A **23**, 1717 (1981).

[12]. G.Basbas, W.Brandt and R.Laubert, Phys. Rev. A **7**, 983 (1973).

[13]. N.Bohr, Kgl. Dans. Vid. Sels. Mat-fys. Medd. **18.No.8** (1948).

[14]. L.Bidenharn and P. Brussard, Coulomb Excitation, 1965 Clarendon Press Oxford.

[15]. L.Bidenharn and R.M.Thaler, Phys. Rev. **104**, 1643 (1956).

[16]. D.Trautmann, F.Rosel and G.Baur, Nucl. Instr. and Meth. **214**, 22 (1983).

[17]. L.Kocbach, J. Phys. B **7**,L487 (1974).

[18]. D.Trautmann, G.Baur and F.Rosel, J. Phys. B **16**, 3005 (1983).

[19]. P.A.Amundsen, L.Kocbach and J.M.Hansteen, J. Phys. B **9**, L203 (1976).

[20]. A.Jakob, D.Trautmann, F.Rosel and G.Baur, Nucl. Instr. and Meth. B **4**, 218 (1984).

[21]. T.Mukoyama and L.Sakardi, Bull.Inst.Chem.Res. Kyoto Univ. **57**, 33 (1979).

[22]. L.Kochbach, Nucl.Instr. and Meth. B **4**, 248 (1984).

[23]. K.Alder, A.Bohr, T.Huus, B.Mottleson and A.Winther, Rev. Mod. Phys. **28**, 324 (1956).

References for Chapter III

[1]. E.C. Feidel and C.J. Umbarger, Nucl. Instr. and Meth. **103**, 341 (1972).

[2]. W. DelBianco, Nucl. Instr. and Meth. **109,** 189 (1973).

[3]. E.Blanke, K.Brand, H.Genz, A.Richter and G. Schrieder, Nucl. Instr. and Meth. **122,** 295 (1974).

[4]. P.R. Hanley, M.R. Cleland, C.F. Mason, K.H. Morganstern and C.C. Thompson, IEEE Trans. Nucl.Sci. **NS-16** 90 (1969).

[5]. C.Cadet, PH.D Thesis CUNY 1987

[6]. I.Feigenbaum, personal communication

[7]. **Vacuum products catalogue,** Kurt J. Lesker Co. 1987

[8]. E.H. Kobisk Proc. Third Conf. Applic. of Small Accel., 1974, Vol.1 pp.31-42.

[9]. X.Guoji, Z. Yuhua, Z. Shengnan and X. Yongchang, Nucl, Instr. and Meth. A **236,** 627 (1985).

[10]. W.K.Chu, J.W.Mayer, M.A.Nicolet, G.Amstel, T.Buck and F.H.Eisen, **Thin Films 17,** 1 (1973).

[11]. P.M.Maier-Komor, Nucl. Instr. and Meth. A **236,** 641 (1985).

[12]. G.Sauerbrey, Z. Physik **155,** 206 (1959).

[13]. J.Sanada, Nucl. Instr. and Meth. **57**, 58 (1967).

[14]. S.Datz and C.Snoek, Phys.Rev. **134**, A347 (1964).

[15]. J.P. Farrell, Brookhaven Technology, Setauket N.Y. personal communication.

[16]. G. Skorinko, Brooklyn College Dept. of Physics, personal communication.

[17]. P.M.S. Lesser, Brooklyn College Dept. of Physics, personal communication.

[18]. D.Sadowski, Anacon Corp. Bartlett, Mass.

[19]. D.Yan, J. Paul Farrell, P.M.S. Lesser, F.H. Pollack, T.F.Kuech and D.J.Wolford, Nucl. Instr. and Meth. B**24/25**, 662 (1987).

[20]. S.E.Bauman, E.T.Williams, H.L.Finston, A.H.Bond and P.M.S.Lesser, Nucl. Instr. Meth. **165**, 57 (1979).

[21]. S.Matteson and M.A.Nicolet, Nucl. Instr. and Meth. **160**, 301 (1979).

References for Chapter IV.

[1]. W.L.Hansen, Nucl. Instr. and Meth. **94**, 377 (1971).

[2]. F.S.Goulding, Nucl. Instr. and Meth. **43**, 1 (1966).

[3]. V.V.Beloshitsky, F.F.Komarov and M.A.Kumakhov, Physics Reports **139**, 293 (1986).

[4]. F.S.Stephens, M.A.Deleplanque, R.M.Diamond, A.O.Macciavelli and J.E.Draper, Phys. Rev. Lett. 55 **2558**, (1985).

[5]. T.B.Johansson, R.Akelsson and S.A.E.Johansson, Nucl. Instr. and Meth. **84**, 141 (1970).

[6]. A.P. Mills and J.Levy, Phys. Rev. D **36**, 1707 (1987).

[6]. M.Geretschlager, Nucl. Instr. and Meth. B **28**, 289 (1987).

[7]. G.I.Johansson, X-Ray Spectr. **11**, 194 (1982).

[8]. T.Aberg, Phys. Rev. A **4**, 1735 (1971).

[9]. R.P.Gardner, A.M.Yacout, J.Zhang and K.Verhese, Nucl. Instr. and

Meth. **A242** 399 (1986).

[10]. F.S.Goulding and J.Jaklevic, Nucl. Instr. and Meth. **142,** 323 (1977).

[11]. R.H.Pehl and R.C.Cordi, Lawrence Berkeley Lab Report, **No.3630,** (1974).

[12]. J.S.Hansen, J.C.McGeorge, D.Nix, W.D.Schmidt-Ott, I.Unus and R.W.Fink, Nucl. Instr. and Meth. **106,** 365 (1973).

[13]. D.D.Cohen, Nucl. Instr. and Meth. **178,** 481 (1980).

[14]. W.J.Gallagher and S.J.Cipolla, Nucl. Instr. and Meth. **122,** 405 (1974).

[15]. E.Liarokapis, J.J.M.Zouros and J.S.Greenberg, Phys. Rev. A **36,** 1883 (1987).

[16]. S.J.Cipolla and S.M.Watson, Nucl. Instr. and Meth. **10/11,** 946 (1985).

[17]. J.Llacer, E.E.Haller and R.C.Cordi, IEEE Trans. Nucl. Sci. **NS-24,** 53 (1977).

[18]. E.C.Montenegro, A.Oliver and F.Aldape, Nucl. Instr. and Meth. B **12,** 435 (1985).

[19]. J.H.Scofield, Phys. Rev. A **9**, 1041 (1974).

[20]. R.L.Becker, A.L.Ford and J.F.Reading, Nucl. Instr. and Meth. B **4**, 271 (1984).

[21]. J.A.Scofield, Phys. Rev. A **10**, 1507 (1974).

[22]. J.L.Campbell, A.Perujo, W.J.Teesdale and B.M.Millman, Phys. Rev. A **33**, 2410 (1986).

[23]. J.L.Campbell, Nucl. Instr. and Meth. B **22**, 13 (1987).

[24]. J.L.Campbell, P.L.McGhee, J.A.Maxwell, R.W.Oliverhead and B.Whittaker, Phys. Rev. A **33**, 986 (1986).

[25]. J.F.Harrison and R.A.Eldred, Adv. in X-ray Anal., **17**, 560 (1974).

[26]. M.P.Fioratti and S.R.Pirematteï, Nucl. Instr. and Meth. **96**, 605 (1971).

[27]. G.Forcianl, Nucl. and Instr. and Meth., **107**, 125 (1973).

[28]. J.L Campbell, B.M.Millman, J.A.Maxwell, A.Perujo and W.J.Teesdale, Nucl.Instr. and Meth. B **9**, 71 (1985).

[29]. D.D.Cohen, Nucl. Instr. and Meth. **178**, 481 (1980).

[30]. W.Maenhaut and H.Raemdonck, Nucl. Instr. and Meth. B **1**, 123 (1984).

[31]. D.D.Cohen and M.Harrigan, At. Data and Nucl. Tables **33**, 256 (1985).

[32]. M.O.Krause, J. Phys. Chem. Ref. Data **8**, 307 (1979).

[33]. J.L.Campbell, B.M.Millman, J.A.Maxwell, R.W.Oliverhead and B.Whittaker,

Nucl. Instr. and Meth. B **9**, 71 (1985).

[34]. D.D.Hoppe, B.M.Coursey and F.J.Schima, Nucl. Instr. and Meth. **193**, 1 (1982).

[35]. W.H.McMaster, Univ. of Cal. Rad. Lab Report **50174**, (1969).

[36]. D.D.Cohen and M.M.Harrigan, At. Data and Nucl. Tables **33**, 256 (1985).

[37]. E.B.Saloman, J.H.Hubbell and J.H.Scofield, At. Data and Nucl. Tables **38**, 1 (1988).

[38]. J.H.Scofield, Univ. of Cal. Rad. Lab Report **51326**, (1973).

[39]. S.J.B.Read and N.G.Ware, J.Phys. E **5**, 582 (1972).

[40]. P.Axel, Brookhaven Natl. Lab No. **271**, (1953).

[41]. V.W.Slivinsky and P.J.Ebert, Nucl. Instr. and Meth. **71**, 346 (1968).

[42]. F.S. Goulding, Nucl. Instr. and Meth. **142**, 213 (1977).

[43]. J.Jaclevic, presonal communication.

[44]. H.J.Fitting, Phys. Status Solidi A **26**, 525 (1974).

[45]. F.P.Larkins, At. Data and Nucl. Tables **20**, 310 (1977).

[46]. D.D.Cohen and M.Harrigan, At. Data and Nucl. Tables **34**, 394 (1985).

[47]. D.D.Cohen, Nucl. Instr. and Meth. B **3**, 47 (1984).

[48]. P.L. McGhee and J.L.Campbell J. Phys B **21**, 2295 (1988).

[49]. C.M.Lederer and V.S.Shirley, Table of the Isotopes, 7th edition, 1978, J.Wiley and sons, New York.

[50]. M.Budner, D.Glavic, A.Kodre and Z.Smit, Nucl. Instr. and Meth. B **31**, 456 (1988).

[51]. H.L.Malm, IEEE Trans. Nucl. Sci. **NS-22**, 140 (1975).

[52]. V.Marrello, T.A.McMath, J.W.Mayer and I.L.Fowler, Nucl. Instr. and Meth.

108, 93 (1973).

[53]. M.Slapa, J.Chwaszczewska, J.Jurkowski, A.Latuszynski, G.C.Huth and A.J.Dabrowski, Adv. X-ray Anal. **14,** 23 (1982).

[54.] R.H.Pehl, R.C.Cordi and F.S.Goulding, Lawrence Berkeley Lab Report **502,** (1971).

[55]. W.L.Hansen and E.E. Haller, Lawrence Berkeley Lab Report **5564,** (1976).

[56]. J.H.Scofield, Univ. of Cal. Rad. Lab Report **51326,** (1973).

[57]. G.Ottavini, C.Canali and G.Majni, J. Appl. Phys. **47,** 627 (1976).

[58]. R.H.Pehl, personal communication.

References For Chapter V

[1]. M.Goclowski, M.Jaskola, J.Szerypo, P.Hornshoj and Z.Zelazny, J. Phys. B

[2]. S.H.Greenberg, E.T.Williams, B.Perley, R.Eldred and D.J.Shadoan, Nucl. Instr. and Meth. B **24/25**, (1987).

[3]. J.H.Scofield, Phys. Rev. A **10**, 1507 (1974).

[4]. D.Trautmann and F.Rosel, Nucl. Instr. and Meth. **169**, 259 (1980).

[5]. F.D.Becchitti and G.W.Greenlees, Phys. Rev. **182**, 1190 (1969).

[6]. P.R.Christensen, I.Chernov, E.E.Gross, R.Stockstad and F.Videbak, Nucl. Phys. A **207**, 433 (1973).

[7]. P.Hornshoj, Z.Zelazny, M.Jaskola, L.Zemlo, A.Celler and J.Szerypo J.Phys. B **14**, 2391 (1981).

[8]. Z.Zelazny, M.Pfuetzner, J.Szerypo and M.Goclowski, J. Phys. B **19**, 4185 (1986).

[9]. K.Alder, A.Bohr, T.Huus, B.Mottleson and A.Winther, Rev. Mod. Phys. **28**, 432 (1956).

[10]. D.D.Cohen, Nucl. Instr. and Meth.B **3**, 47 (1984).

[11]. K.Parthasaradhi, A.Esposito, S.Mobilio and M.Pelliccioni, Phys. Rev. A **38**, 1608 (1988).

[12]. E.C.Montenegro, G.P.Baptista and P.W.E.P. Duarte, At. Data and Nucl. Data Tables **22,** 157 (1978).

[13]. T.Papp and J.Palinakas, Phys. Rev. A (to be published Sept. 1988).

[14]. M.O.Krause, J. Phys. Chem. Ref. Data, **8,** 307 (1979).

[15]. J.H.Schofield, Phys. Rev. A **10,** 1507 (1974).

[16]. S.Raman, C.H.Malarky, W.T.Milner, C.W. Nestor Jr. and P.H.Stelson Atomic Data and Nucl.Tables **36,** No.1 (1987).

[17]. F.Rosel, B.Fries, K.Alder and M.C.Pauli, At. Data and Nucl. Tables **21,** Nos.1,2,4,5 (1978).

[18]. H.R.Verma, A.K.Sharma, N.Singh and P.N.Trehan, J. Phys. Soc. Japan, **45,** 374 (1978).

[19]. F.T.Avignone, J.H.Trueblood and Z.W.Grabowski, Nucl. Phys. A **167,** 129 (1971).

[20]. K.Alder and A.Winther, Ed. Coulomb Excitation, Academic Press, N.Y. 1966

[21]. R.Anholt, Phys Rev. A **17,** 983 (1978).

[22]. K.Alder and A.Winther, Electromagnetic Excitation, 1975 N.Holland Amsterdam-Oxford.

[23]. F.T.Avignone, Rev. Sci. Instr. **39**, 1949 (1968).

[24]. K.Alder and A.Winther, Electromagnetic Excitation, 1975 N.Holland Amsterdam-Oxford.

[25]. N.V. da Castro Faria, F.L.Friere, E.C.Montenegro, A.C. da Pinho and E.F. da Silverira, J. Phys. B **17**, 2307 (1984).

[26]. S.R.Wilson, F.D.McDaniel, J.R.Rowe and J.L.Duggan, Phys. Rev. A **16**, 903 (1976).

[27]. S.Divoux, B.Raith and B.Gonsoir, Nucl. Instr. and Meth. B **3**, 27 (1984).

[28]. H.Paul and J.Mohr, Physics Reports, **135**, 47 (1986).

[29]. E.C.Montenegro and G.M.Sigaud, J. Phys. B **18**, 299 (1985).